

https://dspace.org/

The effect of petrographically determined parameters on carbonaceous reductant reactivity in the production of high-carbon ferromanganese

Soqinase, Sanda

2024
https://hdl.handle.net/10539/37370

Downloaded from a DSpace repository. https://dspace.org/



The effect of petrographically determined parameters on carbonaceous reductant reactivity in the production of high-carbon ferromanganese

A dissertation submitted to
the Faculty of Engineering and the Built Environment
in partial fulfilment of the requirements
for the degree
Master of Science in Engineering

By
Sanda Soqinase

Johannesburg
February 2023

DECLARATION

I, Sanda Soqinase declare that the research reported in this dissertation, except where otherwise stated, is my own original work. This dissertation does not contain other persons' writing or material, unless specifically acknowledged as being sourced from other researchers. This dissertation has not been submitted for any degree or examination at any other university or academic institution.

Signature : 

Surname and initials : Soqinase, S

Student number : 764692

Date : 16 February 2023

Abstract

In pyrometallurgical processes, metal oxides are reduced from slag through carbothermic reduction. The carbonaceous reductant reactivity to slag is of industrial interest as it provides information such as the rate at which MnO dissolves in the slag, which ultimately influences the manganese yield in the alloy.

However, knowledge is limited on the effectiveness of organic composition of the reductants when heated and its contribution that gives rise to the differences of the reductant reactivities of the chosen reductants. This study compares the effect of organic composition of coal on the reductant reactivity to slag. The objectives of the study are

(1) To determine empirically reductant reactivity to slag
(2) To determine petrographically the intrinsic organic properties of the bituminous coal and anthracite as reductants
(3) To compare the fundamental properties and characteristics of bituminous coal and anthracite

The study examined two medium-rank C bituminous coals—labelled coal 1 and coal 2—and anthracite. It investigated the effect of petrographic characteristics on carbonaceous reductant reactivity to slag. The reductant reactivity towards slag tests were conducted in a gas-tight muffle furnace at 1500°C applicable to the chosen three carbonaceous materials.

Analytical techniques, such as SEM-EDS, were applied to measure the extent of MnO reduction (and SiO_2 to a lesser extent) from the slag. It was expected for MnO and SiO_2 from slag to be partially reduced to form Mn and Si in the alloy phase. Other analytical techniques were applied, such as proximate analyses, which indicated the differences and similarities between the chosen carbonaceous reductants as the fundamental basis for evaluating coal for technological use.

The maceral data revealed coal 2 consisted of a greater proportion of reactive macerals than coal 1 and anthracite. The anthracite sample, consisting of the highest inert maceral proportions, had the least mass loss.

Acknowledgments

To my principal supervisor, Paul den Hoed, thank you for your guidance and contribution to this work—for never failing to tend to the ingenious spark to teach and share knowledge.

To my co-supervisor, Dr Joalet D. Steenkamp, thank you for birthing this vision that made this research possible. Thank you for believing in me and your continued wisdom.

To my reason for being, my family, thank you for your love, continuous support and patience with me.

Sanda Soqinase

Table of Contents

1 INTRODUCTION 12

1.1 Background 12

1.2 Research problem 15

1.3 Research aim 15

2 LITERATURE REVIEW 16

2.1 Reduction mechanisms 16

2.1.1 Pre-reduction zone 16

2.1.2 Coke-bed zone 17

2.2 Carbonaceous reductants in HCFeMn production 20

2.3 Coal characterization 21

2.3.1 Proximate analysis 22

2.3.2 Petrographic analysis 22

2.3.3 Reactivity analysis 29

2.4 Effect of petrographic constituents on reactivity 31

2.5 Research questions 33

2.6 Research objectives 33

3 TEST PROCEDURE 34

3.1 Source and prepare raw materials 34

3.2 Characterize raw materials 38

3.2.1 Bulk chemical composition 38

3.2.2 Bulk phase chemical composition 40

3.2.3 Specific phase-chemical composition 40

3.2.4 Petrographic analysis 40

3.3 Reactivity test 41

3.4 Characterization of post-mortem samples 45

4 RESULTS 46
4.1 Material characterization 46
4.1.1 Chemical analysis 46
4.1.2 Bulk phase chemical analysis 53
4.1.3 Specific phase-chemical analysis 54
4.1.4 Petrographic analysis 57
4.2 Reactivity test results 70
4.3 Characterization of post mortem samples 73
4.3.1 Macroscopic observations 73
4.3.2 Specific phase chemistry analysis 79
4.3.3 Petrographic observations 98
5 DISCUSSION 103
5.1 Effect of coal rank 103
5.2 Effect of maceral analysis 105
6 CONCLUSIONS AND RECOMMENDATIONS 108
7 REFERENCES 110
APPENDIX A 116
Reactivity test data 116
APPENDIX B 119
Method development 119
Standard operating procedures used for the muffle furnace type tests 124
APPENDIX C 129
Petrography data 129
SEM-EDS data 140

LIST OF TABLES

Table 1: Typical chemical compositions of manganese alloys (% — ASTM Standard A99) 12

Table 2: Summary of most common coal quality parameters and their implications (Pinheiro, 2006) 21

Table 3: Proximate analyses of the reductant samples 46

Table 4: Ash oxide analyses of major and minor elements as determined by XRF for coal 1 49

Table 5: Ash oxide analyses of major and minor elements as determined by XRF for coal 2 50

Table 6: Ash oxide analyses of major and minor elements as determined by XRF for anthracite 51

Table 7: Chemical composition of HCFeMn slag (XRF) 52

Table 8: Chemical composition of HCFeMn slag (ICP) 53

Table 9: Summary table of the mineral abundance found in the HCFeMn slag sample 54

Table 10: Normalised HCFeMn slag elemental composition of Area A, point 1 and 2 by SEM-EDS (mass%) 56

Table 11: Elemental composition of the MnS phase found in as-received slag (mass%) 57

Table 12: Elemental composition of the alloy entrained in the as-received slag (mass%) 57

Table 13: Reflectance measurements summary table for Coal 1, Coal 2 and Anthracite 58

Table 14: Summary table of maceral group analyses (Incl. mm- including mineral matter, mmf-mineral matter free basis) 60

Table 15: Summary table of the dominant macerals in Coal 1, Coal 2 and Anthracite (inc. mm- including mineral matter, mmf-mineral matter free basis) 62

Table 16: Microlithotype analyses for Coal 1, Coal 2 and Anthracite 69

Table 17: Mass loss % Coal 1, Coal 2 and Anthracite at the different reaction time ...71

Table 18: Summary of the observations of the photographic images of heat-treated samples.....76

Table 19: Elemental composition of the alloy phases at 72 minutes reaction time Coal 1 (mass%).....82

Table 20: Elemental composition of alloy phase and SiC at 72 minutes reaction time for Coal 2 (mass%).....82

Table 21: Elemental composition of the alloy phase at 72 minutes reaction time Anthracite (mass%) 82

Table 22: Elemental chemical composition of the alloy phase at 144 minutes reaction time Coal 2 (mass%) 84

Table 23: Elemental composition of the identified alloy phases at 144 minutes reaction time Anthracite (mass%). 84

Table 24: Elemental composition of the spinel phase found associated with slag (mass%) 85

Table 25: Elemental composition of the alloy at 216 minutes reaction time Coal 1 (mass%) 87

Table 26: Elemental composition of the FeMn alloy and SiC at 216 reaction time Coal 2 (mass%).....87

Table 27: Composition of two phases in alloy at 216 minutes reaction time Anthracite(mass%) 88

Table 28: Alloy composition at 288 minutes reaction time Coal 1 (mass%).....90

Table 29: Elemental composition of the alloy phase at 288 minutes reaction time Coal 2 (mass %).....90

Table 30: Alloy composition at 288 minutes reaction time Anthracite (mass%) 90

Table 31: Elemental compositions of the Si-Mn alloy and SiC at 360 minutes reaction time Coal 2 (mass%) 93

Table 32: Alloy composition at 360 minutes reaction time Anthracite (mass%) 93

Table 33: Oxide composition of the slag at different reaction times for the different carbonaceous reductants.....95

Table 34: Summary table of MnO in slag at the different reduction times (mass%)...96

Table 35: Summary table, elemental composition of Mn in metal as a function of reaction time (mass%) 97

Table 36: Temperature profile for reactivity tests in muffle furnace 116

Table 37: Coal 1 reactivity tests data 117

Table 38: Coal 2 reactivity tests data 117

Table 39: Anthracite reactivity data test 1 118

Table 40: Anthracite reactivity tests 2 data 118

Table 41: Anthracite reactivity tests 2 data 118

Table 42: Maceral group analysis of the three studied parent coals 132

Table 43: Vitrinite reflectance analysis data of the parent coals 133

List of Figures

Figure 1: Conceptual diagram of the different reaction zones in SAF (illustrated by Ringdalen et al., 2015) 13

Figure 2: Reduction paths for different basicities, b (from Olso et al., 1998).....20

Figure 3: Coalification process from peat through to bituminous coals with increasing temperature and pressure (Myrvagnes, 2008) 23

Figure 4: Changes in chemical structure from high volatile bituminous coal to anthracite (Teichmüller and Teichmüller 1968) 24

Figure 5: Maceral groups with their formation origins and typical morphology (Falcon and Ham, 1988) 28

Figure 6: Reactive and non-reactive macerals (Falcon and Snyman, 1986) 32

Figure 7: As-received carbonaceous reductants (a) coal 1 (b) coal 2 and (c) anthracite 34

Figure 8: Coal sample preparation flow sheet 35

Figure 9: Photographs of the prepared reductant crucible from the large lumps for the reactivity tests. (a) Drilled reductant to prepare 'crucible', (b) The reductant 'crucible' filled with HCFeMn slag, (c) Alumina crucible used for containing 'crucible' and slag, (d) Refractory board placed on top of the alumina crucible with 'crucible' and slag inside.....37

Figure 10: HCFeMn slag sample (a) as-received HCFeMn slag before crushing (b) crushed HCFeMn slag.....37

Figure 11: HCFeMn slag sample preparation flowsheet.....38

Figure 12: Experimental set-up used for the carbonaceous reductant reactivity on slag tests (a) Gas tight chamber furnace (b) Sample set-up inside chamber 42

Figure 13 : Schematic layout of the experimental set-up 42

Figure 14: Method for chamber furnace reactivity tests.....43

Figure 15: Determined mineral matter distribution across Coal 1, Coal 2 and Anthracite.....52

Figure 16: XRD diffractograms of the as-received slag sample showing phase counts. (a) Generated from EVA software (b) Generated from Topaz software.....54

Figure 17: SEM micrographs of the as-received HCFeMn slag sample conducted at 20.0 kV. (a) Secondary electron image. Scale bar indicates 200 μm. (b) Backscattered-electron image of zoomed out area A indicating primary phase as '1' and secondary phase as '2'. Scale bar indicates 10 μm.....55

Figure 18: SEM backscattered electron image conducted at 15.0kV. (a) MnS spheres. Scale bar indicates 5 μm (b) MnS sphere zoomed out associated with the secondary slag phase. Scale bar indicates 2 μm. 56

Figure 19: SEM backscattered electron image conducted at 15.0kV. (a) metal prill entrained in the feed slag consisting of Fe metal. Scale bar indicates 10 μm (b) Zoomed out area of metal prill. Scale bar indicates 1 μm.....57

Figure 20: Reflectance histograms for a) Coal 1, b) Anthracite, bi-modal distribution and, c) Coal 2, single bell curve.....59

Figure 21: Inertinite proportion without mineral matter (mmf) and including mineral matter vs rank relationship.....64

Figure 22: Vitrinite group without mineral matter (mmf) and including mineral matter (incl. mm) vs rank.....65

Figure 23: Plates A-D for parent Coal 1.....65

Figure 24: Plates A-D for parent Coal 2.....66

Figure 25: Plates A-D for Anthracite parent coal.....67

Figure 26: Mass loss % table with corresponding curves for Coal 1, Coal 2 and Anthracite at the different reaction time 71

Figure 27: Mass loss profiles for Coal 1, Coal 2 and Anthracite highlighting slag and crucible mass.....72

Figure 28: Images of the heat -treated samples at the different reaction times at 1500°C.....75

Figure 29:Cross-section images of the heat-treated samples for the different reductants at different reaction times.....79

Figure 30: SEM backscattered electron image of Coal 1 at 72 minutes reaction time conducted at 20.0 kV (a) Slag, Coal 1 and alloy phases. Scale bar indicates 100 μm. b) Identified slag phases with associated features. Scale bar indicates 20 μm. 81

Figure 31: SEM backscattered electron image at 72 minutes reaction time conducted at 20.0 kV (a) Slag, Coal 2 and alloy interface. Scale bar indicates 100 μm. (b) Alloy phase associated with SiC. Scale bar indicates 200 μm. 81

Figure 32: SEM backscattered electron image of anthracite-slag at 72 minutes reaction time conducted at 20.0 kV. (a) Interface of the anthracite and slag with alloy phase. Scale bar indicates 100 μm. (b)Identified slag phases in Area A. Scale bar indicates 10 μm. 82

Figure 33: SEM backscattered electron image of the alloy of area A conducted at 20.0 kV. (a) The three phases of alloy, slag and coal existing with the associated SiC phase. Scale bar indicates 40 μm. (b) The two slag phases identified in Area A. Scale bar indicates 20 μm. 83

Figure 34: SEM backscattered electron image of Anthracite, slag and alloy conducted at 20.0kV. (a) Interface of slag and Anthracite with the formed alloy and Area A at lower magnification. Scale bar indicates 100 μm. (b) Identified slag and alloy phases from Area A. Scale bar indicates 10 μm. 84

Figure 35: SEM backscattered electron image at 216 minutes reaction time conducted at 20.0kV. (a) Interface between coal and slag with alloy and area B at low magnification. Scale bar indicates 100 μm. (b) The identified slag phases (1) Primary slag phase (2) Secondary slag phase (3) Associated Magnesium alumina spinel phase ($MgAl_2O_4$). Scale bar indicates 10 μm. 86

Figure 36: SEM backscattered electron micrograph at 216 minutes reaction time conducted at 20.0 kV. (a) interface of alloy with associated SiC, Coal 2 and slag. Scale bar indicates 200 μm. (b) Area A identifying the different slag phases. Scale bar indicates 100 μm. 86

Figure 37: SEM backscattered electron micrograph at 216 minutes reaction time conducted at 20.0 kV. (a) interface of slag- Anthracite with alloy phase. Scale bar indicates 200 μm. (b) Identified slag phases at 216 minutes reaction time. Scale bar indicates 20 μm. 87

Figure 38: SEM backscattered electron image at 228 minutes reaction time for Coal 1 conducted at 20.0 kV. (a) Coal 1, slag and alloy with metal prills in the slag. Scale bar indicates 50 μm. (b) Slag phases identified. Scale bar indicates 100 μm. 89

Figure 39: SEM backscattered electron image at 288 minutes reaction time for Coal 2 conducted at 20.0 kV. (a)Coal and alloy interface boundary with identified area B. Scale bar indicates 100 μm(b) Area B with the different slag phases observed, (1) secondary dark spheres phase, (2) primary slag matrix phase (3) SiC, (4) slag vein rich in Ca. Scale bar indicates 30 μm. 89

Figure 40: SEM backscattered electron image at 288 minutes reaction time conducted at 20.0 kV. (a) Interface between the slag and anthracite and alloy with SiC. Scale bar indicates 50 μm. (b) Area A with TiC found in the alloy and the Si-Mn alloy phases as indicated by point 2 and 3. Scale bar indicates 10 μm. 90

Figure 41: SEM backscattered electron image of the slag- coal interface with alloy at 360 minutes reaction time conducted at 20.0 kV. (a) Slag and coal interface with alloy with focus on area A at low magnification. Scale bar indicates 100 μm. (b) Area A showing associated SiC with the alloy. Scale bar indicates 50 μm. 92

Figure 42: Backscattered electron image at 360 minutes reaction time Coal 2 conducted at 20.0 kV. (a) slag and alloy phases with TiC. Scale bar indicates 100 μm (b) Zoomed Area A with the identified phases associated with slag. Scale bar indicates 30 μm. 92

Figure 43: SEM backscattered electron image of the present slag phases at reaction time 360 minutes Anthracite conducted at 20.0kV. (a) Slag anthracite interface. Scale bar indicates 200 μm. (b) Zoomed out Area A of the slag with identified slag phases. Scale bar for area A indicates 20 μm. 93

Figure 44: Plate A and B showing the evolution of the vitrinite and inertinite when heated at 72 minutes reaction time 100

Figure 45: Plates A- D for Coal 2 showing the progression as a function of reaction time. 101

Figure 46: Plates A-B for Anthracite showing evolution of macerals at 216 minutes reaction time....102

Figure 47: Variation of key coal properties with coal rank (Ward, 2008(ed.)) 103

Figure 48: Coal rank relationship with volatile matter and fixed carbon for Coal 1, Coal 2 and Anthracite....104

Figure 49:Graph representing temperature profile of actual vs set-point 117

Figure 50: Coal 1 histogram with V-steps 129

Figure 51: Coal 2 V-steps and histogram distribution....130

Figure 52: Anthracite histogram distribution and V-steps 131

Figure 53: Zoomed out alloy phases of Coal 1 at 72 minutes reaction time 140

Figure 54: Alloy phases for Coal 1 at 72 minutes reaction time with a different microstructure....141

Figure 55: Coal 1 at 216 minutes reaction time, showing porous coal with slag depositing within the pores....141

Figure 56: Settling phases found at the bottom of alumina crucible in Coal 1 at 288 minutes reaction time.....142

Figure 57: Coal 1 at 360 minutes reaction time showing alloy found in between large pores with slag.....142

Figure 58:Coal 2 alloy at 144 minutes reaction time associated with the slag.....143

Figure 59: Zoomed out phases associated with alloy at 288 minutes reaction time Coal 2.....143

Figure 60: Alloy of Anthracite at 72 minutes reaction time with displaced slag.....144

Figure 61: Metal prills found finely disseminated in Anthracite at 144 minutes reaction time.....144

Figure 62: Alloy phases of Anthracite at 144 minutes reaction time.....145

1 INTRODUCTION

1.1 Background

Manganese alloys are produced through the carbothermic reduction of the manganese ore. The most important manganese alloys are high-carbon ferromanganese (HCFeMn) or standard ferromanganese, refined-grade ferromanganese (MCFeMn), low-carbon ferromanganese (LCFeMn), and silicomanganese (SiMn). These grades vary in manganese, carbon, sulfur, and phosphorous contents. The compositions defining class are set out in Table 1.

Table 1: Typical chemical compositions of manganese alloys (% – ASTM Standard A99)

	HCFeMn			MCFeMn				LCFeMn	
Grade	**A**	**B**	**C**	**A**	**B**	**C**	**D**	**A**	**B**
Mn	78.0-82.0	76.0-78.0	74.0-76.0	80.0-85.0	80.0-85.0	80.0-85.0	80.0-85.0	85.0-90.0	80.0-85.0
C	7.5	7.5	7.5	1.5	1.5	1.5	1.5	–	0.75
Si	1.2	1.2	1.2	1.5	1.0	0.70	0.35	2.0	5.0–7.0
P	0.35	0.35	0.35	0.30	0.30	0.30	0.30	0.20	0.30
S	0.050	0.050	0.050	0.020	0.020	0.020	0.020	0.020	0.020

High carbon ferromanganese (HCFeMn) is commonly produced in submerged arc furnaces (SAF), in which metal oxides are reduced by carbon from coke or coal char to form a slag phase (Ostrovski and Swinbourne, 2013). Excavation of an industrial ferromanganese electric furnace revealed different reaction zones within the furnace interior, as illustrated in Figure 1 (Tangstad and Olsen, 2004; Ringdalen *et al.,* 2015). Studies have divided furnaces into two main reaction zones: the pre-reduction zone, where solid charge is found, and coke bed zone, where ore, slag and fluxes are found molten (Tangstad and Olsen, 2015).

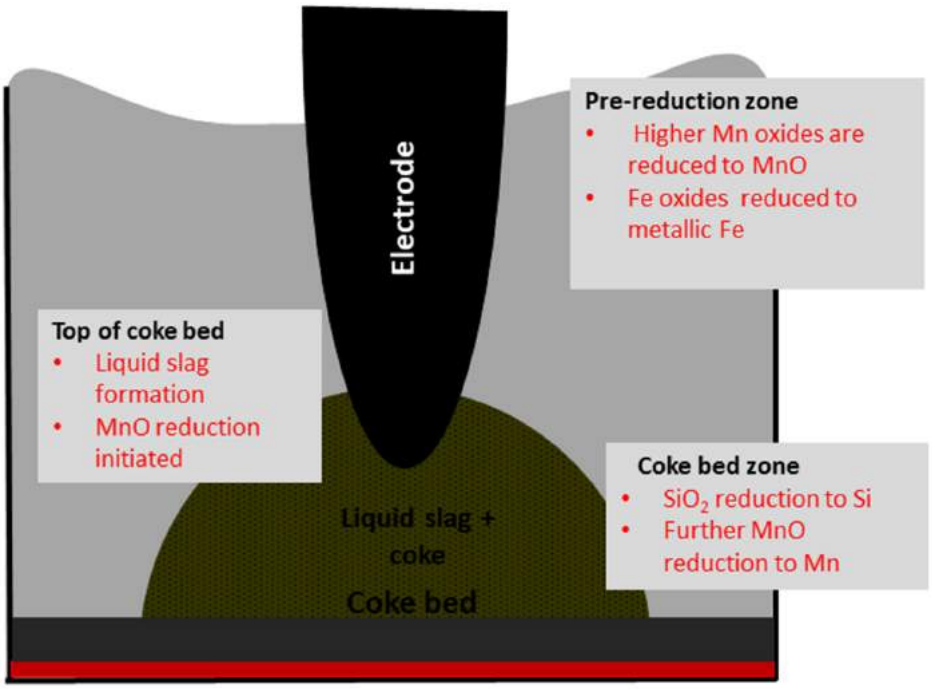

Figure 1: Conceptual diagram of the different reaction zones in SAF (illustrated by Ringdalen *et al.*, 2015)

The reduction of the higher oxides of manganese to MnO by CO gas in the pre-reduction zone occurs through solid-gas reactions. In the coke-bed zone, where liquid-solid reactions occur, the manganese is produced through the interaction of an MnO-containing slag with carbon to form metallic Mn (Lindstad *et al.*, 2007). The main role of the carbonaceous material is reduction of oxide compounds either by the Boudouard reaction or direct reduction (Suharno *et al.*, 2018).

The carbonaceous reductant can be involved in the following reaction paths:

- Gas reduction (pre-reduction) of higher manganese oxides and iron oxides by ascending CO gas. The CO gas forms either when solid reductant reacts with liquid slag components, lower down in the furnace, or when CO_2, formed by reduction of higher Mn oxides and iron oxides, reacts with solid reductant in the Boudouard reaction.
- Dissolution of MnO and SiO_2 in the slag and subsequent reaction with solid reductant to form Mn and Si dissolved in the metal phase, the product of molten iron formed during solid-state reduction.

- Dissolution of solid carbon in the alloy as the alloy becomes saturated in carbon.

The main reaction observed in the coke-bed zone is the reduction of MnO from liquid slag, by either solid carbon or solute carbon, to form metallic manganese (Mn) (Kim, 2018; Lindstad *et al.,* 2007). Molten slag first forms at the top of the coke-bed zone, where most oxides are reduced from the slag. This reaction relates to the reductant reactivity to slag, which forms an integral part of this study.

The reactivity of reductant to slag is defined as the potential of the carbonaceous reductant to react with main slag components, specifically MnO in the coke-bed zone, where direct reduction of MnO to metallic Mn occurs. Reactivity refers loosely to the rate at which a chemical substance undergoes a reaction. Reactivity can also refer to a property or behaviour such as the ability of carbon to react with MnO in a chemical or metallurgical process (Myrvagnes and Lindstad, 2007).

Organic matter in coal forms as a result of biochemical and physicochemical changes in plant matter (Diessel, 1992). The organic constituents, known as macerals, in turn form the fundamental basis for petrographic assessment. There are three main maceral groups that form the basis of coal petrography. They are based primarily on reflectance and physical properties. The macerals are vitrinite, liptinite, and inertinite. Each maceral is distinguished by a unique set of physical, chemical, and technological properties for a given rank (Chen and Ma, 2002); the set ultimately contributes to the behaviour of coal. Generally, the maceral groups are divided into reactive and unreactive groups on the basis of change in structure and shape when heated (Falcon *et al.,* 2018). Reactive macerals soften and release volatile matter, resulting in char formation (Falcon *et al.,* 2018). Inert forms of inertinite macerals of any rank do not combust easily and require more heat (Falcon and Ham, 1988).

The physico-chemical behaviour and thermo-chemical transformation of coal for industrial use is notably dependent on the petrographic make-up of coal (Choundary *et al.,* 2008). The maceral content of a particular coal is found to greatly influence the coal properties, which in turn affects the thermal behaviour of the coal. The ability of the organic component of coal to transform in its chemical reactivity and structure

when heated should be a consideration when choosing a carbonaceous reductant. The coking coal or coal char will reflect the characteristics of the original coal.

The organic composition of the reductant and the transition it undergoes when subjected to heating affects the effectiveness of a reductant and controls its chemical properties (Pinheiro,2006). A first step, therefore, in understanding the influence of petrography on the performance of coals during high-carbon ferromanganese production will be determining the petrographic constituents of these coals.

1.2 Research problem

The ferromanganese industry is a significant consumer of carbonaceous reductants. New types of reductant are always a possibility. If they are to be considered for use, then characterizing them—determining their petrographic and other properties and relating these properties to expected behaviour—will secure a measure of confidence. And the petrographic properties are critical for, despite similar chemical specifications, different reductants perform differently in different applications because of their different petrographic properties.

This study establishes the key characteristics or properties of carbonaceous reductants that determine the reactivities of these reductants to slag in the production of HCFeMn. Some characteristics, such as proximate analysis, will tell us something about how a coal will behave in a given application. In the production of HCFeMn, however, there is much we do not know about the reactivities of reductants towards slags, and what properties affect reactivity.

1.3 Research aim

To explore the thesis that reactive macerals identified and quantified petrographically affect the reactivity of a reductant towards a slag in HCFeMn production.

2 LITERATURE REVIEW

2.1 Reduction mechanisms

The interior of a SAF in HCFeMn production comprises two zones, pre-reduction zone and a coke bed (see section 1.1).

2.1.1 Pre-reduction zone

This is the low-temperature, upper part of the furnace, where solid charge sits and solid-state reduction of manganese oxide occurs. The charge is reduced by CO formed in the lower part of the furnace (Kim, 2018; Tangstad *et al.*, 1998). The reactions that occur in the pre-reduction zone are mainly between gas and solid. The unstable higher oxides of manganese (Mn_2O_3 to Mn_3O_4) and most iron oxides are reduced easily in the solid state by CO (Tangstad and Olsen, 1995). The reactions in the pre-reduction zone are those described in equations 1−4. They are exothermic and heat the charge in the furnace (Tangstad *et al.*, 2015). On the other hand, reaction 5, the Boudouard reaction, takes effect when temperatures reach 800°C. As it is endothermic (drawing energy in) it is undesirable.

$$MnO_{2\,(s)} + \frac{1}{2}CO_{(g)} = \frac{1}{2}Mn_2O_{3(s)} + \frac{1}{2}CO_{2(g)} \quad [1]$$

$$\frac{1}{2}Mn_2O_{3(s)} + \frac{1}{6}CO_{(g)} = \frac{1}{3}Mn_3O_{4(s)} + \frac{1}{6}CO_{2(g)} \quad [2]$$

$$\frac{1}{2}Fe_2O_{3(s)} + \frac{3}{2}CO_{(g)} = Fe_{(s)} + \frac{3}{2}CO_{2(g)} \quad [3]$$

$$\frac{1}{3}Mn_3O_{4(s)} + \frac{1}{3}CO_{(g)} = MnO_{(s)} + \frac{1}{3}CO_{2(g)} \quad [4]$$

$$C_{(s)} + CO_{2(g)} = 2CO_{(g)} \quad [5]$$

$$\frac{1}{3}Mn_3O_{4(s)} + \frac{1}{3}C_{(s)} = MnO + \frac{1}{3}CO_{(g)} \quad [6]$$

Power consumption is mainly determined by reactions in the pre-reduction zone (Tangstad *et al.*, 1998). Reduction of Mn_3O_4 to MnO may take place in two ways. It may be reduced by CO in an exothermic reaction (reaction 4), or it may occur concurrently with the endothermic Boudouard reaction, resulting in net reaction 6 (Kim, 2018; Tangstad and Ishak, 2007). At temperatures up to 1000°C the rate of reaction is dependent on temperature and controlled by the Boudouard reaction (Eric and

Akdogan, 1995). According to Kim (2018), the gaseous diffusion of CO and CO_2 between particles of oxide and carbon determines the rate of reaction.

2.1.2 Coke-bed zone

The coke bed is a high-temperature zone that comprises liquid slag and solid carbon in contact with each other (Kim, 2018; Safarian *et al.*, 2009) and a mixture of metal droplets and gas (Olso *et al.*, 1998; Eidem *et al.*, 2010). According to Ringdalen *et al.* (2009) almost all of MnO reduction occurs at the top of the coke-bed zone. An initial MnO-SiO_2-Al_2O_3-CaO-MgO slag is produced concomitantly at the top of the coke bed where manganese oxide is firstly dissolved into the slag then reduced from the slag (Kononov, 2007). In this zone, a stoichiometric surplus of carbon is found. As the charge reaches this zone, the ore melts and reduction occurs (Tangstad and Olsen, 1997). The remainder of slag and metal drain continuously into the coke bed with the solid coke depositing on top of the coke-bed zone (Kim, 2018). The draining of liquid slag requires that the viscosity of the slag, as controlled by temperature, be low (Ringdalen *et al.*, 2015).

Reaction 7 is the main reaction observed in the coke-bed zone for the production of HCFeMn; it ultimately controls the distribution of manganese between slag and alloy (Ringdalen and Tangstad, 2009). Both equations 7 and 8 are considered in the production of SiMn and control the distribution of silicon and manganese between slag and alloy.[1] The optimum in furnace operation is defined by low power consumption and stable load. How the reactions in the coke-bed zone play out determines the stability of the operation (Tangstad *et al.*, 1998).

$$(\mathrm{MnO})_{(l)} + \mathrm{C} = \langle \mathrm{Mn} \rangle_{(l)} + \mathrm{CO}_{(g)} \quad [7]$$

$$(\mathrm{SiO_2})_{(l)} + 2\mathrm{C} = \langle \mathrm{Si} \rangle_{(l)} + 2\mathrm{CO}_{(g)} \quad [8]$$

MnO reduction by CO gas is impossible—the low equilibrium constant is too low (Safarian *et al.*, 2006). However, MnO can only be reduced carbothermically where the carbon source is either solid or dissolved carbon, the latter dissolved in the metal

[1] Round brackets in equations 7 and 8 denote species in the slag phase; angular brackets, species in the metal phase.

phase. SiO_2 can only be reduced by solute carbon or solid carbon in the presence of either metallic Fe or Mn because the formation of Si metal requires a low Si activity (Gaal et al., 2004) .

The significance of a carbonaceous reductant is its reducing role in the pre-reduction zone and coke-bed zone—i.e., through direct carbothermic reduction in the coke-bed zone and through the release of up-flowing CO gas in the pre-reduction zone. The coke-bed zone is defined as the place where most metal forms in the reduction of MnO. That formation relates to the reactivity of the reductant towards slag. Almost all of the MnO is reduced at the top of the coke bed, where the process heat is generated (Safarian *et al.,* 2009). Thus, a study of the reduction in this zone will provide useful insights into mechanisms by which MnO is reduced from slag.

Several studies have been conducted to understand the mechanisms by which carbon reduces MnO from high-carbon ferromanganese slags (Rankin *et al.,* 1980; Coetsee, 2018; Safarian *et al*., 2008, 2009). According to Lindstad *et al*. (2007) the reduction of MnO to metallic Mn from molten slag involves three main steps, namely—

- The dissolution of the MnO phase into the liquid slag
- Diffusion of MnO in liquid slag to the solid carbon
- Reduction of dissolved MnO at the interface between slag and carbon

Several parameters have a bearing on the rate of carbothermic reduction of MnO from liquid slags. Studying these parameters is all about gaining a better understanding of their effects on reductant reactivity towards slag. The parameters studied, which work through reaction kinetics and thermodynamics, include temperature, slag composition, slag basicity, and the activity of MnO in slag.

Temperature was one of the parameters found to play a role in the reduction rate of MnO (Olso *et al*., 1998). A study of MnO reduction by graphite (Rankin and Deventer, 1980) determined that the rate of reduction of MnO increased with increasing temperature. A typical solidified slag sample consists of two areas, one area with spherical MnO particles and a crystalline area with MnO dendrites (Tangstad and Olsen, 1997; Olso *et al.,* 1998). Olso *et al.* (1998) found that the reduction rate in a two-phase area is constant until all the solid MnO is dissolved. The reduction of MnO then

proceeds in the liquid phase (Lindstad *et al.,* 2007; Ringdalen *et al.,* 2009). It has also been observed that the rate of MnO reduction from silicate slags is affected by the type of carbonaceous reductant used (Safarian and Kolbeinsen, 2008; Tranell *et al.,* 2007).

The carbothermic reduction of MnO is found to be mix-controlled, and involves both a chemical reaction and CO-gas mass transfer in the gas phase (Safarian and Kolbeinsen, 2008). Safarian *et al.* (2009) suggested that reaction rates are not controlled by diffusion of components in the bulk of the slag and metal phases, but by chemical reactions. The reduction mechanism is also believed to take place in stages. MnO reduction takes place in a fast initial stage and a slower second stage, where the decreasing rate is due to the decreasing activity of MnO. According to Kolbeinsen *et al.* (2006), the first rapid stage is determined by a liquid slag coexisting with solid MnO. The slag is saturated in MnO, the activity of which is close to 1. Consequently, the reduction rate is found to be relatively high. This shows that the reduction rate may also be controlled by MnO activity of the slag. Later, as solid MnO phase is consumed, the activity of MnO decreases, which leads to a slowing down of the reduction rate.

The effect of basicity was explored and three basicities were chosen for the study by Olso *et al.* (1998). The reduction rate was found to change with basicity: the rate of reduction decreases with increasing basicity. Olso *et al*. (1998) found that in the first stage of reduction the rate decreases with increasing basicity, whereas in the second stage the reduction rate increases when the basicity increases. Figure 2 depicts three reduction paths along which MnO follows a straight line. Solid MnO phase will be consumed to completion once the liquidus temperature is reached and equilibrium established (Olso *et al.,* 1998). Knowledge of the liquidus composition can provide information on slag characteristics and the kinetics of MnO reduction (Olso *et al*., 1998). Ringdalen *et al.* (2009) stated that equilibrium is not always achieved between the MnO in slag and Mn in the alloy.

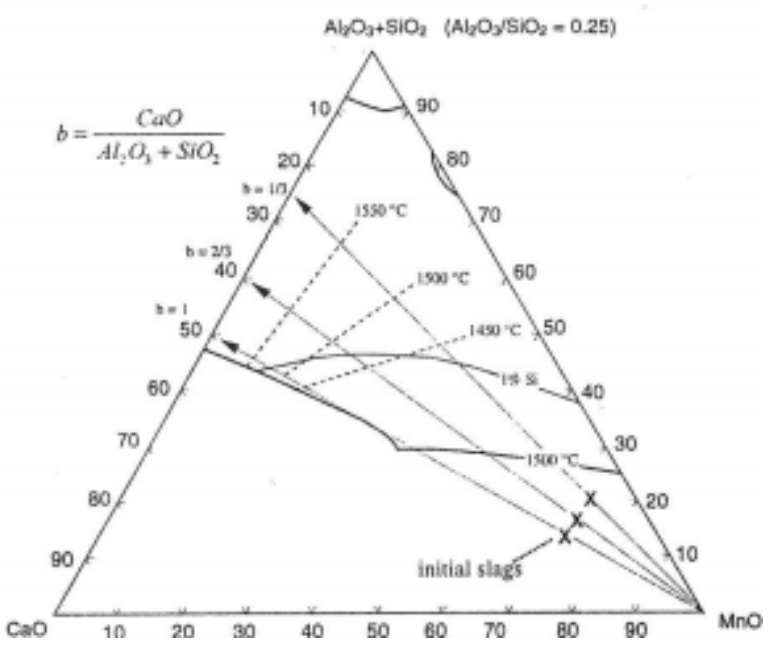

Figure 2: Reduction paths for different basicities, *b*
(from Olso *et al*., 1998)

The mechanism of MnO reduction from slags by dissolved carbon in liquid iron has been studied. Iron in the slag increases the reduction rate by (supposedly) imposing a larger driving force (Tangstad and Safarian, 2010). The introduction of an Fe-Mn-C alloy increases the rate and extent of MnO reduction (Kolbeinsen *et al.,* 2006) and accelerates the graphite-slag reaction (Teasdale and Hayes, 2005). The reduction of MnO was mostly observed at the metal-slag interface by carbon in the metal phase. FeO can also be reduced by CO gas at the slag-gas bubble interface (Safarian and Kolbeinsen, 2008). The mass transfer in the slag is accelerated by movement of gas bubbles through the liquid phase as proposed in a gas-ferrying mechanism (Teasdale and Hayes, 2005).

2.2 Carbonaceous reductants in HCFeMn production

A variety of carbonaceous materials as reductants are used in the ferromanganese production (Sahajwalla *et al.,* 2004). The reductant materials include coal, coal char and coke. Coal is a heterogeneous mixture of organic (plant matter) and inorganic (mineral matter) components. As a result it possesses a variety of chemical and physical differences (Sahajwalla *et al.,* 2004).

The quality of a coal consists in its properties. Those properties, assuming that mineral content and ash are low, are coal type, which shows the proportions and compositions of various macerals, and metamorphic degree, which reflects geochemical and geological processes. These properties strongly influence the physical and chemical composition of a coal, which in turn have implications for the reactivities of various coal types in industrial use (Suarez-Ruiz *et al.*, 2019; Xie, 2015).

2.3 Coal characterization

Six common parameters give the measure of coal quality (see ***Table 2***).

Table 2: Summary of most common coal quality parameters and their implications (Pinheiro, 2006)

Parameter	Desired	Implications as a reductant	Implication as a fuel
Moisture	Low	Negatively affects power consumption	May retard ignition
Volatiles	Variable	Detrimental to power consumption; increases porosity and reactivity; pollution increases	Enough required to allow for ignition. Pollution increases
Ash	Low	Power consumption and slag disposal	Lowers CV and creates disposal issues
Carbon	High as possible	Fundamental	High, provides heat energy
Sulfur	Low	Inorganic S transfers to metal; detrimental, and also formation of SO_x	Pollution, combusts to form SO_x
Rank	Variable	Relates to reactivity; lower for gas-solid reactivity, high for solid-liquid reactivity	Rr<5% preferred, high rank is difficult to ignite

2.3.1 Proximate analysis

Bituminous coal and anthracite are used as carbon-rich reductants in various metallurgical applications. The application of these carbonaceous materials is dependent on specific properties such as carbon content and impurities. In addition, the suitability of various coal processes can initially be evaluated on proximate analysis, on measures such as volatile matter, moisture, and fixed carbon (Xie, 2015). The carbon content of a coal is often the deciding measure in choosing a reductant.

The volatile content of coal contributes to power consumption as the release of the organic volatiles which are mostly endothermic reactions contribute to air pollution (Pinheiro, 2006). Volatile matter is an important parameter in reactivity, as it can be used to determine coal rank (Falcon *et al.,* 2018; Miller, 2013). Coal rank is a critical parameter in determining the suitability of any coal for a process such as coking (Wilberforce and Olivia, 2017

The most obvious implication of moisture in reductants is its contribution to increased power consumption. Any reaction that involves moisture is endothermic and increases power consumption as energy goes into sensible and latent heat to raise temperatures and (inadvertently) produce steam (Bagirathi, 2012).

Ash comprises the impurities that are unwanted in a reductant. Ash reports to slag, which adds to waste being discarded.

2.3.2 Petrographic analysis

Coal petrography, a sub-branch of petrology, studies the organic and inorganic constituents of coal, carbon, and other rocks by means of microscopy (Richards *et al*., 2013; Falcon *et al.,* 2018; Stach *et al.,* 1982). The applied aspects of coal petrography are significant in technological applications (Falcon *et al*., 2018). For instance, in the metallurgical industry coal petrography can provide understanding of the technical performance of coal in carbonisation processes (Falcon *et al.,* 2013). Whilst petrography can provide information that pertains to coal formation and composition, there is still a need for complementary analyses such as chemical analyses to provide a fuller picture of the coal.

Coal composition and coal formation are necessary to put into context the foundations of petrographic analyses. Coal composition relates to the type (organic composition) , maturity (coal rank) , and grade (mineral matter composition).Coalification is a metamorphic process initiated by increasing temperature and pressure, and running for a long time. This results in the transformation of peat through progressive stages. The full transformation runs from lignite through sub-bituminous coal, to bituminous coal, and finally anthracite (see Figure 3; Falcon *et al.,* 2018; Smith and Cook, 1980). Rank refers to the degree of coalification (metamorphism) reached (Falcon *et al.,* 2018; Falcon and Ham, 1988). Rank is a concept that cannot be measured but rather determined petrographically through the physical and chemical properties of a coal (Diessel, 1992).



Figure 3: Coalification process from peat through to bituminous coals with increasing temperature and pressure (Myrvagnes, 2008)

Volatile matter and moisture are the most commonly used rank parameters. Moisture content to determine coal rank is usually applicable in low-rank coals, whereas volatile

matter has been traditionally used for more mature coals. However, vitrinite reflectance is the most acknowledged measure of rank. Vitrinite is chosen as a reliable parameter for rank determination because it displays uniform physical and chemical changes under increasing thermal stress, and because its appearance is homogenous (Mukhopadhyay, 1994).

Generally, volatile matter decreases with increasing coal rank. Rank relates to volatile matter in that it correlates inversely with volatile matter arising from organic constituents (Falcon *et al.,* 2004). The molecular structure of coals changes continuously during the coalification process. In bituminous coals, the amount of volatile matter consists mainly of aliphatic components. During the anthracitic stage, a decrease in hydrogen-carbon ratio corresponds to a re-ordering of aromatic units to a higher degree (see Figure 4).

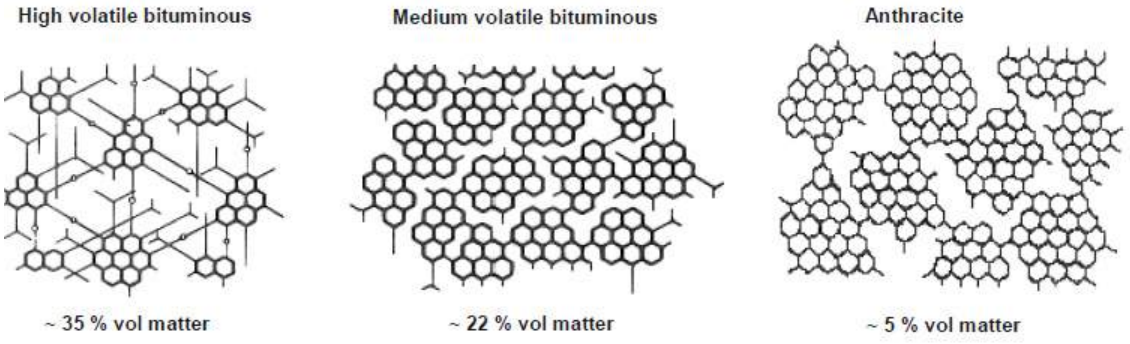

Figure 4: Changes in chemical structure from high volatile bituminous coal to anthracite (Teichmüller and Teichmüller 1968)

Coal composition can be characterized into macroscopic (lithotypes) and microscopic (macerals and minerals) constituents, both of which govern the properties of a coal. Coal type is presented by the formation of the macerals evolving from different plant parts of the original peat (Falcon *et al.,* 2018; Suarez-Ruiz, 2008). Lithotypes are macroscopically identifiable layers in coal seams representing the changes in organic input (Falcon *et al.*, 2018; Falcon, 1987). The bands are identified on the basis of physical properties, such as lustre, fracture pattern, and colour of the coal (Falcon *et al.*, 2018; Suarez-Ruiz, 2008).

The macerals evolved from different organs and tissues of the original plant material from early accumulation to biochemical degradation and then geochemical coalification. (Falcon et al.,2019). The maceral formation during the decomposition of vegetable matter to peat depends on factors such as phytogenic input, acidity (pH), tectonics, and redox potentials (Eh) (Diessel, 1992; Falcon *et al.*,2018). Eh is important in the degradation of plant matter. Under aerobic conditions, the buried, accumulated organic matter undergoes further decay by bacteria to complete disintegration of plant matter (Arnold, 2013; Falcon *et al.,* 2018). These factors ultimately control the process of biochemical coalification and produce the constituents in coal (Pinheiro, 2006).

Most macerals change in physical, chemical, and optical properties with increasing rank. However, their proportions and shape remain unchanged (Falcon *et al.,* 2018). As the rank increases, the differences in physical and chemical properties become less significant because their reflectances converge. The organic matter formed during biochemical degradation (composition or type) and the process of coalification (rank) are independent of one another. O'Keefe *et al*. (2013) state that coal rank is measured by a decrease in moisture and volatile functional groups, leading consequently to an increase in the carbon content of the coal.

Maceral composition, rank, and coal grade are all assessed microscopically. Three maceral groups form the basis of coal petrography, namely, vitrinite, liptinite, and inertinite. They are based primarily on reflectance and physical properties. Each maceral is distinguished by a unique set of physical and chemical properties for a given rank (Chen and Ma, 2002). These properties ultimately determine the behaviour of coal. Each group includes a series of macerals that can be regarded as belonging together, either because of similar origin or because of mode of degradation or preservation (Falcon *et al.,* 2018; Falcon and Snyman, 1986).

Vitrinite is a group that formed from the cellulose and lignin of cell wall material, cell fillings of the woody tissue and colloidal humic gels (Moroeng *et al.,* 2019; Falcon *et al.,* 2018). In appearance, depending on rank, vitrinite appears dark to light grey until white under the microscope. The vitrinite maceral group is defined by the level of reflectance as increased carbon and volatile matter loss relates to the amount of light

reflecting from the surface of vitrinite (Falcon *et al.,* 2018). The higher the carbon content, the higher the reflectance. The chemical structure of vitrinite is made up of moderately aromatic with aliphatic chains found in the bituminous range rank or lower rank coals (Falcon, 2013). With increasing rank, vitrinite becomes more anisotropic (Falcon *et al*., 2018) the aromaticity, condensation and the order of polyaromatic units increase (Suarez-Ruiz, 2008). Vitrinite contains more oxygen and less carbon compared to vitrinite and inertinite, the increase in carbon content and loss of volatile matter occurs linearly with increasing rank (Falcon *et al*., 2008).

Inertinite is a group of macerals derived from plant material that has been altered and degraded in oxidising conditions before or during the peat stage of coal formation (Falcon *et al.,* 2018). They exhibit a high degree of aromatization and condensation (Suarez-Ruiz, 2008). Inertinite formation is also impacted by factors such as redox, biochemical and chemical processes. Literature suggests that inertinite may have formed through biochemical alteration, some derived from peat fires and oxidation by microbial activity and dehydration in an aerobic environment (O'Keefe *et al.*,2013; Falcon *et al*.,2018). The chemical structure of the inertinite group is characterised by highest carbon and lowest oxygen and hydrogen (Falcon *et al.,* 2018; Suarez-Ruiz, 2008). This maceral group exhibits little change in physical and chemical properties with increasing rank, the aromaticity, carbon content, size and shape remain the same through the entire rank process. According to Falcon *et al.,* (2018), inertinite maceral group comprises macerals that may be semi-reactive, particularly in Southern African coals which exhibit low reflectance in low to medium rank coals (Scott and Glasspool, 2007).

Liptinite maceral group includes all the distinct plant parts such as spores, cuticles, suberine cell walls and resins (Suarez-Ruiz; 2008, Maledi, 2017). This maceral group contains the highest hydrogen content and aliphatic compounds in nature. Due to their high hydrogen content, macerals in this group produce high content of tar and gases during the carbonization process (Suarez-Ruiz, 2008). At low and medium rank, liptinite macerals have a lower reflectance than vitrinite; liptinite reflectance generally increases with increasing rank (Picket *et al.,* 2017). Liptinite exhibits the lowest

reflectance of the macerals and as a result, has an appearance that is dark to dark grey or rusty brown in reflected light (Falcon *et al.,* 2018; Suarez-Ruiz, 2008, Picket *et al.,* 2017). Liptinite changes rapidly with rank (Falcon, 2013) and is less aromatic in lower rank coals (Maledi,2017). At ranks above medium volatile bituminous, liptinites disappear due to thermal transformation (Suarez-Ruiz, 2008).

Figure 5 displays the plant origins of the different maceral groups with their corresponding chemical properties and technological applications. The maceral groups depending on rank, can be applied to different technological applications. For instance, in the bituminous coal range, with a decreasing volatile matter, vitrinite rich coal can be applied in an array of technological properties ranging from coke and char making to pyrolysis and combustion.

The rank and maceral composition of coal have great significance to the technological use of the coal (Falcon *et al.,* 2013). As a result, standardised petrographic analytical techniques include composition or type of coal as determined by maceral analysis and rank (Falcon, 2013; Miller, 2013; O'Brien *et al*., 2002; Falcon *et al.,* 2018). Maceral analysis provides quantitative composition of coal in terms of macerals (Suarez-Ruiz and Ward, 2008) and categorises the microscopic constituents of coal according to morphology and reflectance (Miller, 2013). Maceral analysis is important as differences in chemical composition translate to differences in technological properties of coal (Suarez-Ruiz and Ward, 2008). Maceral analysis can be utilized to determine the proportion of reactive to inert macerals to predict certain coal quality parameters (Miller, 2013).

Maceral group	Plant origin	Reflectance: Description	Reflectance: Rank	Reflectance: Reflected light, %	Chemical properties: Characteristic element	Chemical properties: Typical products on heating	Technological characteristics
VITRINITE	Woody trunks, branches, twigs, stems, stalks, bark, leaf tissue, shoots	Dark to medium grey	High vol. to medium volatile Bituminous	0,5 to 1,1 1,1 to 1,6	Oxygen-rich	Light hydrocarbons; Decreasing amounts of volatiles	• Combusts rapidly • Pyrolysis • Hydrogenation/ liquefaction • Coking
		Pale grey	Low volatile Bituminous	1,6 to 2,0			Combusts with little smoke
		White	Anthracite	2,0 to 10,0			• Combusts with no smoke
EXINITE	Cuticles, spores, resin bodies, algae	Black–brown	High vol.	– 0,0 to 0,5	Hydrogen-rich	Early methane gas; Oil	• Combusts very rapidly • Pyrolysis • Hydrogenation/ liquefaction • For bitumen production
		Dark grey	Bituminous	– 0,5 to 1,1			
		Pale grey	Med. vol. Bituminous	– 1,1 to 1,6		Condensates Wet gases (decreasing)	
		Pale grey (= vitrinite) to white shadows	Low vol. Bituminous to anthracite	– 1,6 to 10,0			
INERTINITE	As for vitrinite, and oxidized detrital organic humus	Medium grey	High vol. Bituminous	0,7 to 1,6	Carbon-rich		• Combusts slowly • Maintains flame • Relatively inert in coking hydrogenation liquefaction pyrolysis
		Pale grey	All bituminous				
		White	coals and anthracite	1,6 to 10,0			
		Yellow white					

Figure 5: Maceral groups with their formation origins and typical morphology (Falcon and Ham, 1988)

The microscopic constituents of coal include the inorganic matter which is made up of mineral matter. Mineral matter includes minerals and other inorganic materials occurring in coal (Suarez-Ruiz, 2008). Coal grade reflects the extent to which the inorganic material has contaminated the accumulation of plant debris (O'Keefe *et al.,* 2013). A high-grade coal is reflected by low proportions of mineral matter (Suarez-Ruiz and Ward, 2008). The minerals can be classified as silicates, sulfides, carbonates, oxides and hydroxides (Finkelman *et al.,* 2019; Maledi, 2017). According to Finkelman *et al.,* (2019) minerals play a significant role in affecting the utilisation of coal from mining to technological applications.

Minerals undergo reactions such as thermal decomposition, disintegration and agglomeration (Chakravarty *et al.,* 2015). The minerals are also known as the primary source of fly ash particles, bottom ash and boiler slag (Finkelman *et al.,* 2015). Inherent

and excluded mineral matter undergo chemical and physical changes during coal conversion processes (Maledi, 2017). For example, excluded mineral matter tends to transform into coarse ash particles and the ash composition is usually of similar composition to the original mineral matter. Inherent mineral matter, associated with organic matter, may coalesce at high temperatures resulting in change of ash particle size and chemistry transformation (Krishnamoorthy and Pisupati, 2015). But the most significant influence of mineral matter is dilution of the organic matter which constitutes the coal grade.

2.3.3 Reactivity analysis

Reactivity tests assess the reactivities of carbonaceous materials in reacting with phases such as slag and CO_2. The reductant partakes in reduction reactions in two main ways: through gasification to form CO, which is dominant in the upper furnace, and direct reduction of carbon with slag (Pistorius, 2000; Sahajwalla *et al.,* 2004). This means that CO_2 and slag reactivity are critical parameters and play a significant role in furnace performance (Monsen *et al.,* 2004).

CO_2 reactivity tests are based on the gasification of carbonaceous materials in the presence of CO_2 (Sahajwalla *et al.,* 2004). Blast furnaces are still used in the ferroalloys industry (Madias, 2011) but not as widely as SAF's. For blast furnace applications, a most widespread standardised CSR (Coke strength after reaction)-CRI (Coke reactivity index) test to characterise coke degradation has been described by Lundgren *et al.,* (2009). The process involves the coke sample heated in a reactor at 1100°C in an inert atmosphere (ASTM D5341). Subsequently, the coke is degassed isothermally in a 100% CO_2 atmosphere then cooled with nitrogen gas. Moreover, to measure the mechanical degradation as denoted by CSR –CRI parameters, the cooled coke is tumbled and sieved (+10mm-0.5mm), the sieved +10mm represents CSR. The CRI or coke reactivity is determined according to Reaction 5**.**

For SAF applications, other techniques have been developed to assess CO_2 reactivity. The technique uses a standardised technique of thermogravimetry (TG) to assess CO_2 reactivity, observing mass loss behaviour as a function of time and temperature as relating to reactivity. A method was conducted by Lindstad *et al.* (2004) using

thermobalance at controlled temperatures of 900°C, 1000°C and 1100°C with either a mixture of 25% CO_2-75%CO or 50%CO_2-50%CO. The furnace was evacuated with Ar gas and later replaced with CO-CO_2 when the Boudouard reaction was initiated. In addition, a developed method by NTNU/SINTFEF that simulates close to upper furnace atmosphere is carried out in a 75% CO-25% CO_2 atmosphere at 1000°C or 1100°C (Monsen *et al.*, 2004, Monsen *et al.*, 2007).

A number of techniques have been developed to assess the potential of slag to react with carbon materials (Monsen *et al.*, 2007; Safarian and Tangstad, 2010):

- *Thermogravimetry*—Monsen *et al.* (2004) conducted tests for slag/charcoal and slag/coke in a CO atmosphere at 1600°C for 60−90 minutes. Crucibles were made from large pieces of reductant and filled with synthetic slag. The reduction experiments were carried out with the calcined reductants at 1200°C and 1600°C for 3 hours before the experiments. The results reported a good slag reactivity for the coke and charcoal tested. The drawback of this technique is challenges with preparing reductant crucibles.
- *ASEA Induction furnace*—This technique assesses the reduction of MnO and SiO_2, according to Reaction 7 and 8, in a graphite crucible in an induction furnace. Both synthetic and industrial slag were tested and the reductants chosen were charcoal, metallurgical coke, anthracite, and petrol coke. The study concluded that it is not ideal to perform slag-carbon reactivity in a graphite crucible in an induction furnace due to the additional supplied inductive energy by the graphite crucible.
- *Sessile drop technique* – A wettability approach that investigates the contact between a solid substrate and a liquid phase. This method has been proven advantageous to the thermogravimetry method due to possibility of preparing a more homogenous substrate. It is also preferred over the ASEA induction technique as no crucible is used. The carbon substrate is placed in a graphite sample holder and a slag piece positioned on the carbon substrate. The procedure entails the chamber furnace initially evacuated and then heated with Argon gas over the sample. The furnace is then rapidly heated to 1500°C at a rate of 120°C/min and held for 15, 30, and 60 minutes at reaction temperature and subsequently cooled rapidly. Slag-

carbon reactivity using the sessile drop technique can be evaluated by considering factors such as, contact angle and slag volume changes, slag chemical composition, and gas outlet analysis.

2.4 Effect of petrographic constituents on reactivity

Relating reactivity to petrographically determined constituents is important in order to understand the influence of petrography of feed coals and how they could potentially perform during high carbon ferromanganese production.

There is however, limited literature on the influence of petrographically determined constituents on reactivity of solid carbon with CO_2 and slag components. Extensive research is available on the structural transformation of macerals and their change in chemical reactivity during processes such as pyrolysis and carbonization. There are different technological applications for petrographic study in the metallurgical industry. For instance, the metallurgical industry depends on petrographic assessment of coal for processes such as carbonization to produce quality coke. Coal utilization processes, such as combustion, also benefit from petrographic assessment. The chemico-physical behaviour and thermo-chemical transformation of coal for industrial use has been proven to be especially dependent on its petrographic make-up (Choundary *et al.,* 2008). The maceral content in a particular coal greatly influences the coal properties which affects its thermal behaviour.

Reactivity in petrography holds a unique meaning. Generally, the maceral groups are divided into reactive and unreactive groups, as seen in Figure 6 on the basis of change in structure and shape when heated (Falcon *et al.,* 2018). Reactive macerals have a lower carbon-to-hydrogen ratio as compared to non-reactive macerals (Malumbazo, 2012). Whilst inert forms of inertinite macerals at any rank will not combust easily and require more heat (Falcon and Ham, 1988).

Maceral Sub-group		Maceral group name
Reactive	Sporinite, Cutinite, Resinite Alginite	Liptinite
	Collinite Tellinite	Vitrinite
	Reactive-Semifusinite	Inertinite
Non-Reactive	Inert Semi-fusinite Fusinite Macrinite Scleronite Micrinite Inertodetrinite	Inertinite

Figure 6: Reactive and non-reactive macerals (Falcon and Snyman, 1986)

The behaviour of coal organic constituents (macerals) upon heating in technological applications has been explored. During processes such as pyrolysis, thermal behaviour of particles can be assessed petrographically. Vitrinite and inertinite differ in pyrolysis behaviour for example macerals inert in nature do not react or change in size. Contrastingly, reactive macerals soften, release volatile matter resulting in char formation (Falcon *et al.,* 2018).

Coal petrography can also be used to evaluate coal for coking purposes. Carbonization is the process of making coke from 'coking coals' (Falcon *et al.*, 2018). A study was conducted by Gray *et al.*, (2000) to establish a relation between SiO gas reactivity and petrographic characteristics: the study found that SiO reactivity decreased with increased rank. The coke properties are related to coal properties such as coke corresponding to a high content of reactive macerals in vitrinite coals. The study also found that reactivity generally increased with increased binder phase from reactive macerals.

The reactive macerals are thermally altered in the coking process and form the binder phase. Inert macerals such as inertinite do not change significantly in the coking process and reinforce the cell walls and as a result form filler phase in cokes. However, studies show that reactive macerals especially Gondwana coals produce better coke

quality than vitrinite rich Northern Hemisphere coals (Malumbazo *et al.*, 2012). As mentioned by Falcon *et al.,* (2018) for any vitrinite there is a proportion of inertinite needed to provide strength for coke walls. A study conducted by Raaness and Gray (1995) to characterize parent coals, as well as coal chars and coke, found that reactivity generally decreased with increasing rank. Coals high in reactive macerals produce coke that has a high reactivity towards CO_2. The carbon forms in the binder phase of the coke are based on rank as determined by vitrinite reflectance (Gray and Devanney, 1986).

2.5 Research questions

The study investigates the potential effect of the petrographic characteristics of coal or anthracite on the reactivity of reductant to slag during the production of high-carbon ferromanganese (HCFeMn) by addressing the following two questions:

1. Does coal rank have an effect on slag reactivity?
2. Does the maceral analysis have an effect on slag reactivity?'

2.6 Research objectives

- Source and prepare raw materials
- Characterize raw materials such as reductants and already reduced slag sourced from an HCFeMn producer
- Develop and conduct tests in a gas-tight muffle furnace to measure reductant reactivity to slag (mass loss as a function of time and temperature)
- Characterize reacted samples to study maceral interaction with slag and reaction products formed

3 TEST PROCEDURE

3.1 Source and prepare raw materials

Three reductant samples as seen in Figure 7 were sourced from a South African producer of manganese ferroalloys. These samples, indicated in Figure 7, are described as coal 1, coal 2, and anthracite.

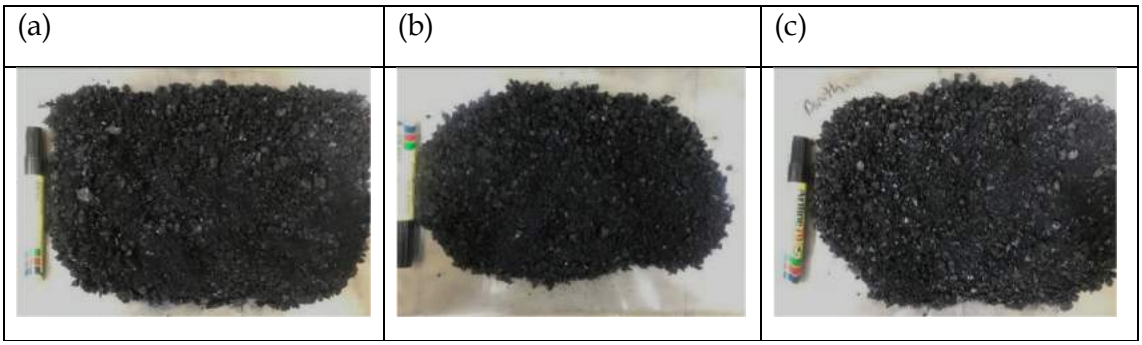

Figure 7: As-received carbonaceous reductants (a) coal 1 (b) coal 2 and (c) anthracite

The preparation flowsheet in Figure 8 presents the steps undertaken for the sample preparation of the coal samples.

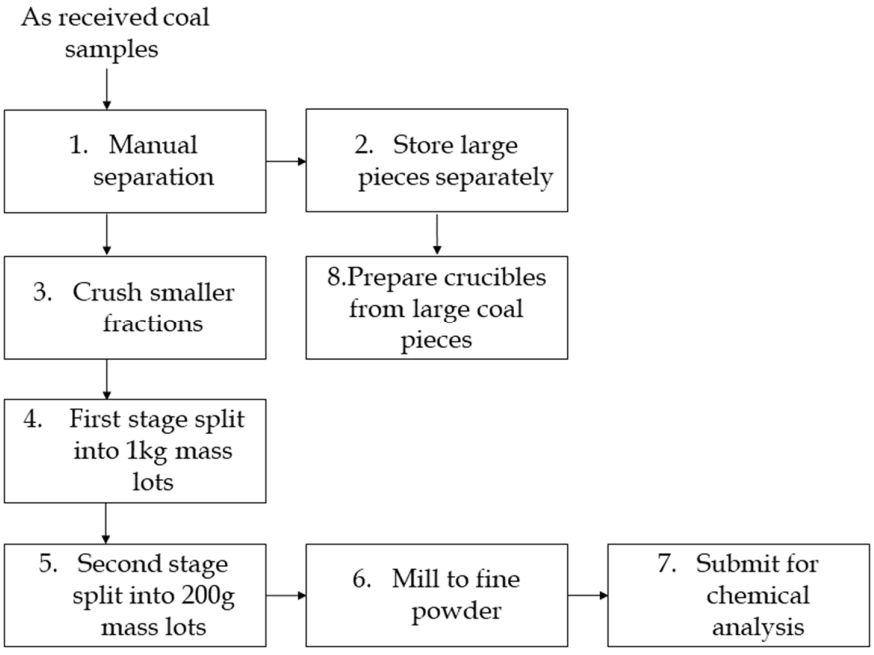

Figure 8: Coal sample preparation flow sheet

1. The coal samples were composed of a mixture of fairly large lumps of coal, to be used to make crucibles that will contain the slag, and also the smaller fractions for characterisation
2. The selected large lumps were stored to be used to prepare the reductant 'crucibles' (see Step 8)
3. The smaller fractions of the coal samples were prepared in accordance to ISO 78283:2006. The as-received coal samples were weighed before being stage crushed using a jaw crusher. The −3 mm fractions were screened out
4. The representative +3 mm crushed fractions were further split using a rotary splitter to 1 kg mass lots
5. A second stage splitter was utilised, where the crushed fractions were split into 200 g lots
6. The +3 mm split fractions were milled to powder form to ensure homogeneity using a pulverizing tungsten carbide disc mill
7. The milled representative samples were submitted for chemical analyses
8. The preparation of reductant 'crucible' process involved selecting large lumps from the as-received carbonaceous reductants. For each reductant type, 'crucibles' were prepared from the large lumps of the carbonaceous reductants by drilling using a diamond core bit for tiles (30 mm diameter) to minimize breakage of the crucibles and dust generation. During the drilling process, a hollow space is created first before chiselling out the outside of the 'crucible' for the desired shape and size as seen in Figure 9 that can fit into a A5 size alumina crucible (dimensions of 75 mm H, 42 mm ID,49 mm OD and thickness of 3 mm). The dimensions of the reductant 'crucibles' prepared were fairly similar in size with an inner diameter ranging between 25−27 mm, thickness of 7−10 mm and height of 50 mm

The drawbacks of this method were

- Sourcing large enough lumps that will not break easily when drilled as coal is a brittle material
- Drilling the carbonaceous reductants was also challenging especially coal 1 and coal 2 as they were more prone to breaking than the anthracite

- Coal is naturally a heterogeneous material and no two coals can be the same. Manually selecting the large lumps potentially created some uncertainty in terms of representation. This means that the 'crucibles' of the same type of reductant could behave differently during the reactivity tests and not be attributed to the differences in chemical specifications

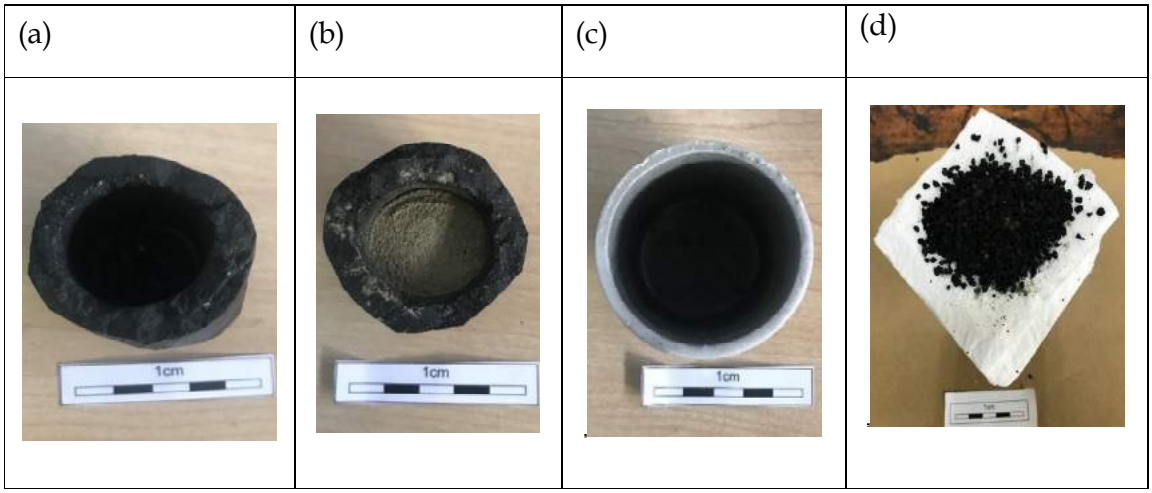

Figure 9: Photographs of the prepared reductant crucible from the large lumps for the reactivity tests. (a) Drilled reductant to prepare 'crucible', (b) The reductant 'crucible' filled with HCFeMn slag, (c) Alumina crucible used for containing 'crucible' and slag, (d) Refractory board placed on top of the alumina crucible with 'crucible' and slag inside.

The industrial HCFeMn slag samples in Figure 10 were sourced from one of the South Africa's HCFeMn producers. The flowsheet in Figure 11 presents the steps taken to prepare representative slag samples.

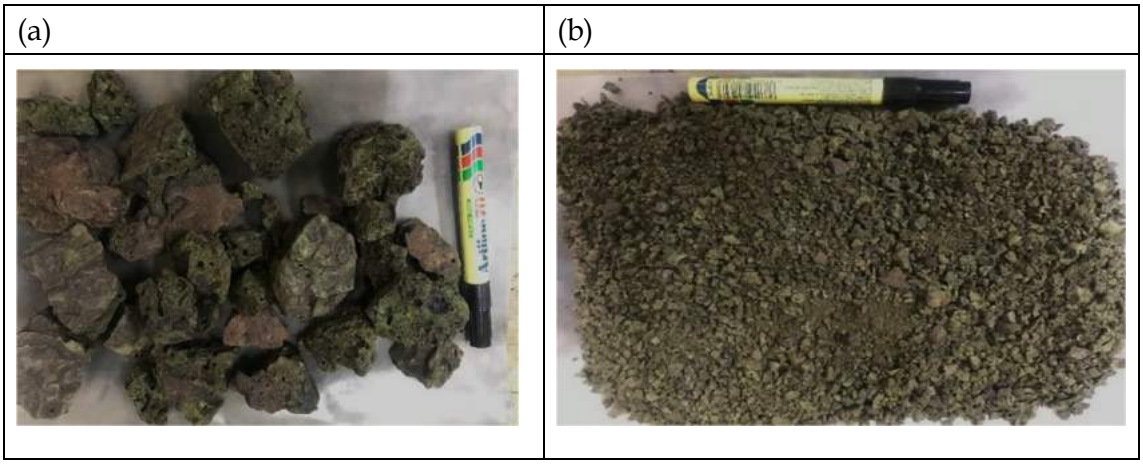

Figure 10: HCFeMn slag sample (a) as-received HCFeMn slag before crushing (b) crushed HCFeMn slag

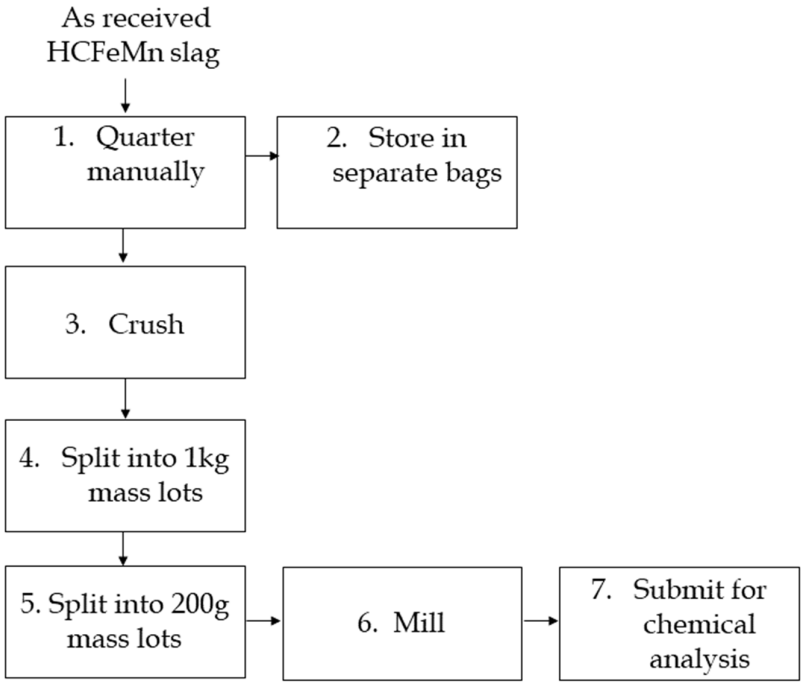

Figure 11: HCFeMn slag sample preparation flowsheet

1. To obtain representative samples the as-received slag samples were quartered manually and stored in separate bags
2. One bag was subsequently crushed, using jaw crusher, to achieve the desired size suitable for milling
3. The industrial HCFeMn slag was initially crushed and screened to −3 mm
4. The crushed slag was split using a rotary splitter to 1 kg mass lots
5. The slag sample was further split into 200 g mass lots
6. The crushed slag was milled to powder form to ensure homogeneity using a pulverizing Tungsten carbide disc mill

3.2 Characterize raw materials

3.2.1 Bulk chemical composition

The bulk chemical compositions of the prepared milled representative coal samples were determined by proximate analyses and X-ray fluorescence (XRF). Whilst the bulk chemical compositions of the HCFeMn slag samples were determined by XRF and Inductively Coupled Plasma-Optical Emission Spectrometry (ICP-OES) to assess major elemental composition.

Proximate analyses (ASTM D3173-11; ASTM D3174-12; ASTM D3175-11) is a suite of analyses used to examine the chemical composition of coal samples that covers moisture content, fixed carbon (by difference), volatile matter and ash. The basis for reporting moisture is as follows (Falcon *et al.,* 2018; Zhu, 2014):

- As received (ar)—refers to total moisture (including both surface and inherent moisture)
- Air dry (ad)—the stable moisture content when equilibrium has been reached with the humidity of the laboratory
- Dry—analysis is reported based on assumption that coal is completely free of moisture
- Dry ash-free (daf)—value is based on a hypothetical situation that sample is completely free of moisture and ash

Volatile matter, fixed carbon and ash are reported on a dry ash free basis. The ash percentage is calculated from the mass of residue remaining after combustion divided by the original mass of the sample used in the procedure. Volatile matter is measured as the percentage loss in mass, adjusted for moisture when coal is heated in absence of oxygen. The volatile matter is calculated from the loss in mass of the analysis sample after making allowance for the loss in mass due to moisture (Miller, 2013). Fixed carbon is the solid combustible residue that remains by calculating removal of moisture, ash, and volatile matter from 100%.

XRF is a non-destructive analytical technique used to determine the elemental composition of materials by measuring the secondary X-ray emitted from a sample when excited by a primary X-ray source, radioisotope or electron beam (Janssens, 2014). The method entails the samples directed with high energy X-rays. ICP- OES is an analytical method that uses emission spectra of a sample to detect and measure elements. It is a conventional spectroscopic technique (Thompson and Walsh,1989) that uses the inductively coupled plasma to produce excited atoms and ions to emit electromagnetic radiation at wavelengths representing of a particular element (Boss and Fredeen,2004). The principle of ICP is based on an atom becoming excited then an electron from the atom is moved from the ground state orbital into a high energy level

known as an excited state (Boss and Fredeen, 2004). ICP is an analytical method used to detect and measure elements through the ionisation of a hot plasma usually made from argon or other gases such as Helium and Nitrogen (Thompson and Walsh, 1989).

3.2.2 Bulk phase chemical composition

The as-received HCFeMn slag representative sample was milled to 80% −75 μm and subsequently micronized for XRD analysis, in order to ensure a homogenized sample, and reduce particle sizes, to allow each particle probability of exposure to X-rays. The micronized sample was analysed by a Bruker D8 Advanced diffractometer, with a Lynxeye detector and variable divergence- and fixed-receiving slits, with Fe filtered Co-Kα radiation. The analysed phases were identified using the DIFFRAC.SUITE TOPAS software package, which is based on Rietveld Refinement and fundamental parameters approach.

3.2.3 Specific phase-chemical composition

SEM-EDS was used for identification of specific phases of the as-received slag phases. The samples were taken for polishing through a series of grinding papers and polishing cloths, with water, on an automated polisher. Subsequently, the samples were coated with carbon to improve the imaging of samples by creating a conductive layer on the sample to inhibit charging. The SEM instrument used was a ZEISS Sigma 300VP with field emission gun and ZEISS 'Smart SEM software. The EDS detector used was OXFORD INSTRUMENT X-act PentaFET Precision with Oxford INCA software. The surface of the sample was initially cleaned with a cloth and sprayed with dry air to ensure that the surface is free from loose particles. The coated samples are positioned on an aluminium stub, by use of a double-sided tape, and placed inside the instrument stage. The chamber is allowed to vacuum before proceeding with the sample analysis. The chamber is evacuated in order to prevent the atmosphere from interfering with the electron beam or X-ray.

3.2.4 Petrographic analysis

Petrographic analysis is a technique used to determine the organic and inorganic (mineral matter) composition of coal samples. The three-parent coal samples (coal 1, coal 2 and anthracite) were prepared in accordance to SABS ISO 7404-2. The samples

were initially crushed to −1 mm and the −30 µm sieved out. The 1 mm sample was mixed with epoxy resin and hardener and moulded as a block mount. It was left to cure in vacuum for 24 hours. The final stage involved grinding and polishing of the surface of each block with a 0.05 µm OPS lubricant, using a Struers Tegraforce polisher to create a clean, flat scratch free surface. Microlithotype and maceral analyses were determined by use of a Zeiss Axio Imager M2m petrographic microscope, fitted with a Fossil Hilgers system for reflectance determination. The reflected light microscope is fitted with a ×10 dry air lens and a ×50 oil immersion lens, leading to a total magnification of ×100 and ×500 respectively. The Zeiss Axio Imager M2m reflected light microscope is equipped with an oil immersion objective lens, to allow high-resolution colour images at a magnification of 500x. The immersion oil used to enhance reflectivity differences was a Zeiss immersol 518N.

Before using the Zeiss Axio Imager M2m reflected light microscope, the sections were mounted on a slide using a levelling press to level the section. The polished heat-treated sections were initially assessed at magnification of x100, without oil, using the air-dry lens. Subsequently, 500× magnification was used to study the sections under colour camera. The heat-treated samples are only viewed under 500× magnification for microscopic images. The parent coals under 500× were analysed for reflectance, microlithotypes and maceral analyses.

The maceral analyses were conducted according to ISO 7404-03 where an automated point-counting stage at traverse spacing of 0.4 mm and intervals between the traverse of 0. 5 mm. At least 500 points are counted under the cross hair, and all macerals are included in the count (not determined by calculation). The 0.900 YAG calibration standard was used and the results are presented in volume per cent (vol %). Reflectance measurements are taken on a smooth scratch free surface and carried out in monochromatic green light by means of a photomultiplier. The results were reported as the mean random reflectance and standard deviation is always included.

3.3 Reactivity test

The muffle furnace type tests were conducted to study reductant reactivity to slag and reporting mass loss as a function of time and temperature. An Ultrafurn gas tight

chamber furnace was utilised and presented in Figure 12. It had workable chamber dimensions (H × W × D) of 175 mm × 195 mm × 175 mm with a schematic experimental set-up in Figure 13. The furnace was equipped with Molybdenum Disilicide ($MoSi_2$) heating elements, with maximum operating temperature of 1800°C, but a maximum of 1700°C was recommended to extend the lifetime of the elements. A CAHO P961 programmable controller was used to set the targeted temperature at a specific heating rate of 10°C/min to the target reaction time and set temperature of 1500°C. To measure the control temperature, a B-type furnace thermocouple is connected to the rear of the furnace.

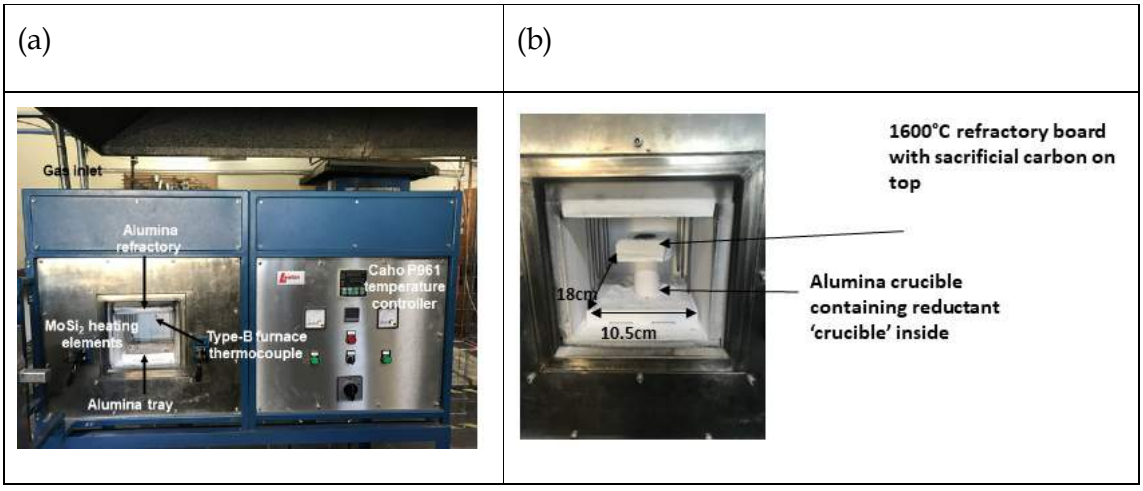

Figure 12: Experimental set-up used for the carbonaceous reductant reactivity on slag tests (a) Gas tight chamber furnace (b) Sample set-up inside chamber

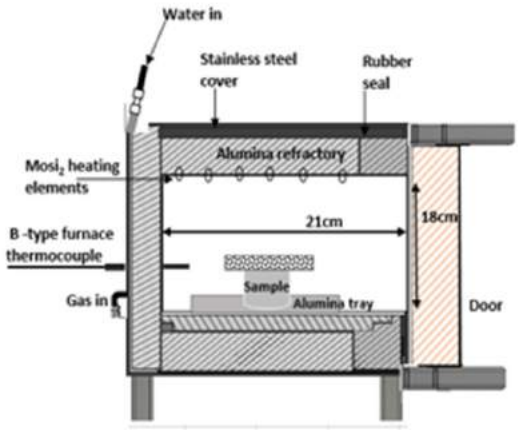

Figure 13 : Schematic layout of the experimental set-up

The method used for the carbonaceous reductant reactivity to slag is summarized in Figure 14:

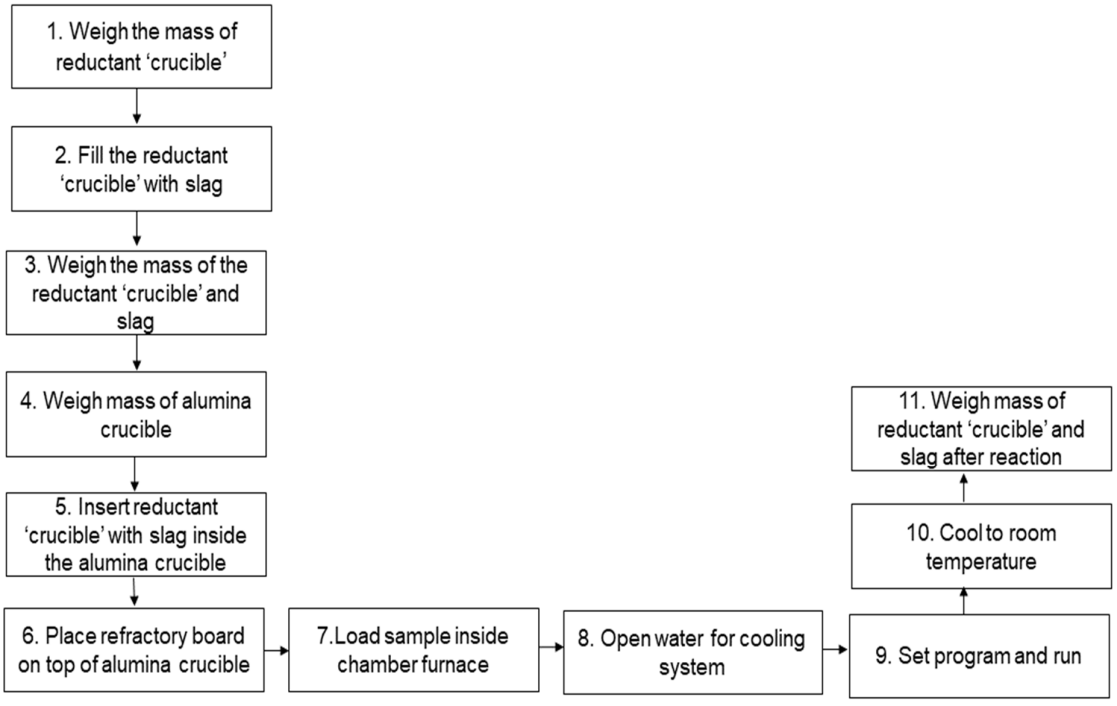

Figure 14: Method for chamber furnace reactivity tests

For the muffle furnace type tests, a procedure was developed,

1. The empty reductant 'crucibles' were weighed
2. The reductant 'crucibles' were filled with the milled slag
3. The combined mass weighed and recorded. The mass of the slag before reaction is determined by difference. The average mass of slag filled inside the reductant 'crucible' recorded before heat treatment varied between 10 g and 17 g.
4. The alumina crucible was weighed and the mass recorded
5. The reductant 'crucibles' filled with the slag were placed into size A5 alumina crucibles which served as containment vessels, in case of leakages, and aided in positioning the reductant crucibles in the gas tight chamber furnace
6. In order to scavenge any oxygen that could potentially enter the chamber, a refractory board topped with activated carbon was placed as lid to the alumina crucible.

7. The sample was inserted inside the heating chamber, placed on top of the alumina tray
8. Before introducing the Argon (Ar) gas the chamber door was closed tightly. The gas was introduced to evacuate the chamber for approximately 30 minutes.
9. Once purging was completed, the cooling water system was opened.
10. The furnace was switched on and the program set to 1500°C with a targeted reaction time using the CAHO P961 temperature controller according to **PDD-SOP-784 in APPENDIX B.** One sample was placed at a time for the specific set reaction time and temperature.
11. Once the reaction time lapsed, the furnace was stopped. The sample was kept inside the chamber and allowed to cool down overnight to room temperature whilst the Ar gas was still flowing continuously.
12. Once cooled, the sample was removed from the furnace. The reacted reductant 'crucible' with slag was removed from the alumina crucible and the combined mass of the reductant 'crucible' and slag determined by weighing.
13. The mass of slag and reductant after reaction allowed for determination of %mass loss as a function of reaction time and temperature.

$$\Delta m = m_i - m_f \quad [9]$$

Where

Δm = mass difference in g

m_f = final mass in g

m_i = initial mass in g

$$\%\Delta m = \frac{\Delta m}{m_i} \times 100 \quad [10]$$

Therefore,

$$Mass\ loss\ \% = \frac{\Delta m}{m_i} \times 100 \quad [11]$$

Where

Δm = (Initial reductant 'crucible' mass + slag) − (final reductant 'crucible' mass+ slag mass) in g

m_i = initial mass of reductant 'crucible' + slag in g

3.4 Characterization of post-mortem samples

SEM-EDS was used for identification of specific phases of the heat-treated slag and alloy phases formed as a result of carbothermic reduction. The height of the heat-treated, unpolished samples in resin from the base was initially reduced in size to 1.5 cm or less in order to fit in the specimen chamber without interference. The samples were taken for polishing through a series of grinding papers and polishing cloths, with water, on an automated polisher. Subsequently, the samples were coated with Au-Pd to improve the imaging of samples by creating a conductive layer of metal on the sample. Au-Pd was used in this instance instead of carbon because the heat-treated samples already contain carbon source from the carbonaceous reductant.

4 RESULTS

4.1 Material characterization

Section 4.1 presents results of the characterization of the as-received slag and carbonaceous reductants. Presented is the chemical analysis, bulk chemical analysis, specific phase chemical analysis and petrographic analysis conducted on the parent coals. Characterization of post-mortem results includes macroscopic observations and microscopic observations in the form of petrographic observations.

4.1.1 Chemical analysis

The results obtained from the proximate analysis of coal 1, coal 2 and anthracite are presented in Table 3**.** The results indicated that Anthracite had the highest fixed carbon at 78.1% whilst coal 1 and coal 2 had similar fixed carbon content determined on a dry basis of 55.0% and 52.1% respectively. In terms of volatile matter, coal 2 consisted of the highest volatile matter reported at 29.3%, followed by coal 1 at 27.7% and, Anthracite the least volatile matter content at 5.4%. The moisture content and ash content were similar in all three studied parent coals. The determined moisture content ranged between 3.2% and 3.9% and the ash yield between 16.3% and 17.4%.

Table 3: Proximate analyses of the reductant samples

Sample ID	**Inherent moisture**	**Volatile Matter**	**Ash %**	**% Fixed C**
	%	%	**Dry Basis**	**Dry Basis**
Anthracite	3.9	5.4	16.3	78.1
Coal 1	3.2	27.7	16.3	55.0
Coal 2	3.9	29.3	17.4	52.1

The ash compositions presented in Table 4, Table 5 and Table 6 contain calculated average values, sum and standard deviation of the three carbonaceous reductants (coal 1, coal 2 and anthracite). According to the ash chemistry analyses, SiO_2, Al_2O_3, Fe_2O_3, and CaO are the major elemental oxides present. SiO_2 was the most dominant major oxide element present in all the three reductants with anthracite containing the highest concentration on average of 54.8% followed by coal 2 with 51.2% and coal 1 with the least SiO_2 concentration of 41.4%. Si found in coals occurs mostly as quartz and clay minerals (Maledi, 2017). The second most dominant major oxide found in the ash chemistry analyses was Al_2O_3 for all three carbonaceous reductants, with Coal 2 and Coal 1 consisting of similar concentrations of 27.9% and 27.7% respectively. Al is found primarily in the coal as clay minerals. This indicates that clay and silicates are the dominant mineral matter occurring in the investigated carbonaceous reductants.

Coal 1 consisted of the highest concentration of CaO at 12.0% followed by coal 2 at 6.7% and the least concentration of anthracite at 2.61%. Moreover, anthracite also contained the highest Na_2O at 3.0% and undetected limits for coal 1 and coal 2. Sulfur is present in the form of SO_3. From the ash chemistry analyses, SO_3 was in highest concentration in coal 1 at 5.5%.

Table 4: Ash oxide analyses of major and minor elements as determined by XRF for coal 1

n. d= not detected

Ash components	Sample Identification				
	Coal 1				
	1A	1B	1C	Average	Std. Dev
Al_2O_3	24.3	24.5	23.5	24.1	0.5
CaO	12.0	12.7	11.4	12.0	0.7
Cr_2O_3	0.04	0.05	0.05	0.0	0.01
Fe_2O_3	8.3	8.7	12.1	9.7	2.1
K_2O	0.7	0.7	0.6	0.6	0.04
MgO	2.8	2.7	2.7	2.7	0.08
MnO	0.4	0.4	0.5	0.5	0.02
Na_2O	0.2	0.2	0.3	0.2	0.02
P_2O_5	0.1	0.1	0.1	0.1	0.02
SiO_2	43.9	42.6	41.4	42.7	1.3
TiO_2	0.9	0.9	0.9	0.9	0.01
V_2O_5	0.03	0.03	0.03	0.0	0.0
ZrO_2	0.06	0.06	0.06	0.06	0.0
BaO	0.2	0.2	0.2	0.2	0.0
SrO	0.2	0.2	0.2	0.2	0.0
ZnO	0.01	0.01	0.01	0.0	0.0
SO_3	5.7	5.3	5.6	5.5	0.19
Total	99.9	99.5	99.6		

Table 5: Ash oxide analyses of major and minor elements as determined by XRF for coal 2

Ash components	Sample Identification				
	Coal 2				
	2A	2B	2C	Average	Std. Dev
Al_2O_3	27.4	28.8	27.6	27.9	0.8
CaO	7.1	6.3	6.6	6.6	0.4
Cr_2O_3	0.04	0.04	0.06	0.05	0.01
Fe_2O_3	4.1	4.8	8.8	5.9	2.5
K_2O	0.7	0.7	0.7	0.7	0.03
MgO	2.2	2.3	2.1	2.2	0.1
MnO	0.3	0.1	0.2	0.2	0.08
Na_2O	0.02	nd	nd	0.02	nd
P_2O_5	0.1	0.1	0.1	0.10	0.00
SiO_2	53.3	51.9	48.2	51.2	2.6
TiO_2	1.1	1.1	1.1	1.1	0.02
V_2O_5	0.03	0.02	0.03	0.03	0.01
ZrO_2	0.06	0.06	0.06	0.06	0.00
BaO	0.2	0.2	0.2	0.2	0.01
SrO	0.2	0.2	0.2	0.2	0.01
ZnO	0.01	0.01	0.01	0.01	0.00
SO_3	2.9	3.2	3.6	3.2	0.3
Total	99.7	99.7	99.3		

Table 6: Ash oxide analyses of major and minor elements as determined by XRF for anthracite

Ash components	Sample Identification				
	Anthracite				
	3A	3B	3C	Average	Std. Dev
Al_2O_3	27.2	27.8	27.9	27.7	0.4
CaO	2.6	2.53	2.7	2.61	0.09
Cr_2O_3	0.06	0.04	0.04	0.0	0.01
Fe_2O_3	4.8	4.7	4.4	4.6	0.2
K_2O	2.0	1.9	1.9	1.9	0.07
MgO	1.4	1.5	1.5	1.5	0.04
MnO	0.1	0.1	0.1	0.1	0.01
Na_2O	3.2	2.9	3.0	3.0	0.1
P_2O_5	0.2	0.2	0.2	0.2	0.02
SiO_2	54.6	55.2	54.5	54.8	0.4
TiO_2	1.3	1.3	1.3	1.3	0.05
V_2O_5	0.03	0.03	0.03	0.0	0.00
ZrO_2	0.06	0.07	0.07	0.1	0.01
BaO	0.2	0.0	0.2	0.2	0.01
SrO	0.2	0.2	0.2	0.2	0.01
ZnO	0.01	0.01	0.01	0.0	0.00
SO_3	1.9	1.8	1.9	1.9	0.08
Total	99.9	100.0	99.8		

Ash chemistry complements the petrographically determined mineral matter content. The ash oxides determined from ash chemistry provide an indication of the occurring minerals in the coal, providing a relationship between the ash oxides and mineral matter. The mineral matter results indicated that Coal 1, Coal 2 and Anthracite were dominated by clays, quartz, pyrite and carbonates as seen in Figure 15. Quartz was reported as the dominant mineral, in Coal 1 present at 3.9%, 2.9% in Coal 2 and 2.0% in Anthracite. Carbonate minerals on the other hand were dominant in Anthracite and Coal 2 at 2.6% and 2.9% respectively. Pyrite existed below 2% for all the studied coals whilst the clay mineral was most abundant in Coal 1.

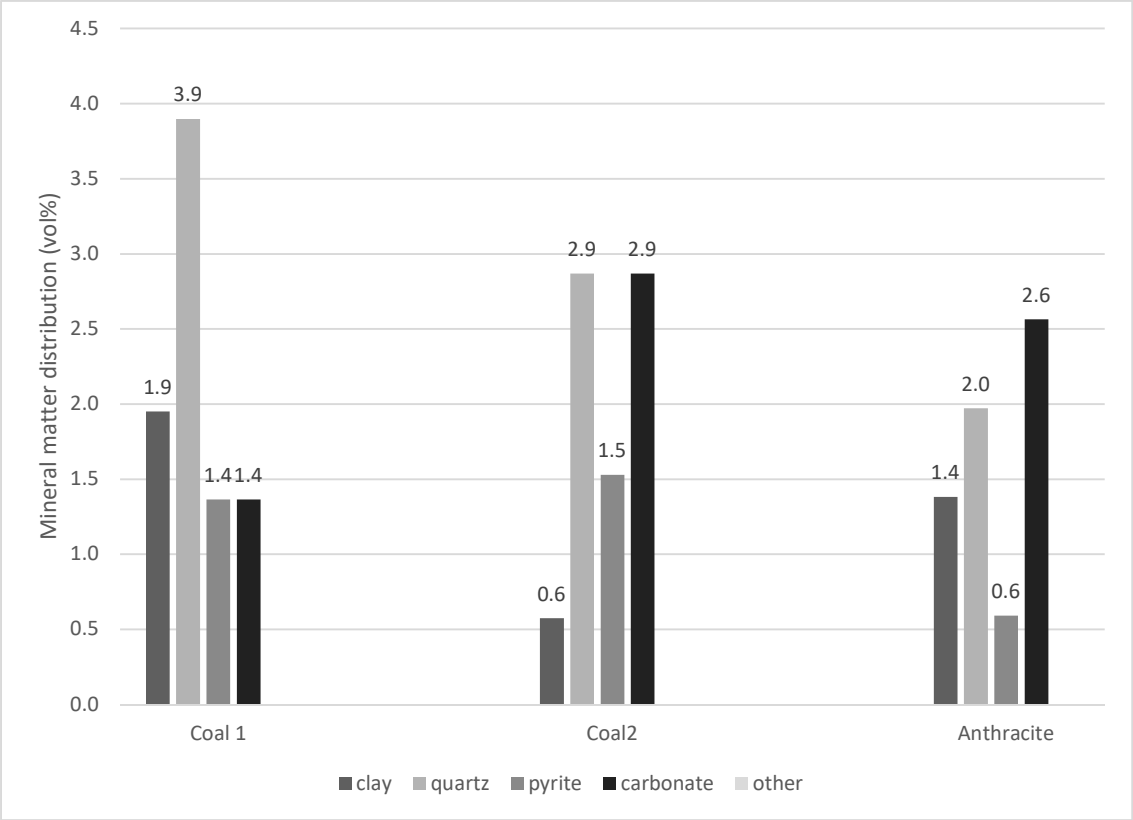

Figure 15: Determined mineral matter distribution across Coal 1, Coal 2 and Anthracite

The chemical composition of the as -received HCFeMn slag was determined by XRF as reported in Table 7 and by ICP method in Table 8. The bulk chemical analysis of the slag as determined by XRF and ICP methods both show that the major species in the slag are MnO, CaO and SiO_2. The ICP method with a higher MnO average of 23.4% and MnO by XRF reporting an average of 21.5%. The CaO content is also slightly higher in the XRF method on average at 31.1% and 29.4% in the ICP method. The ICP method differed from the XRF results in that it reported species such as BaO, TiO_2 and K_2O which were not picked up by the XRF method. The ICP method seemed as the most reliable method because the aforementioned species are in agreement with some of the SEM-EDS chemical composition results detected in the slag.

Table 7: Chemical composition of HCFeMn slag (XRF)

Sample ID	MnO	FeO	CaO	MgO	SiO_2	Al_2O_3	Total
A	21.7	0.9	31.2	7.3	34.0	3.9	99.0
B	21.3	0.8	31.1	7.4	34.4	3.9	98.9
C	21.4	0.8	31.1	7.4	34.4	3.9	99.0
Average	21.5	0.8	31.1	7.4	34.3	3.9	
Std. dev.	0.21	0.07	0.06	0.06	0.23	0.00	

Table 8: Chemical composition of HCFeMn slag (ICP)

Sample ID	MnO	FeO	CaO	MgO	SiO_2	Al_2O_3	K_2O	TiO_2	BaO	Total
A	23.1	0.9	29.0	6.9	34.2	3.9	0.2	0.2	0.6	98.9
B	23.8	0.8	29.7	7.2	34.7	3.9	0.2	0.2	0.6	101.0
C	23.4	0.8	29.6	7.1	34.6	3.9	0.2	0.2	0.6	100.3
Avg	23.4	0.8	29.4	7.1	34.5	3.9	0.2	0.2	0.6	
Std dev.	0.36	0.05	0.34	0.16	0.25	0.04	0.01	0.00	0.01	

4.1.2 Bulk phase chemical analysis

The HCFeMn slag sample analysed for quantitative XRD comprised a predominant cumulative amount of Olivine (glaucochroite and monticellite). Glaucochroite being a Mn-rich olivine and monticellite, a Mg-rich olivine and trace amounts of quartz and gehlenite in Table 9 with the corresponding diffractogram in Figure 16.The abundance of quartz as trace amounts is not in agreement with the reported chemical analysis of the as-received slag where SiO_2 occurred in larger concentration than all other oxide species. This is also noted in SEM-EDS results where SiO_2 was one of the most dominant oxides.

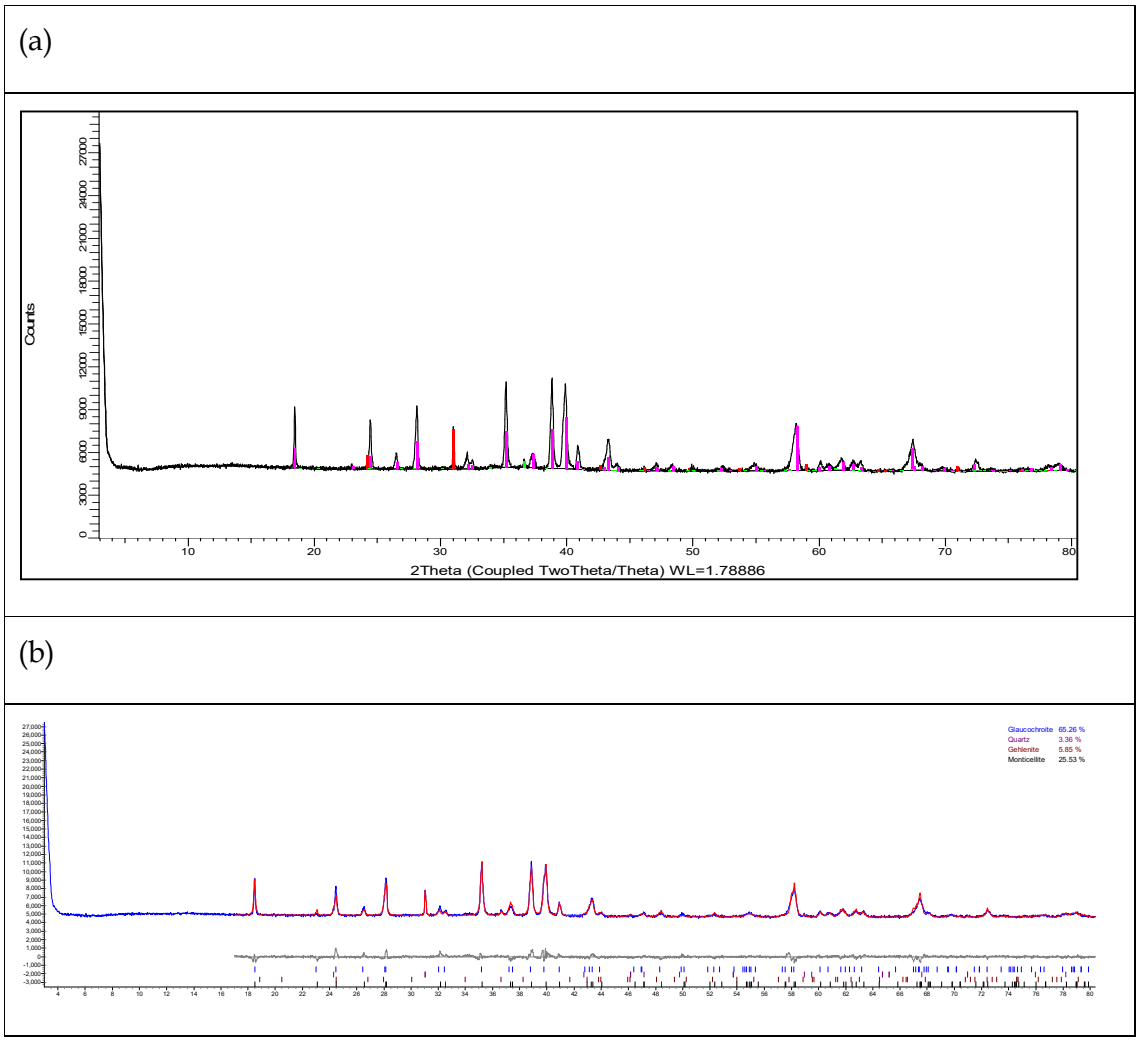

Figure 16: XRD diffractograms of the as-received slag sample showing phase counts. (a) Generated from EVA software (b) Generated from Topaz software

Table 9: Summary table of the mineral abundance found in the HCFeMn slag sample

Legend	Mineral	Ideal composition	Abundance
	Quartz	SiO_2	3.4
	Gehlenite	$Ca_2Al(AlSiO_7)$	5.9
	Glaucochroite	$CaMnSiO_4$	65.3
	Monticellite	$CaMgSiO_4$	25.5
	Total		**100**

4.1.3 Specific phase-chemical analysis

The specific phase-chemical analysis results are presented for the as-received slag. Micrographs of the as- received HCFeMn slag samples are presented in Figure 17

where a general overview of the as-received slag sample is presented as a SEM BSE micrograph with a zoomed in SEM backscattered electron image marked by Area A. Area A indicates the identified slag phases, marked by point '1' and '2' in which both phases are characterised by similar oxide compositions. Point 1 of Area A is the primary slag phase, which contains MgO, Al_2O_3, SiO_2, CaO and MnO as presented in Table 10. The secondary slag phase denoted by point 2, contains the same oxides at similar mass% but with no Al_2O_3. On average, the as-received slag oxide composition for both phases consists of SiO_2 at 32.8%, CaO at 35.4% and MnO at 27.3%.

The primary and secondary slag phases are the result of the main reduction taking place in a two-phase area where liquid primary phase and solid MnO secondary phase co-exist.

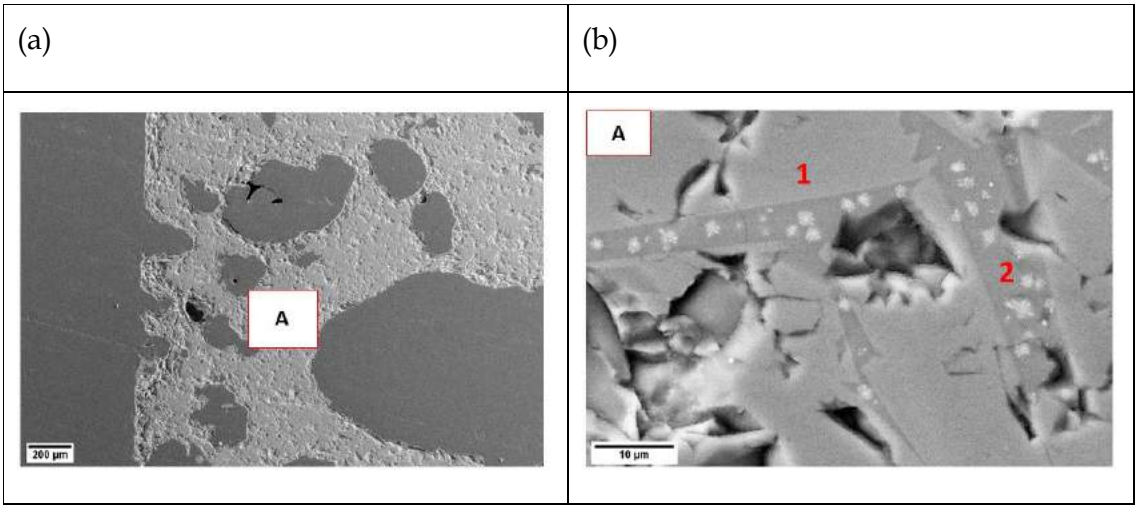

Figure 17: SEM micrographs of the as-received HCFeMn slag sample conducted at 20.0 kV. (a) Secondary electron image. Scale bar indicates 200 µm. (b) Backscattered-electron image of zoomed out area A indicating primary phase as '1' and secondary phase as '2'. Scale bar indicates 10 µm.

Table 10: Normalised HCFeMn slag elemental composition of Area A, point 1 and 2 by SEM-EDS (mass%)

Scan Area		MgO	Al_2O_3	SiO_2	CaO	MnO	Total
1	SEM-EDS	5.9	3.5	36.8	32.5	26.3	105
2	SEM-EDS	4.6	-	28.8	38.2	28.3	100
Average		5.3	3.5	32.8	35.4	27.3	104

In Figure 18, the MnS spheres that exist within the secondary slag phase are reported with corresponding Table 11 of the elemental composition. The MnS spheres predominantly consisted of Mn at greater than 70 mass%. The MnS spheres and the dendrites exist in the crystalline phase and likely precipitated during solidification.

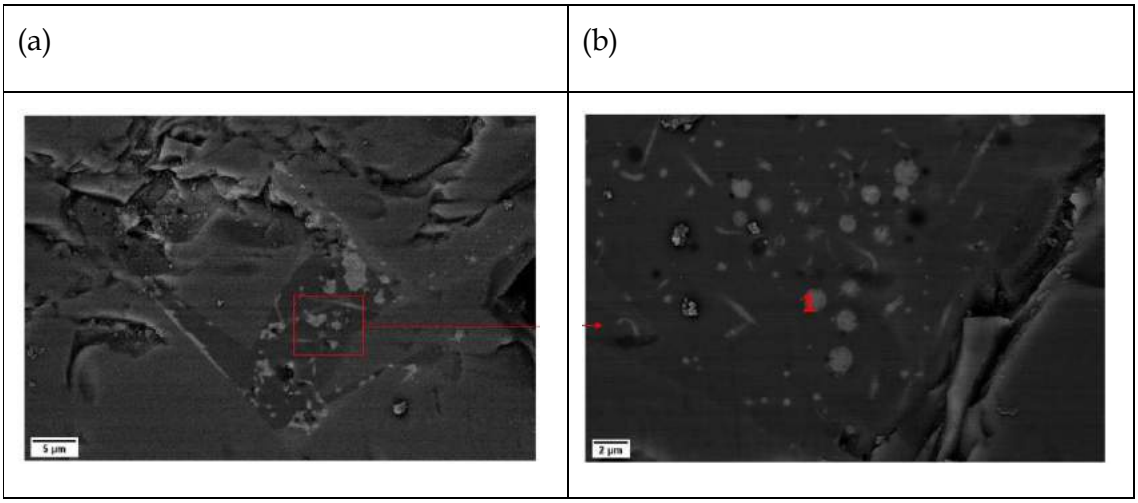

Figure 18: SEM backscattered electron image conducted at 15.0kV. (a) MnS spheres. Scale bar indicates 5 µm (b) MnS sphere zoomed out associated with the secondary slag phase. Scale bar indicates 2 µm.

The MnS spheres compared to the Fe-Mn-C alloy contain predominantly Mn at 79.39 mass% as seen in Table 11. The Fe-Mn-C alloy as presented in Figure 19 found in the as-received slag consisted predominantly of Fe at greater than 80 mass% and less Mn mass% at 3.8% with corresponding elemental composition in Table 12 . Fe in the as-received slag is indicative of the presence of a metallic phase. Teasdale and Hayes (2005) on the influence of metallic Fe in the system found that the addition of Fe-C alloy accelerates the carbon/slag interactions.

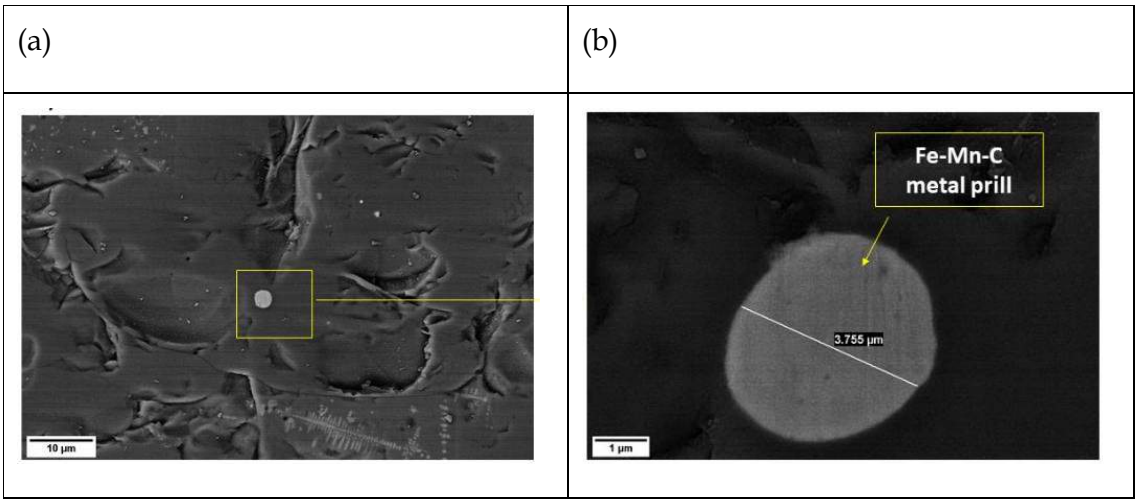

Figure 19: SEM backscattered electron image conducted at 15.0kV. (a) metal prill entrained in the feed slag consisting of Fe metal. Scale bar indicates 10 µm (b) Zoomed out area of metal prill. Scale bar indicates 1 µm.

Table 11: Elemental composition of the MnS phase found in as-received slag (mass%)

Mn	S	Total
79.39	20.61	100

Table 12: Elemental composition of the alloy entrained in the as-received slag (mass%)

Fe	Mn	C	Total
82.7	3.8	13.8	100

4.1.4 Petrographic analysis

Reflectance measurements

The three different types of carbonaceous reductants used for the study reported different measurements of vitrinite reflectance to determine coal rank in Table 13. Coal rank is mostly expressed in terms of vitrinite reflectance as it provides a linear and reliable expression form of rank. Coal 1 reported a vitrinite reflectance (%RoVmr) of 0.8% whilst Coal 2 reported 0.7%. The reflectance measurement results of the parent samples classified Coal 1 and Coal 2 as medium-rank C bituminous coal. The Anthracite sample is classified as high-rank coal with a vitrinite reflectance measurement of 2.9 RoVmr%. The classification follows the international classification of in-seam coals (ECE-UN, 1998).

Table 13: Reflectance measurements summary table for Coal 1, Coal 2 and Anthracite

	Coal 1	Coal 2	Anthracite
Measure Count	201	197	193
Reflectance (Rr)	0.8%	0.7%	2.9%
Standard deviation(s)	0.3	0.1	0.8

The reflectance analysis is accompanied by histograms in Figure 20 that indicated the distribution of readings and is particularly useful in the assessment of coals indicating possible contamination and blending of the coals, which is a useful tool in technological properties of coals (Suarez-Ruiz and Ward, 2008). The histogram distribution of Coal 1 showed a possibility of contamination which was indicated by the standard deviation of 0.3% in Table 13, well above the recommended 0.10% as well as a wider range of the V-steps which are presented in **APPENDIX C**. Vitrinite V-classes correspond to 0.5% reflectance value categories. The varying V-steps or reflectance intervals for Coal 1 consisted of distribution ranging from 0.5%-1, 5% with lower limit of RoV beyond 0.5% and into low rank coal categorisation. On the other hand, Coal 2's histogram distribution showed some possible blending, denoted by standard deviation of 0.10% which is within range and the distribution of the V-steps ranging from 0.5%-1.0% falling within the limit of 0.5% RoV_{mr} between low and medium rank.

(a)	(b)	(c)
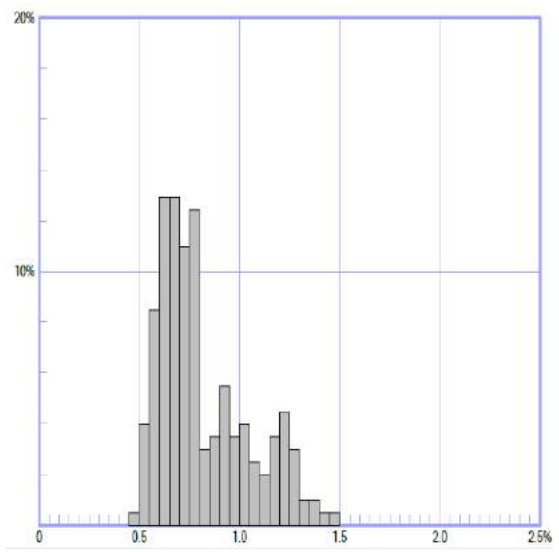	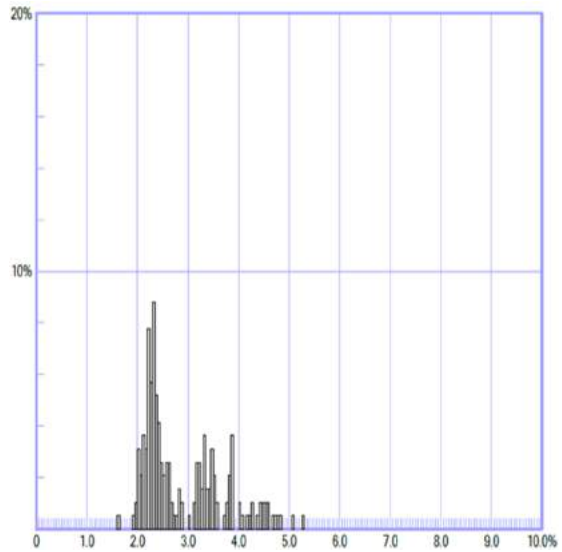	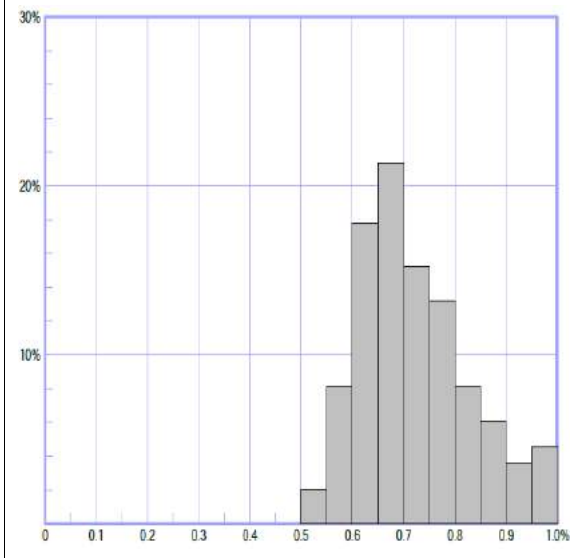

Figure 20: Reflectance histograms for a) Coal 1, b) Anthracite, bi-modal distribution and, c) Coal 2, single bell curve

Maceral Analysis

The maceral analysis results of the studied parent coals are presented in Table 14 expressed as vol %. Summarised in the table are the maceral groups with mineral matter (incl. mm) and on a mineral matter free basis (mmf). The maceral data in Table 14 indicates that Coal 1 and Coal 2 are vitrinite-rich: 44.3 vol% on a mineral matter free basis and 40.5 vol% including mineral matter in Coal 1, and 59.3 vol% on a mineral matter free basis and 54.7 vol% including mineral matter in Coal 2. The Anthracite sample had the least vitrinite proportion of 21.3 vol% including mineral matter and 22.8 vol% on a mineral matter-free basis and is inertinite-rich. Liptinite content was very low from 0.4 to 4.7 vol% on both mineral matter-free basis and including mineral matter. Mineral matter content as determined in Table 14 is low, ranging between 6.5 vol % to 8.6 vol% with Coal 1 consisting of the highest proportion of mineral matter.

Table 14: Summary table of maceral group analyses (Incl. mm- including mineral matter, mmf-mineral matter free basis)

Maceral Group	Coal 1		Coal 2		Anthracite	
	Incl. mm vol%	mmf vol%	Incl. mm vol%	mmf vol%	Incl. mm vol%	mmf vol%
Vitrinite	40.5	44.3	54.7	59.3	21.3	22.8
Inertinite	46.4	50.7	34.6	37.6	71.8	76.8
Liptinite	4.3	4.7	2.9	3.1	0.4	0.4
Mineral matter	8.6	-	7.8	-	6.5	-
Total inertinite	46.6	50.5	34.6	37.6	71.8	76.8
Total reactive macerals	51.0	55.2	59.5	64.5	23.3	24.9

Table 15 summarises the most dominating macerals for each maceral group. In Coal 1, the vitrinite maceral group was mostly dominated by collotelinite at 22.1 vol % and collodetrinite at 17.6 vol % including mineral matter and 24.2 vol % and 19.3 vol% respectively on a mineral matter free basis. The results also showed that Coal 2 had

the highest proportion of the vitrinite maceral group with collotelinite dominating at 31.0 vol% including mineral matter and 33.6 vol% on a mineral matter free basis. The inertinite maceral group consisted mainly of inert semifusinite at 76.3 vol%. The inertinite maceral group was dominated by fusinite, reactive, inert semifusinite and inertodetrinite. Inert semifusinite was found to be the most dominant maceral for Coal 1, Coal 2 and Anthracite. Anthracite had the highest proportion of inert semifusinite at 54.8 vol% including mineral matter and 58.6 vol% on a mineral matter free basis. Liptinite maceral group was mostly found as sporinite with the highest proportion noted in Coal 1.

The total reactive macerals are a combination of the reactive components of inertinite, reactive semifusinite and reactive inertodetrinite, vitrinite and liptinite maceral groups. Coal 1 comprised 50.5 vol % of total reactive macerals including mineral matter and 55.2 vol% on a mineral matter free basis as presented in Table 15. Coal 2 consisted of the highest total of reactive macerals at 59.5 vol% including mineral matter and 64.5% on a mineral matter free basis with the highest proportion of the total reactive macerals. Anthracite comprised the lowest proportion of total reactive macerals at 23.3 vol % including mineral matter and 24.9 vol% on a mineral matter free basis.

The total reactive macerals in Anthracite consisted mainly of vitrinite and reactive semifusinite. Fusinite, inert semifusinite and inert inertodetrinite are the principal inertinite components in the inertinite group for Coal 1, Coal 2 and Anthracite.

The reactive and non-reactive maceral components in petrography are indicative of their change in form and structure when subjected to heat. The effect of each maceral with coal rank on reductant reactivity will be further discussed.

Table 15: Summary table of the dominant macerals in Coal 1, Coal 2 and Anthracite (inc. mm- including mineral matter, mmf-mineral matter free basis)

Maceral Group (vol %)	**Coal 1**		**Coal 2**		**Anthracite**	
	mmf	*Inc. mm*	*mmf*	*Inc. mm*	*mmf*	*Inc. mm*
Vitrinite	44.3	40.5	59.3	54.7	22.8	21.3
Collotelinite	24.1	22.0	33.6	31.0	13.9	13.0
Collodetrinite	19.2	17.5	23.9	22.0	8.4	7.9
Corpogelinite	0.4	0.4	1.4	1.3	0.2	0.2
Telinite	0.4	0.4	0.2	0.2	0.0	0.0
Pseudovitrinite	0.2	0.2	0.2	0.2	0.2	0.2
Liptinite	4.7	4.3	3.1	2.9	0.4	0.4
Sporinite	4.3	3.9	2.7	2.5	0.4	0.4
Cutinite	0.4	0.4	0.4	0.4	0.0	0.0
Inertinite	51.0	46.6	37.6	34.6	76.8	71.8
Fusinite	14.5	13.3	8.3	7.6	3.4	3.2
Reactive semifusinite	6.0	5.5	1.9	1.7	1.5	1.4
Inert semifusinite	21.7	19.9	20.3	18.7	58.6	54.8
Inert inertodetrinite	7.9	7.2	6.6	6.1	9.1	8.5
Reactive inertodetrinite	0.2	0.2	0.2	0.2	0.2	0.2
Secretinite	0.6	0.6	0.2	0.2	4.0	3.7
Mineral matter		8.6		7.8		6.5
Rank (mean random reflectance %)	0.8		0.7		2.9	
Rank category	**Med rank C bituminous**		**Med rank C bituminous**		**Anthracite**	
Total reactive* macerals	55.2	50.5	64.5	59.5	24.9	23.3
Total inert macerals	51.0	46.6	37.6	34.6	76.8	71.8

*Total reactive macerals= vitrinite +liptinite+ reactive semifusinite and reactive inertodetrinite

A relationship between the inertinite maceral group and coal rank for the three reductants, on a mineral matter free basis and with mineral matter, is presented in Figure 21.The graph shows that Anthracite, a higher ranked coal consisted of the highest inertinite proportion. In Figure 22, the vitrinite group variation with coal rank, on a mineral matter free basis and with mineral matter is presented. Coal 1 and Coal 2 with similar reflectance measurements (0.8% and 0.7 % respectively) consisted of the highest vitrinite proportion. Whilst Anthracite, a higher ranked coal consisted of the least vitrinite proportion and highest inertinite. This does not suggest that a higher ranked coal constitutes to a lower proportion of vitrinite macerals or a higher proportion of inertinite macerals. But rather an observation of the studied reductants and their relative macerals composition in relation to coal rank.

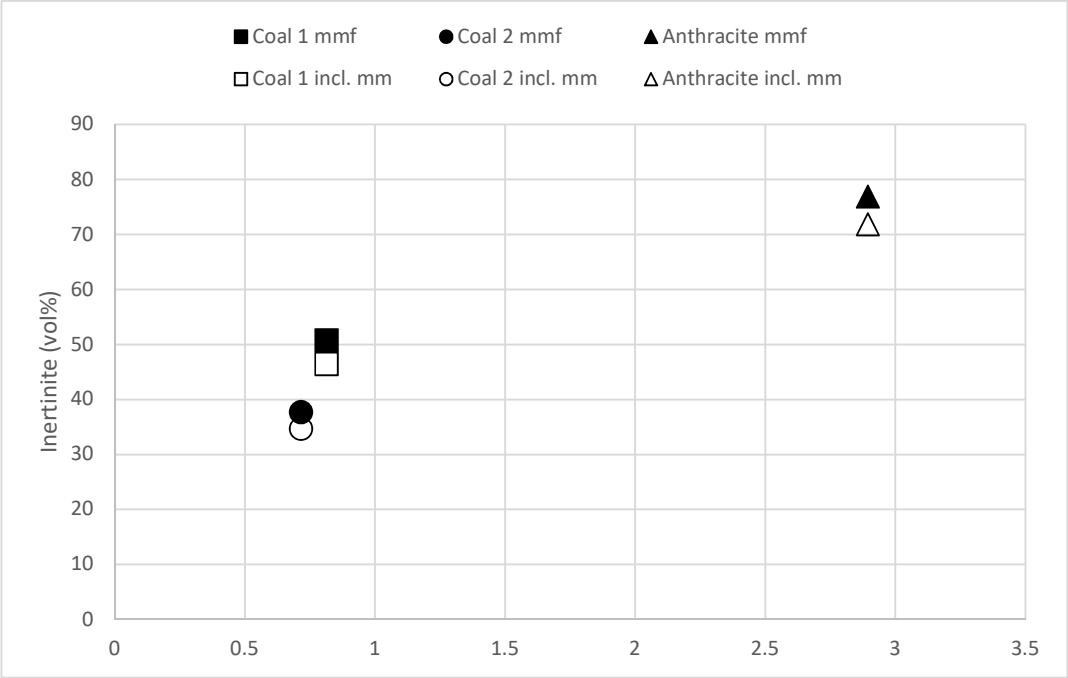

Figure 21: Inertinite proportion without mineral matter (mmf) and including mineral matter vs rank relationship

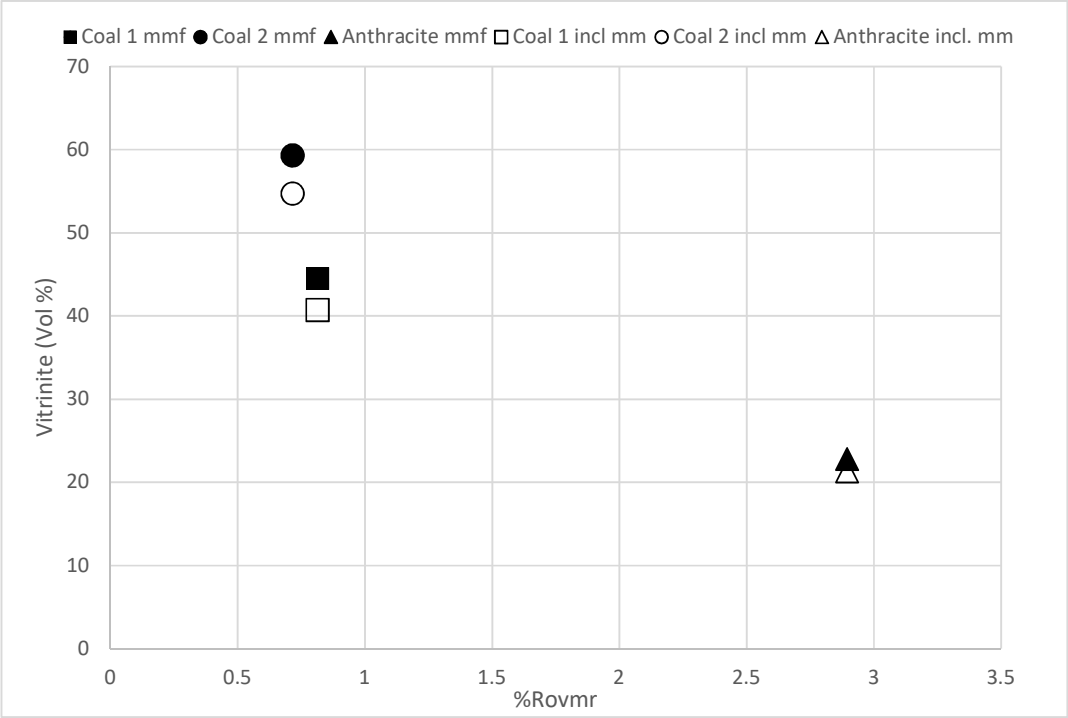

Figure 22: Vitrinite group without mineral matter (mmf) and including mineral matter (incl. mm) vs rank

The series of micrographs identifies the most dominant macerals found microscopically in Coal 1, Coal 2 and Anthracite. Anthracite appears lighter in reflectance in comparison to Coal 1 and Coal 2 and this is attributed to the rank of the coal where higher ranked coals appear light under reflected light microscope.

Coal 1

Scale bar= 100 µm

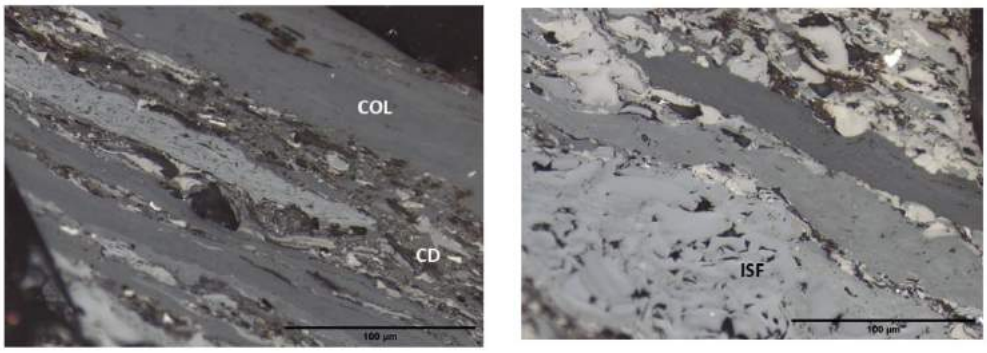

A **B**

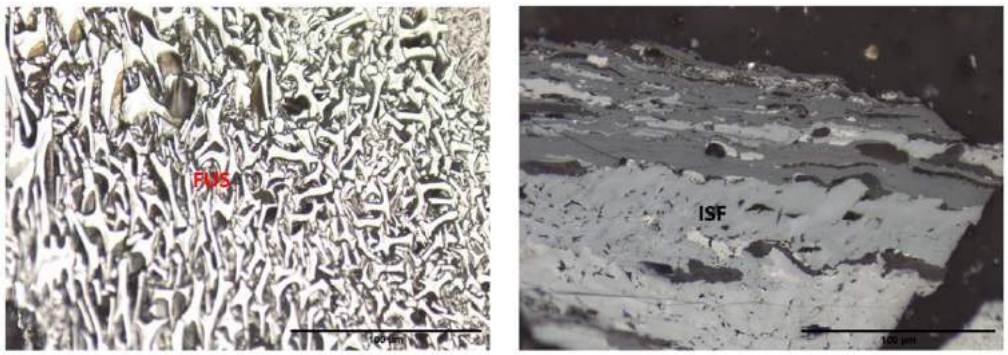

C D

Figure 23*:* Plates A-D for parent Coal 1

A- Banded vitrinite and inert semifusinite, vitrinite bands (collotelinite) and collodetrinite with a vitrinitic groundmass and inertinite fragments.

B- A smoother band of collotelinite surrounded by inert semifusinite and vitrinitic matrix with inertinite fragments.

C- Fusinite showing Bogen structures.

D- Inert semifusinite at the bottom transitioning into vitrinite bands.

Coal 2

Scale bar= 100 µm

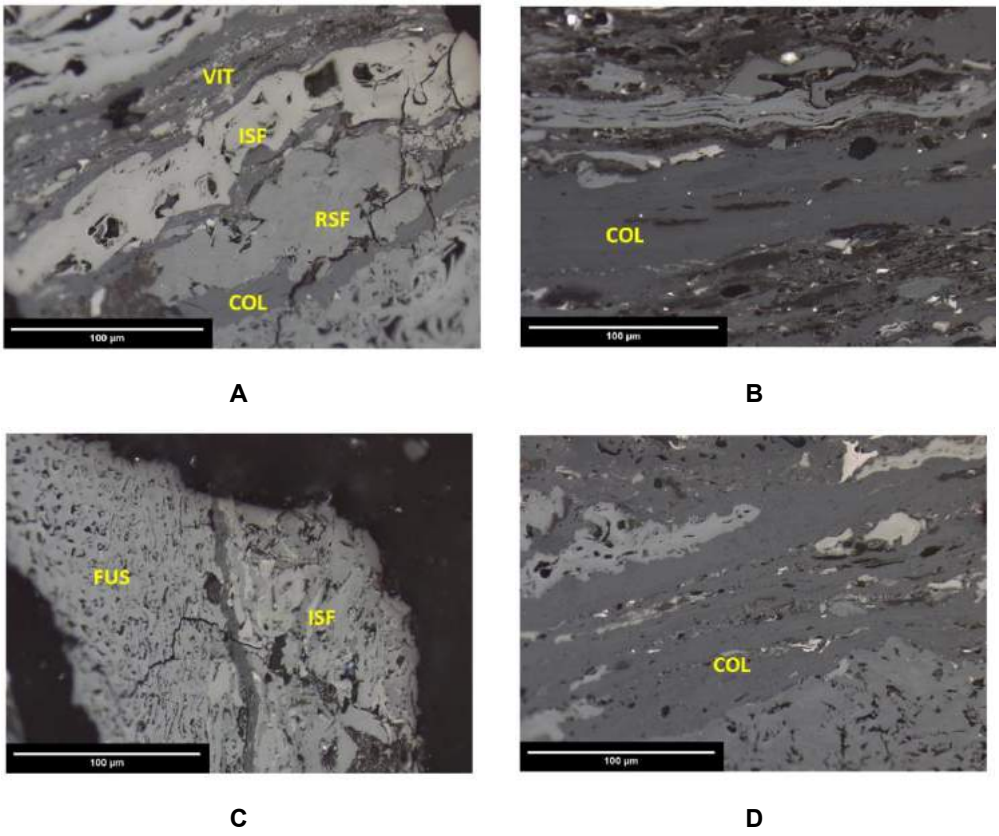

Figure 24: Plates A-D for parent Coal 2

A- Bands of vitrinite macerals with inertinite, vitrinitic matrix transitioning into reactive and inert semifusinite and bottom band of collotelinite.

B- Collotelinite existing with a vitrinitic matrix and semifusinite.

C- Large fusinite with semifusinite, a crack runs through the identified particles.

D- Vitrinite maceral existing with semifusinite.

Anthracite

Scale bar= 100 µm

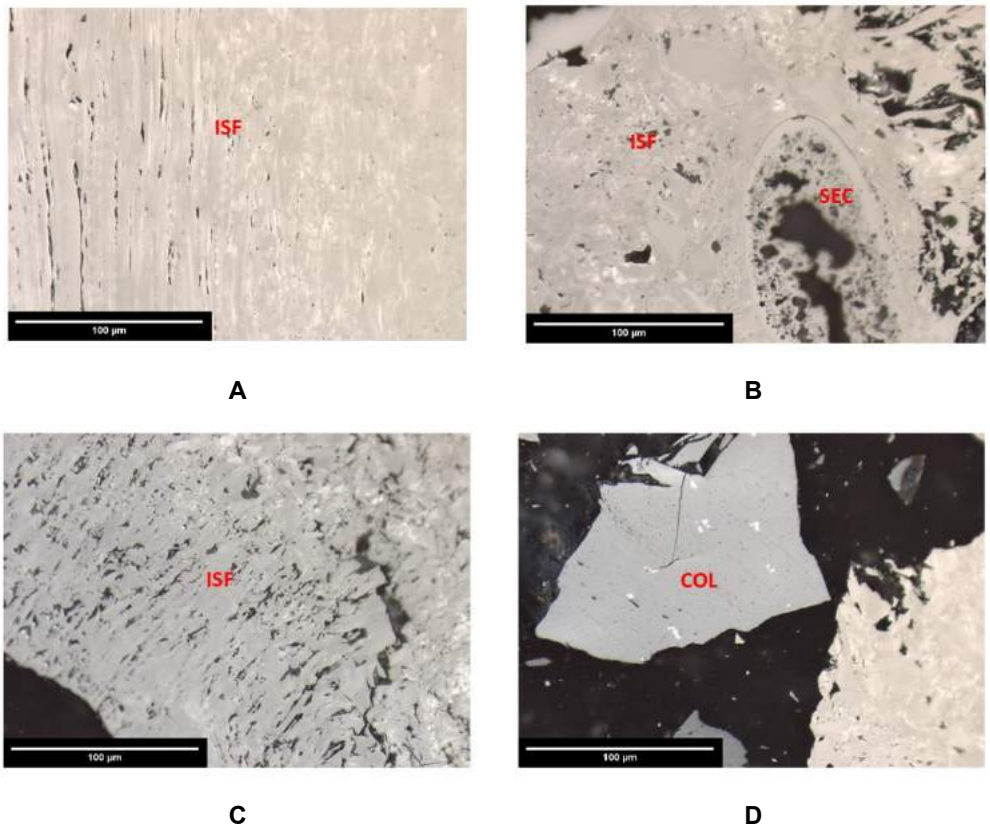

Figure 25: Plates A-D for Anthracite parent coal

A- Banded semifusinite at different orientations

B- Secretinite embedded within semifusinite showing internal structure

C- Secrenite (inertinite) embedded with semifusinite

D- Banded vitrinite with semifusinite

Microlithotype analysis

The results of the arrangement of the macerals show that the macerals occurred mostly as monomacerals as seen in Table 16 . Coal 1 with a total of 61.7 vol %, Coal 2 64.5 vol % and Anthracite with the highest proportion of monomaceral arrangement of 88.6 vol%. Of the monomaceral arrangement group, the macerals occurred as vitrite which belongs to the vitrinite maceral group, most dominant in Coal 2 at 44.8 vol% followed by Coal 1 at 27.7 vol % and Anthracite, the least at 17.5 vol%. The second most

dominant monomaceral is semifusite where Anthracite consisted of the highest proportion at 59.1 vol % compared to Coal 1 and Coal 2 at 22.2 vol% and 12.9 % respectively.

The bi-maceral group was mostly dominated by vitrinertite which is an arrangement of vitrinite and inertinite in the form of fusite and semifusite. Coal 1 had a total of 21.7 vol % of the bi-maceral arrangement, Coal 2 had a total of 16.1 vol % and Anthracite the least total of 4.4 vol % Coal 1 with the highest proportion at 9.8 vol % and Anthracite the least proportion of 2.8 vol %.

Table 16: Microlithotype analyses for Coal 1, Coal 2 and Anthracite

Group	MICROLITHOTYPE (Vol %)	Coal 1	Coal 2	Anthracite
MONOMACERAL	Vitrite	27.7	44.8	17.5
	Semifusite	22.2	12.9	59.1
	fusite / Secretinite	7.1	3.2	4.7
	Inertodetrite	2.2	1	1.6
	Inertite sf+int	2.5	2.6	5.7
	Liptite	0	0	0
	TOTAL	**61.7**	**64.5**	**88.6**
BIMACERAL	Vitrinertite vit+sf/f	9.8	7.7	2.8
	Vitrinertite vit+int	6.1	3	1.4
	Clarite vit+lipt	2.9	3	0.2
	Durite int+lipt	2.9	2.4	0
	TOTAL	**21.7**	**16.1**	**4.4**
TRIMACERAL	Duroclarite (V>I, L)	8.2	6.1	0.2
	Clarodurite (I>V, L)	0.4	0.2	0.2
	Vitrinertoliptite (L>I, V)	0	0.2	0
	TOTAL	8.6	6.5	0.4
CARBOMINERITE	cbm argillite	1.8	1.6	2
	cbm silicate (quartz)	2.2	1	0.8
	cbm pyrite	1	2.4	1
	cbm ank/carb	1.4	1.6	0.4
	cbm poly	0	0.2	0
	TOTAL	**6.4**	**6.8**	**4.2**
ROCK	rock	1.6	6.1	2.4
TOTAL		91.4	93.5	99.6

The arrangement of macerals plays an important role in technological applications. For instance, a vitrite occurring as a monomaceral is not constrained and swells and expands freely during heating. In Coal 2, it was observed that the vitrite occurring as a monomaceral consisted of the highest proportion meaning that there were no constraints and therefore, Coal 2 was able to swell and expand significantly. This consequently led to volatile matter released at a higher rate leading to more mass loss. The bi-maceral proportions of the microlithotype show that Coal 1 consisted of a higher proportion of vitrinertite which is present as either a combination of vitrite and semifusite or as vitrite and inertite. This could mean that the maceral associations of Coal 1 are constrained between two layers of inertite (belonging to the inertinite group) reducing swelling. The microlithotype analysis cannot provide information on which maceral configuration collectively contributes to the reductant reactivity towards slag. However, information of the behaviour of maceral arrangement and their effect when heated was established.

4.2 Reactivity test results

The following set of results comprise the reductant reactivity to slag test results, including generated mass loss curves. The curves for Coal 1 and Coal 2 are similar with some variations which suggests that the carbonaceous reductants behaved similarly. For instance, a rapid initial loss was observed at a higher rate for Coal 2 than Coal 1. At 72 minutes reaction time, Coal 2 had an initial total mass loss of 38.6 %, Coal 1 at 32.9 % and Anthracite the least mass loss at 12.1% as seen in Figure 26. The initial rapid mass loss can be largely attributed to the release of volatile matter where it is expected to be driven off at temperatures above 400°C. Thereafter, Coal 1 recorded a higher total mass loss of 37.0% and 39.7% respectively at 144 and 216 minutes reaction time. Anthracite still obtained the least total mass loss % of 16.4 % and 27.2% respectively. At 288 and 360 minutes reaction time, Coal 2 obtained a higher mass loss compared to Coal 1. An almost linear mass loss pattern was observed for Anthracite from 72- 216 minutes reaction time.

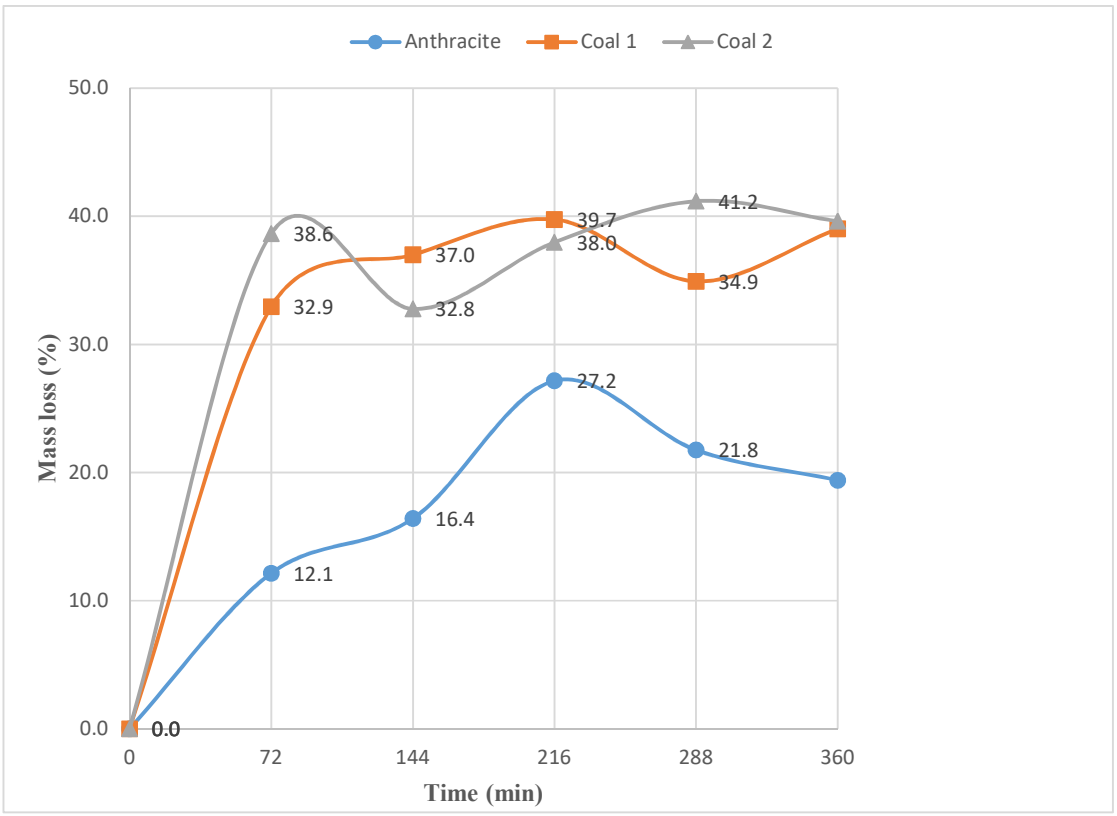

Figure 26: Mass loss % table with corresponding curves for Coal 1, Coal 2 and Anthracite at the different reaction time

Table 17: Mass loss % Coal 1, Coal 2 and Anthracite at the different reaction time

Time(min)	Total Mass loss %			Mass loss from reduction		
	Anthracite	Coal 1	Coal 2	Anthracite	Coal 1	Coal 2
0	0	0	0	0	0	0
72	12.1	32.9	38.6	6.8	5.2	9.3
144	16.4	37.0	32.8	11.1	9.3	3.5
216	27.2	39.7	38.0	21.9	12	8.7
288	21.8	34.9	41.2	16.5	7.2	11.9
360	19.4	39.0	39.6	14.1	11.3	10.3

The non-linear mass loss trend with increasing reaction times could potentially be due to a number of reasons, such as that the tests were not conducted on a continuous series basis but rather in batch mode. This method sets it apart from data obtained

through thermogravimetry type analysis, where continuous thermal behaviour of material as mass loss is observed as a function of time and temperature. The mass loss profiles in Figure 27 highlight the influence of the slag and reductant crucible sizes on the mass loss. For instance, in Coal 2 less mass loss was observed at 144 and 216 minutes reaction time because less reductant crucible mass was used compared to the preceding 72 minutes reaction time. Contrastingly, Anthracite obtained less mass loss at 288 and 360 minutes reaction time compared to 216 minutes reaction time due to less slag mass used. Other factors such as the method of manually selecting the reductants for the reductant 'crucible' could also have played a role in creating uncertainty through an unrepresentative sample.

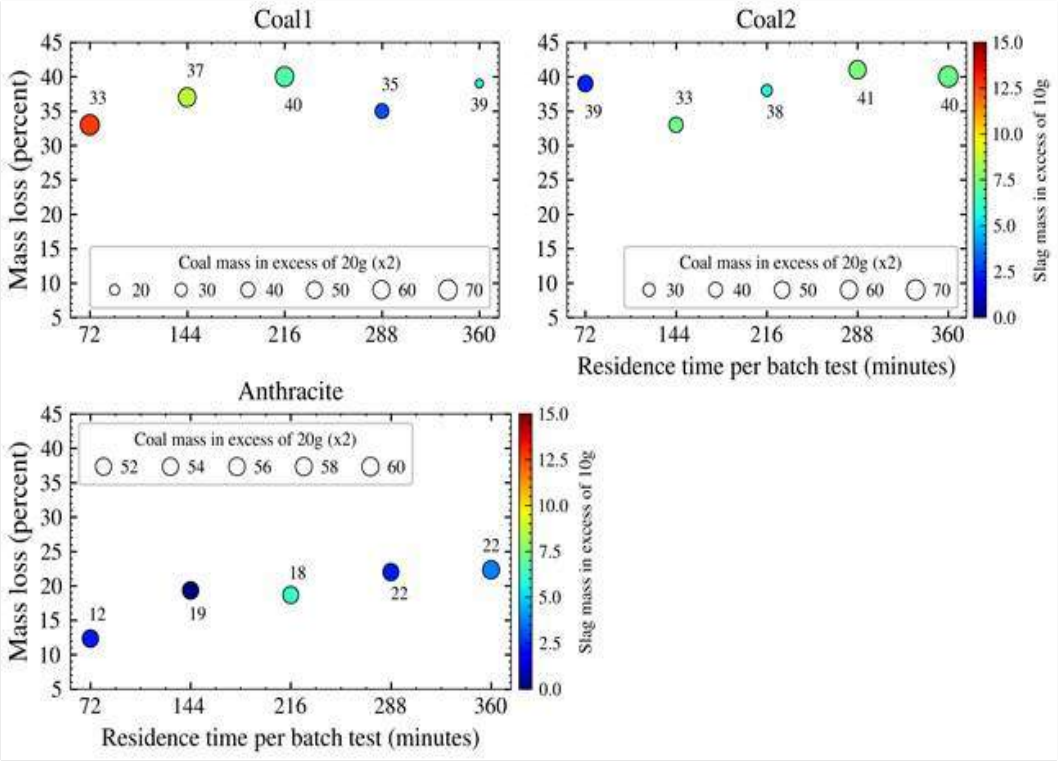

Figure 27: Mass loss profiles for Coal 1, Coal 2 and Anthracite highlighting slag and crucible mass

However, despite the stated reasons, the results demonstrated that overall Coal 2 had the highest mass loss% followed by Coal 1 and, Anthracite with the least mass loss %. The mass loss observed for all the reductants can be attributed to release of volatile matter as well as reduction of MnO to metallic Mn at higher temperatures. At higher

temperatures reduction of MnO in the slag to Mn in the alloy is expected to occur between temperatures of 1400°C and 1500°C (Ringdalen et al., 2015).

4.3 Characterization of post mortem samples

4.3.1 Macroscopic observations

Selected images of the macroscopic observations of the heat-treated slag and reductant samples are presented in Figure 28 with accompanied summary of the observations in Table 18.

The following observations were noted:

- Coal 1 and Coal 2 had similar observations with little variations compared to Anthracite that reacted completely different.
- In overall, applicable to all the reaction times, Coal 1 exhibited more heat-induced cracks and was found to be more porous and, brittle upon touch. As a result, most of the slag penetrated through the cracks and settled to the base of the reductant 'crucible' or deposited within the cracks. Consequently, it was almost impossible to separate from the alumina crucible that was serving as a containment vessel. Coal 2 also had visible cracks but to a lesser degree than Coal 1.
- In comparison, Anthracite had almost no visible cracks and was less brittle. There was also no visible penetration of the slag through the Anthracite.
- Coal 1 and Coal 2 seemed to contain less slag from 144 minutes reaction time to 360 minutes reaction time. This could be as a result of both a release of volatile matter and reduction reactions.
- The slag is characterised by a green appearance in colour which is an indication of MnO presence. In terms of colour changes of the slag, Coal 1 and Coal 2 at 72 minutes reaction time already had no green slag appearance which is an indication that there was little or no MnO present. The MnO could either have reacted with the carbon and report as Mn in the alloy or could have been lost as part of the volatiles.

- In terms of colour changes, in Anthracite the change in slag colour from green to grey took place at a slower rate compared to Coal 1 and Coal 2. This is in support of the reductant reactivity tests where Anthracite seemingly was the least reactive. Meaning there was less mass loss due to reduction or devolatilization.

The volume and shape changes in Anthracite after heat treatment, were also less visible compared to Coal 1 and Coal 2.

Reaction time (min)			
72	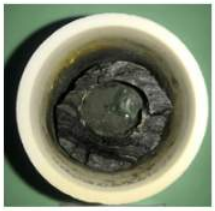	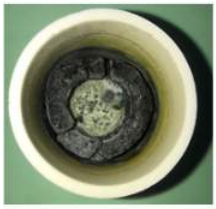	
	Coal 1	Coal 2	Anthracite
144			
	Coal 1	Coal 2	Anthracite

216	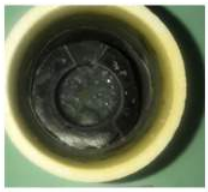		
	Coal 1	**Coal 2**	**Anthracite**
288	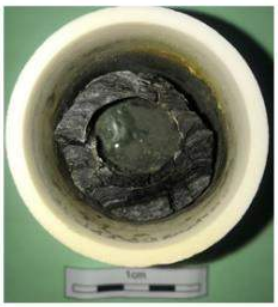		
	Coal 1	**Coal 2**	**Anthracite**
360			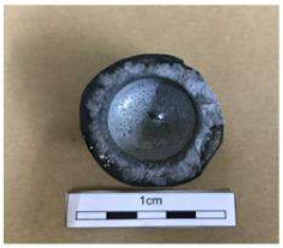
	Coal 1	**Coal 2**	**Anthracite**

Figure 28*:* Images of the heat -treated samples at the different reaction times at 1500°C

Table 18: Summary of the observations of the photographic images of heat-treated samples

Observations			
Reaction time (min)	**Coal 1**	**Coal 2**	**Anthracite**
72	Heat induced-cracks visible Slag colour changed from initial green, a sign of reduction occurring Brittle upon touch	Heat-induced cracks Slag colour change to grey initiated at early reaction time Brittle upon touch	No visible cracks Slag appearance green
144	Coal deformed Grey slag Alloy visible	Flaky coal pieces Grey slag colour	No changes, cracks not visible and slag colour still green
216	No slag present Visible alloy	No slag present Visible alloy	Slag appearance still green
288	All slag reacted, little to no slag noted	All slag reacted	Slag appearance change to grey
360	All slag reacted	All slag reacted	Alloy visible Slag colour grey

In Figure 29, cross sections of the heat-treated samples are presented. At 72 minutes reaction time, the cross section for Coal 1 presented visible layering of the coal with alloy observed at the slag-coal interface. Slag also penetrated through the heat induced fissures, to the bottom of the reductant crucible. Coal 2, at 72 minutes reaction time, presented no visible layering and slag was observed at the interface. On the other hand, Anthracite at the same reaction time of 72 minutes, had slag present at the reaction interface and no alloy was noted.

At 144 minutes reaction time, Coal 1 contained larger metal prills and the slag was observed at the interface with no visible leakage to the bottom. Coal 2 had visible cracks with slag depositing in-between the heat induced cracks, whilst Anthracite had fewer cracks but slag was mostly observed at the interface.

At 216 minutes reaction time, Coal 1 noted visible cracks with no slag observed at the interface. Coal 2 had no cracks and metal prills and slag were observed at the interface. No changes were noted for Anthracite but a clearly defined slag-carbon boundary with alloy formed in between.

Coal 1, at 288 minutes reaction time, had no slag at the interface and was deformed at the reductant crucible edges with slag observed throughout the coal matrix, particularly finding preference within the cracks. In Coal 2, at the same reaction time, slag was observed at the interface with visible alloy. There was not much change observed for the Anthracite.

At 360 minutes reaction time, no slag was visible at the interface of Coal 1, with visible cracks at the edges of the coal. In Coal 2, slag was observed at the corner of the interface with the coal. Anthracite had slag remaining at the interface with visible larger metal prills. Most of the alloy was mainly observed at the slag/carbon interface and on the periphery where slag and carbon made contact.

Reaction time (min)	
72	   Coal 1 Coal 2 Anthracite
144	   Coal 1 Coal 2 Anthracite
216	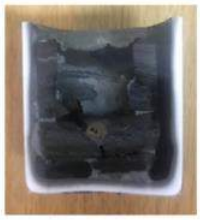 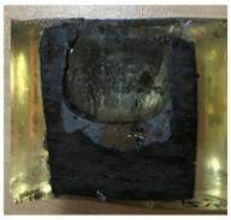  Coal 1 Coal 2 Anthracite
288	 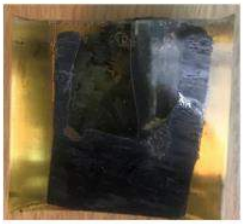  Coal 1 Coal 2 Anthracite

360	

Figure 29:Cross-section images of the heat-treated samples for the different reductants at different reaction times

4.3.2 Specific phase- chemical analysis

The following section includes selected micrographs of the heat-treated reductant types, with slag at the specified reaction times at a temperature of 1500°C.The relevance of the SEM-EDS results is to provide perspective in terms of the extent of carbothermic reduction. To track the reducible and most important chemical composition of MnO in the slag, Mn in the alloy will allow sound argument relative to occurrence of carbothermic reduction from the reductant reactivity tests. Other oxide compositions such as CaO, Al_2O_3, MgO and SiO_2 will be highlighted for the sole purpose of comparing with the as-received slag, as they are expected to be stable and irreducible as they do not form part of the reduction reaction.

Moreover, the SEM-EDS results will also provide the differences noted from the slag in terms of its microstructure in comparison to the as-received slag and how it evolves at the different reaction times for each reductant type. Good contact between the slag and reductant type needs to be maintained in order to produce alloy. Therefore, this section will also observe the differences between the contact area of slag and reductant and its impact on the yield of Mn in its metallic phase.

The following observations were made for the three reductants at the different reaction times:

72 minutes reaction time

For Coal 1, the alloy existing in the slag matrix in Figure 30 predominantly consisted of two phases of Si-Mn content with higher concentration of Mn at above 70 mass %

for both phases and Si at approximately 20 mass % with no Fe present as seen in Table 19. The greater than 20 mass % reported for Si is most likely due to instrument inaccuracies Three different slag phases were identified, a primary slag matrix high in CaO and SiO_2, a secondary slag phase with no MgO and high in CaO and SiO_2. A dendritic feature was also associated with the slag on the edge of interface between alloy and slag phase. A needle like crystalline phase was also present consisting of high MnS. Both the dendrite feature and MnS phase form part of the crystalline phase that formed likely as a result of solidification.

The slag microstructure in comparison to the as-received differs in that it consisted of a needle like crystalline phase in a random network of veins which was not present in the as-received slag. There was a clear boundary between the coal and the slag, the slag is associated with finely disseminated metal prills, which did not get enough time to coalesce to form bigger particles.

Coal 2 at 72 minutes reaction time had the interface between the coal clearly defined with alloy forming in between as seen in Figure 31.The coal was porous and with metal entrainment between the pores. The alloy was identified as a single-phase alloy with a content of Mn greater than 70 mass% as seen in Table 20 and is associated with a SiC phase that was not present in Coal 1 at the same reduction time. The slag microstructure did not contain any dendrites in comparison to the as-received slag and Coal 1 at the same reduction time but consisted of the primary liquid slag phase that contained MnO and secondary slag phase rich in CaO-SiO_2.

Figure 32 displays a micrograph of the slag- anthracite interface with clearly defined boundaries between slag and anthracite and alloy finding preference between the reaction interface. The alloy consisted of two phases, which are similar in composition, predominantly made up of Si-Mn-Fe displayed in Table 21. Area A in Figure 32 can be distinguished by three different slag phases, a primary slag phase that is rich in, CaO-SiO_2, a secondary slag phase with needle like structure consisting of MgO and CaO-SiO_2 and a dendritic feature made up mainly of MnS. The slag microstructure of Anthracite was found to be similar to the as-received slag as well as Coal 1 at same reaction time.

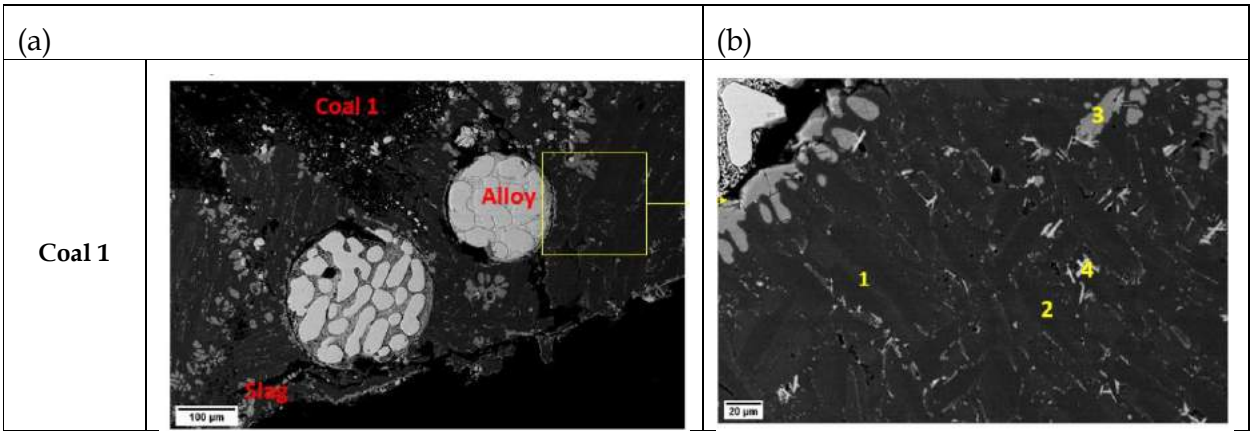

Figure 30: SEM backscattered electron image of Coal 1 at 72 minutes reaction time conducted at 20.0 kV (a) Slag, Coal 1 and alloy phases. Scale bar indicates 100 µm. b) Identified slag phases with associated features. Scale bar indicates 20 µm.

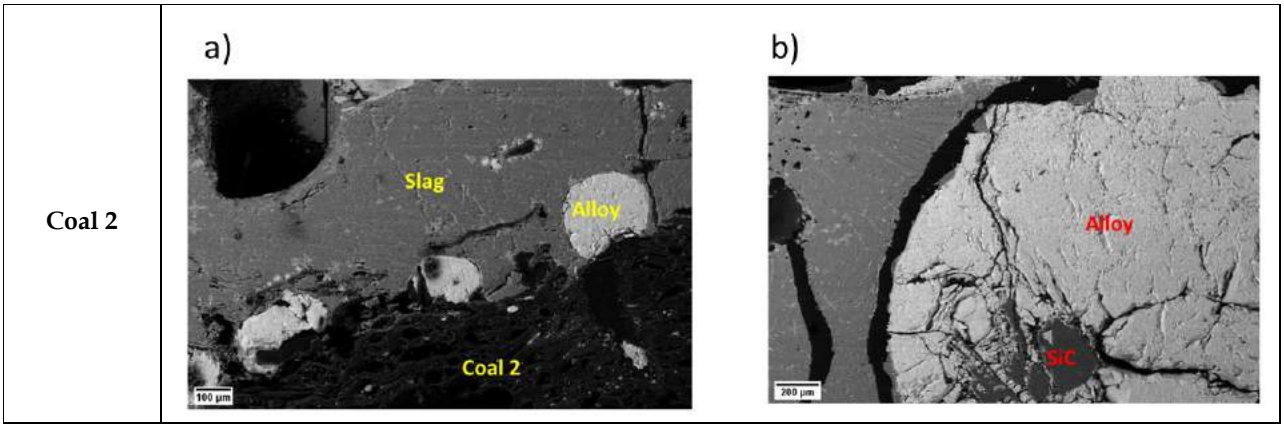

Figure 31: SEM backscattered electron image at 72 minutes reaction time conducted at 20.0 kV (a) Slag, Coal 2 and alloy interface. Scale bar indicates 100 µm. (b) Alloy phase associated with SiC. Scale bar indicates 200 µm.

Anthracite	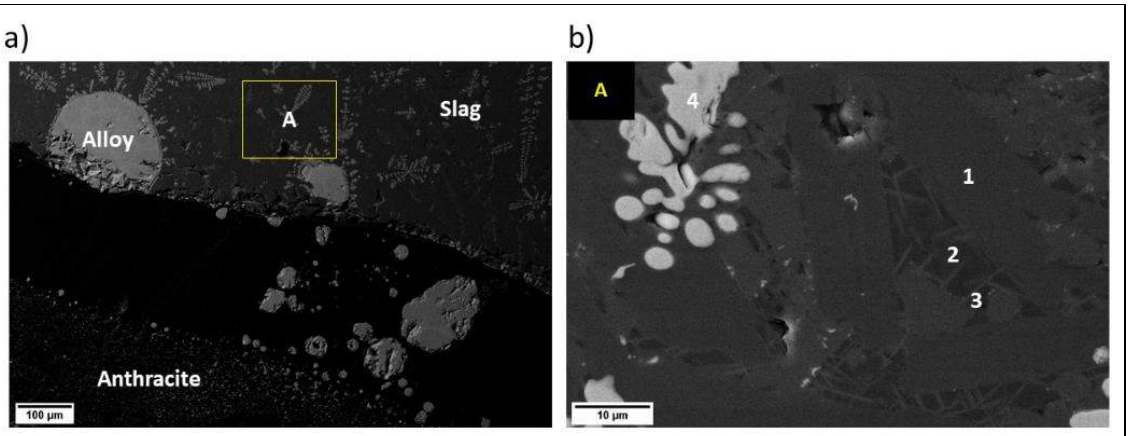

Figure 32: SEM backscattered electron image of anthracite-slag at 72 minutes reaction time conducted at 20.0 kV. (a) Interface of the anthracite and slag with alloy phase. Scale bar indicates 100 µm. (b)Identified slag phases in Area A. Scale bar indicates 10 µm.

Table 19*:* Elemental composition of the alloy phases at 72 minutes reaction time Coal 1 (mass%)

Area		**Si**	**Mn**	**Total**
A	1	21.4	78.6	100
	2	24.1	75.9	100

Table 20: Elemental composition of alloy phase and SiC at 72 minutes reaction time for Coal 2 (mass%)

Area		**Mn**	**Si**	**C**	**Total**
	Alloy	79.1	20.9	-	100
	SiC	-	35.6	64.4	100

Table 21: Elemental composition of the alloy phase at 72 minutes reaction time Anthracite (mass%)

Area	**Si**	**Mn**	**Fe**	**Total**
Alloy	28.3	60.7	11.0	100

144 minutes reaction time

In Figure 33, Coal 2 slag microstructure at 144 minutes reaction time was found to vary from 72 minutes reaction time. The different slag phases are identified consisting of a primary slag matrix and crystalline phase. The slag is also associated with the

alloy, which could be a result of the liquid slag penetrating into the liquid alloy with SiC distributed within the slag and alloy phase. The alloy is also characterised by a single phase mainly of Si-Mn at a higher proportion of Mn greater than 70% as seen in Table 22.

The slag- anthracite boundary is still clearly defined with alloy existing mainly in between with migrated prills into the slag. The slag microstructure does not differ from 72 minutes reaction time for both the primary and secondary slag phase with dendrites observed. The primary slag phase was found to be high in CaO-MgO whilst the secondary phase contained random needle like structure with high CaO content. The alloy consisted of two phases, the primary alloy phase consisted as presented in Figure 34 by point 4 of Si-Mn-Fe with the Mn found at higher concentrations than Si and Fe as seen in Table 23. The Anthracite did not exhibit any pores however consisted of fine metal prills dispersed throughout.

Reaction time	**144 minutes**
Coal 2	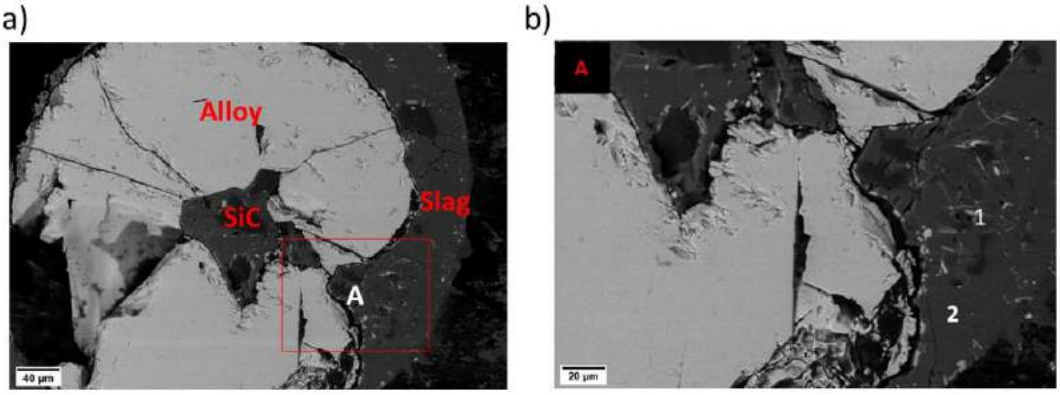

Figure 33: SEM backscattered electron image of the alloy of area A conducted at 20.0 kV. (a) The three phases of alloy, slag and coal existing with the associated SiC phase. Scale bar indicates 40 µm. (b) The two slag phases identified in Area A. Scale bar indicates 20 µm.

Anthracite	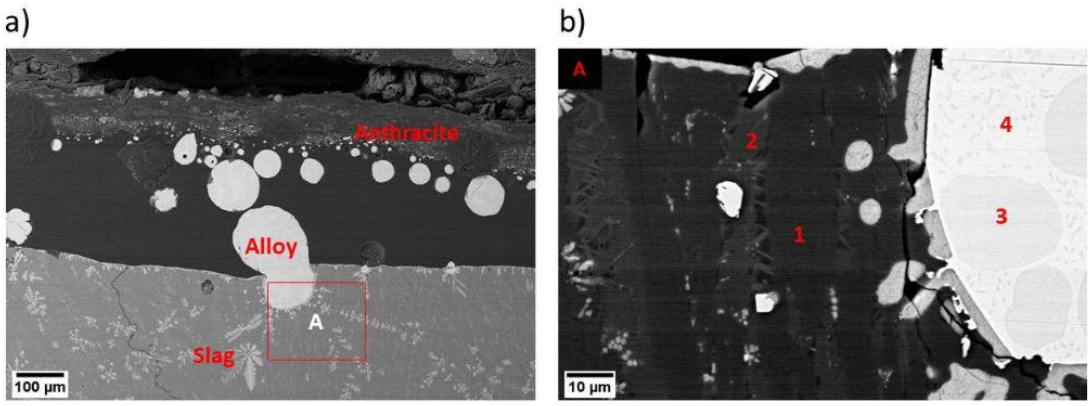

Figure 34: SEM backscattered electron image of Anthracite, slag and alloy conducted at 20.0kV. (a) Interface of slag and Anthracite with the formed alloy and Area A at lower magnification. Scale bar indicates 100 µm. (b) Identified slag and alloy phases from Area A. Scale bar indicates 10 µm.

Table 22: Elemental chemical composition of the alloy phase at 144 minutes reaction time Coal 2 (mass%)

Area	Mn	Si	Total
A	76.2	23.9	100

Table 23: Elemental composition of the identified alloy phases at 144 minutes reaction time Anthracite (mass%).

Area		Si	Mn	Fe	Total
A	3	24.9	75.1	-	100
	4	11.4	80.9	7.7	100

216 minutes reaction time

At 216 minutes reaction time, the slag-carbon interface is displayed in Figure 35 where slag comprised two phases, a primary slag phase high in CaO and SiO_2 and a secondary slag phase associated with needle like crystals high in CaO and contained no MgO. The slag was also associated with a spinel phase which was previously not observed. The spinel is believed to be produced during the solidification as the initial XRD results of the as-received slag revealed no presence of spinel. There are no dendrites present as found in the as-received slag. The alloy consisted of two phases of both Si-Mn-Fe. The presence of Fe in the alloy could indicate that the alloy formed

at this reaction time was due to coalescing of the Fe containing metal prills from the as-received slag. There is a clear interface between the slag and Coal 1 with finely disseminated metal prills found in the coal as well as the slag.

At 216 minutes reaction time for Coal 2, there is still clear contact between the slag and the coal as seen in Figure 36 with the coal exhibiting pores. The alloy phase that is characteristic of a higher Si content than Mn in Table 26 is presented by a single phase, which has been more common in Coal 2 than in Coal 1, where the alloy was found to typically consist of two phases. SiC associated with the alloy is also identified more frequently in Coal 2 than in Coal 1. There are three slag phases identified, presented in Area A. Point (1) as displayed in Area A was a phase high in CaO, SiO_2 and Al_2O_3. (2) is rich in MgO and the bright phase represented as (3) was found to contain high CaO, SiO_2 and Al_2O_3.

From 216 minutes reaction time, the interface between slag and anthracite is still clearly defined in Figure 37 with the alloy forming in between. The slag microstructure is associated with a spinel phase as seen in Area A and corresponding Table 24. The identified slag has two distinct slag phases, a primary slag matrix rich in MgO-SiO_2-CaO and a secondary slag phase, which contains no MgO with a crystalline phase. The dendrite feature as seen in Area A point 3 consists mainly of CaO, Mn and S which is a similar composition to the as-received slag. The alloy composition for Coal 1 in Table 25, displays a Mn proportion of greater than 70 mass %.

Table 24: Elemental composition of the spinel phase found associated with slag (mass%)

Area	MgO	Al_2O_3	Total
B	27.1	67.5	94.6

Reaction time	216 minutes
Coal 1	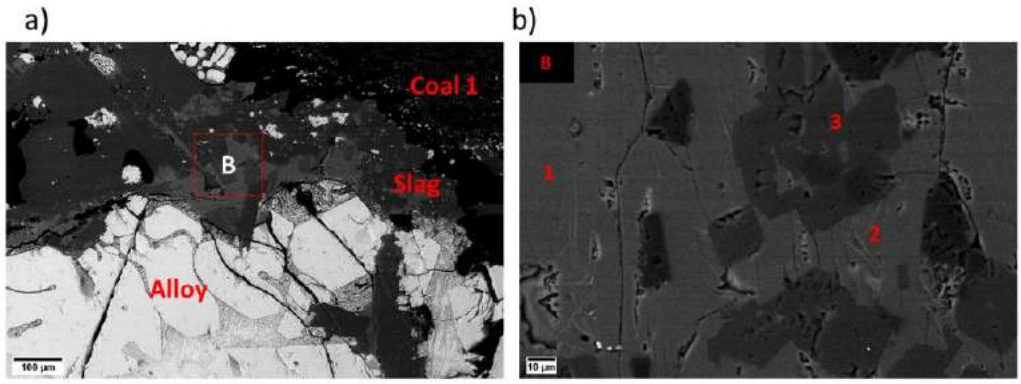

Figure 35: SEM backscattered electron image at 216 minutes reaction time conducted at 20.0kV. (a) Interface between coal and slag with alloy and area B at low magnification. Scale bar indicates 100 µm. (b) The identified slag phases (1) Primary slag phase (2) Secondary slag phase (3) Associated Magnesium alumina spinel phase ($MgAl_2O_4$). Scale bar indicates 10 µm.

Coal 2	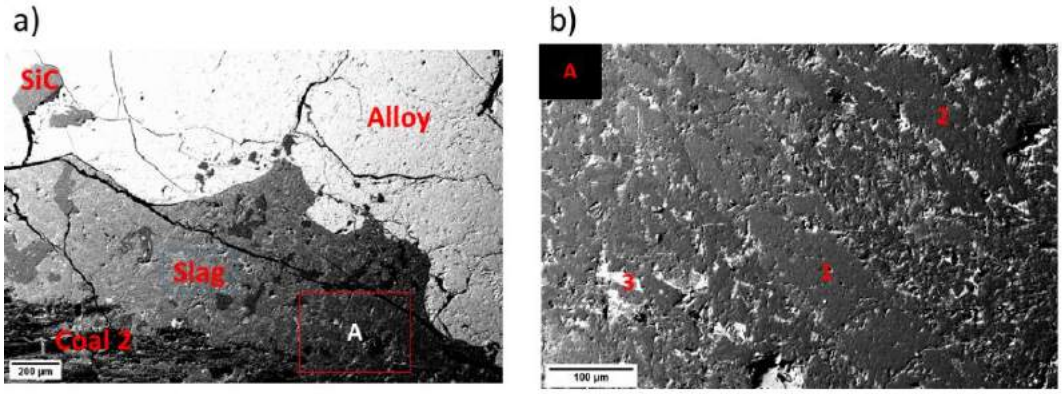

Figure 36: SEM backscattered electron micrograph at 216 minutes reaction time conducted at 20.0 kV. (a) interface of alloy with associated SiC, Coal 2 and slag. Scale bar indicates 200 µm. (b) Area A identifying the different slag phases. Scale bar indicates 100 µm.

Anthracite	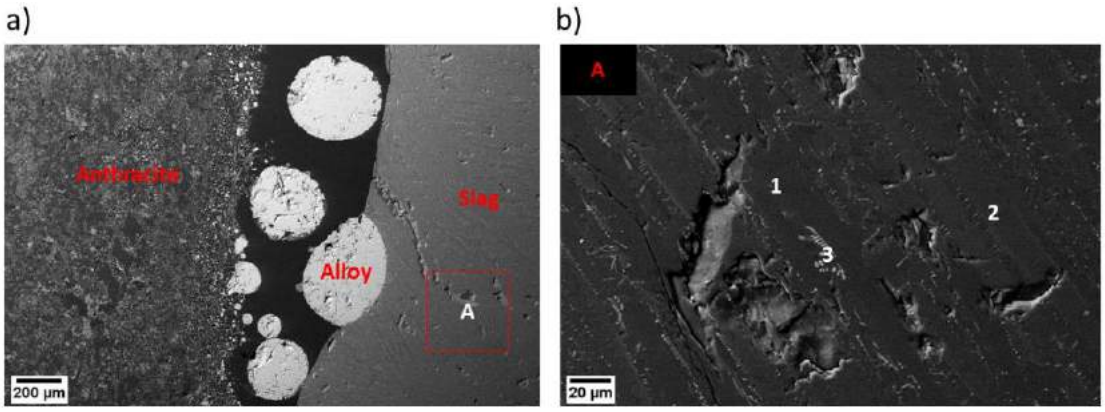

Figure 37: SEM backscattered electron micrograph at 216 minutes reaction time conducted at 20.0 kV. (a) interface of slag- Anthracite with alloy phase. Scale bar indicates 200 µm. (b) Identified slag phases at 216 minutes reaction time. Scale bar indicates 20 µm.

Table 25: Elemental composition of the alloy at 216 minutes reaction time Coal 1 (mass%)

Area	Si	Mn	Total
Alloy	20.9	79.1	100

In Table 26, a lower manganese and higher silicon content of approximately 52 mass% was noted at the slag-metal interface and may be explained by two possible mechanisms. The first one being that silica is reduced by metallic manganese at the metal-slag interface (Sun *et al.*, 2010). The second mechanism suggests the simultaneous MnO and SiO_2 reduction at the slag-carbon interface to alloy. This alloy was also associated with SiC. In Table **27**, two phases were noted for the alloy I Anthracite with Mn in one phase at greater than 70 mass% and at greater than 90 mass % in phase as noted by point 2 in Figure 37 .

Table 26: Elemental composition of the FeMn alloy and SiC at 216 reaction time Coal 2 (mass%)

Area		Si	Mn	C	Total
A	Alloy	52.3	47.7	-	100
	SiC	43.4	-	56.6	100

Table 27: Composition of two phases in alloy at 216 minutes reaction time Anthracite(mass%)

Area	Si	Mn	Total
Alloy	23.8	76.2	100
	8.2	91.8	100

288 minutes reaction time

The slag microstructure of Coal 1 at 288 minutes reduction time appeared different from 216 minutes reaction time in Figure 38. It consisted of a secondary slag phase of elongated crystals high in Al_2O_3 and CaO and no crystalline phase. At this reaction time, it was also observed that there were mostly metal prills in the slag and hardly any large alloy particles at the reaction interface that could have resulted from getting sufficient time to coalesce. The metal prills consisted of two phases, predominantly Si-Mn with a higher Mn mass% proportion.

There is no clearly defined reaction interface between Coal 2 and slag as seen in Figure 39. The coal seemed to have integrated with the slag. The slag microstructure also appeared different, consisting of one phase and presented with coal and metal entrainment. The alloy consisted of one phase as has been the case for Coal 2.

The Anthracite at 288 minutes reaction appeared partially consumed with large alloys formed predominantly consisting of Si-Mn. There was also Titanium carbide (TiC) which was not available at the other reduction times and SiC associated with the alloy. The slag microstructure for Anthracite is similar to 216 minutes reaction time consisted of two phases, a liquid primary phase and a crystalline phase as seen in Figure 40.

Reaction time	288 minutes
Coal 1	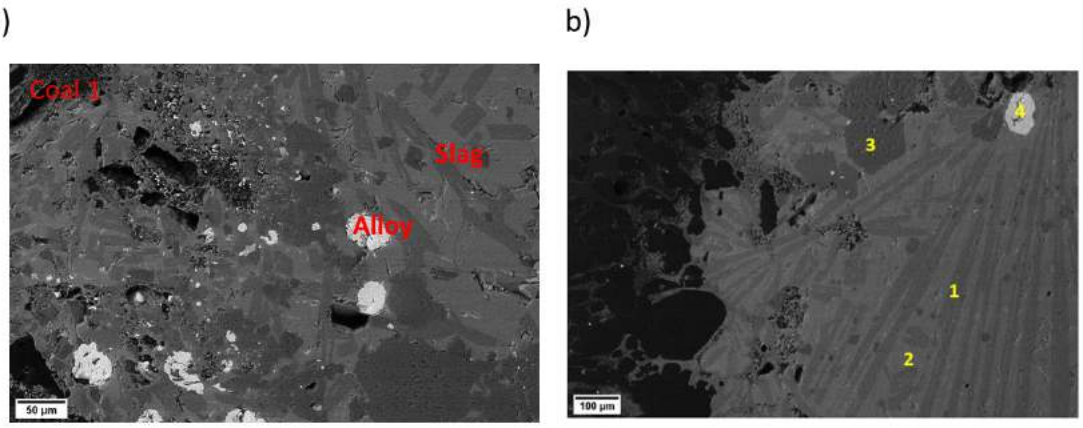

Figure 38: SEM backscattered electron image at 228 minutes reaction time for Coal 1 conducted at 20.0 kV. (a) Coal 1, slag and alloy with metal prills in the slag. Scale bar indicates 50 µm. (b) Slag phases identified. Scale bar indicates 100 µm.

Coal 2	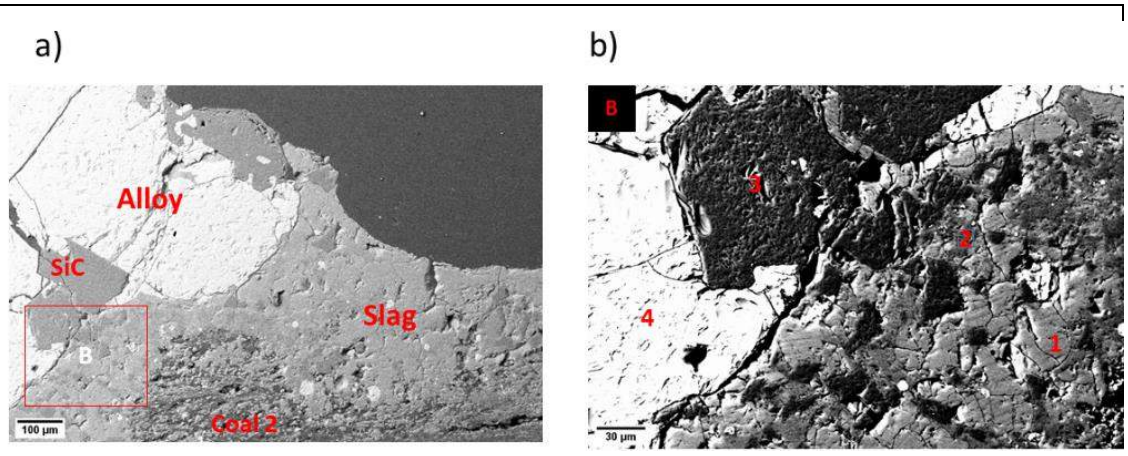

Figure 39: SEM backscattered electron image at 288 minutes reaction time for Coal 2 conducted at 20.0 kV. (a)Coal and alloy interface boundary with identified area B. Scale bar indicates 100 µm(b) Area B with the different slag phases observed, (1) secondary dark spheres phase, (2) primary slag matrix phase (3) SiC, (4) slag vein rich in Ca. Scale bar indicates 30 µm.

Anthracite	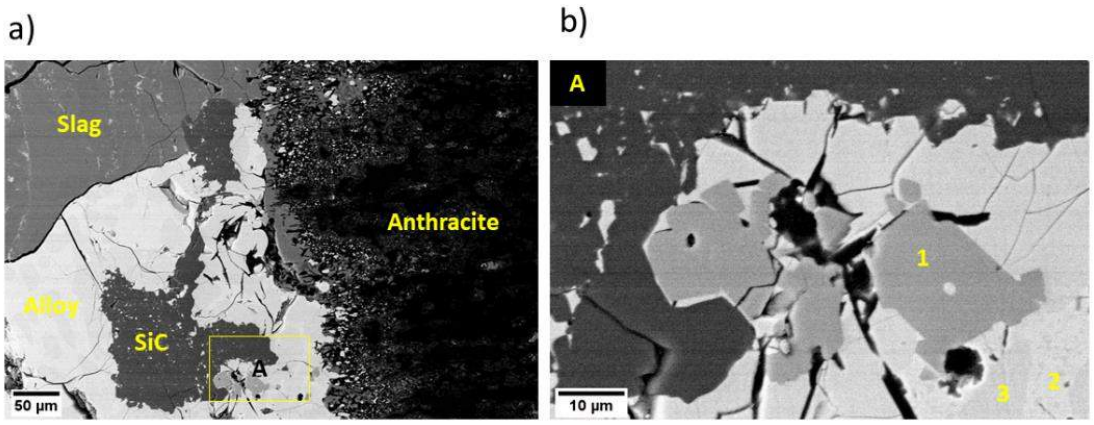

Figure 40: SEM backscattered electron image at 288 minutes reaction time conducted at 20.0 kV. (a) Interface between the slag and anthracite and alloy with SiC. Scale bar indicates 50 µm. (b) Area A with TiC found in the alloy and the Si-Mn alloy phases as indicated by point 2 and 3. Scale bar indicates 10 µm.

The alloy in Coal 1 consisted of two phases with one phase at 79. 1 mass% Mn and the other consisting of greater than 60 mass % Mn as seen in Table 28. In Coal 2, only one alloy phase was noted with Mn proportion reported at about 71.3 mass % in Table 29.

Table 28: Alloy composition at 288 minutes reaction time Coal 1 (mass%)

Area	Si	Mn	Total
Alloy	20.9	79.1	100
	34.5	65.5	100

Table 29: Elemental composition of the alloy phase at 288 minutes reaction time Coal 2 (mass %)

Area		Si	Mn	Total
B	**4**	28.7	71.3	100

Table 30: Alloy composition at 288 minutes reaction time Anthracite (mass%)

Area	Si	Mn	Total
	18.6	81.4	100

360 minutes reaction time

At 360 minutes reaction time, the coal was found porous with the slag depositing in between the pores. The slag consisted of finely disseminated metal prills with alloy at the interface. The alloy was associated with a silicon carbide (SiC) phase, which replaces carbon as the stable carbon-containing phase. MnO can be reduced by solid carbon as well as solute carbon. However, SiO_2 can only be reduced by solute carbon in the presence of metallic Mn.

The slag microstructure at 360 minutes reaction time for Coal 1 was identified to be different from 288 minutes reaction time. It mainly consisted of a primary slag phase composed of Al_2O_3, SiO_2 and CaO and a secondary slag phase that is a network of veins with MgO.

At this reaction time for Coal 2, all the coal has been consumed with no clear reaction interface. The coal was either lost as volatile matter or as a result of reduction. The slag penetrated into the liquid alloy and was composed of a mixture of alloy, TiC, SiC and CaO-SiO_2 rich slag composition as seen in Figure 42.

In Figure 43, there is still a clear reaction interface between slag and anthracite with the slag microstructure is similar to the 288 minutes reaction time Anthracite. Mainly consisting of liquid primary phase and a crystalline phase.

Reaction time	360 minutes
Coal 1	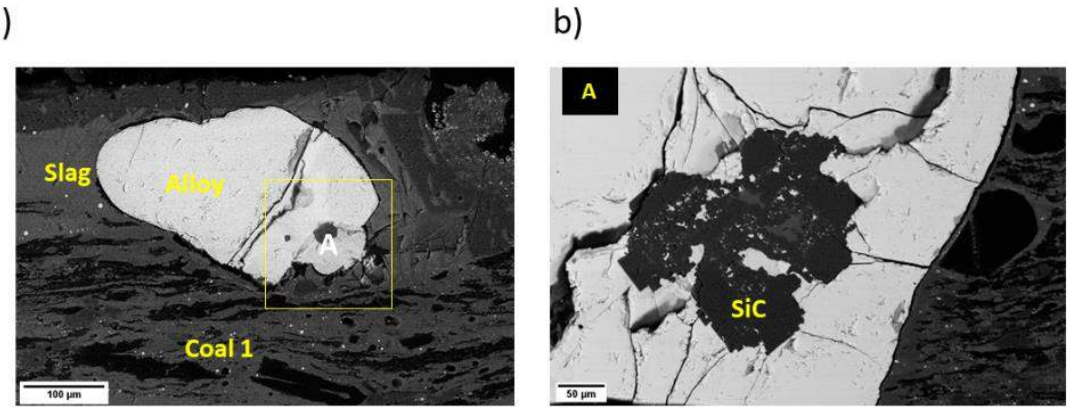

Figure 41: SEM backscattered electron image of the slag- coal interface with alloy at 360 minutes reaction time conducted at 20.0 kV. (a) Slag and coal interface with alloy with focus on area A at low magnification. Scale bar indicates 100 µm. (b) Area A showing associated SiC with the alloy. Scale bar indicates 50 µm.

Coal 2	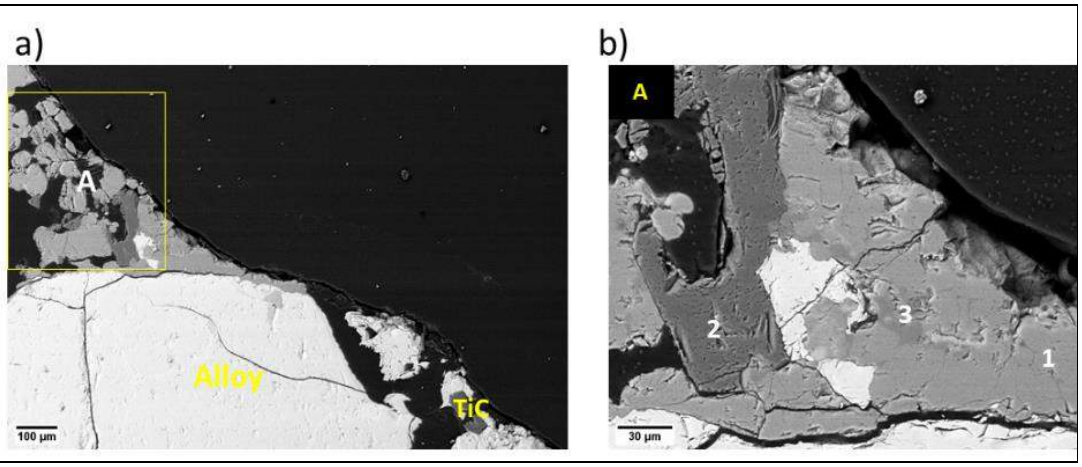

Figure 42: Backscattered electron image at 360 minutes reaction time Coal 2 conducted at 20.0 kV. (a) slag and alloy phases with TiC. Scale bar indicates 100 µm (b) Zoomed Area A with the identified phases associated with slag. Scale bar indicates 30 µm.

Anthracite	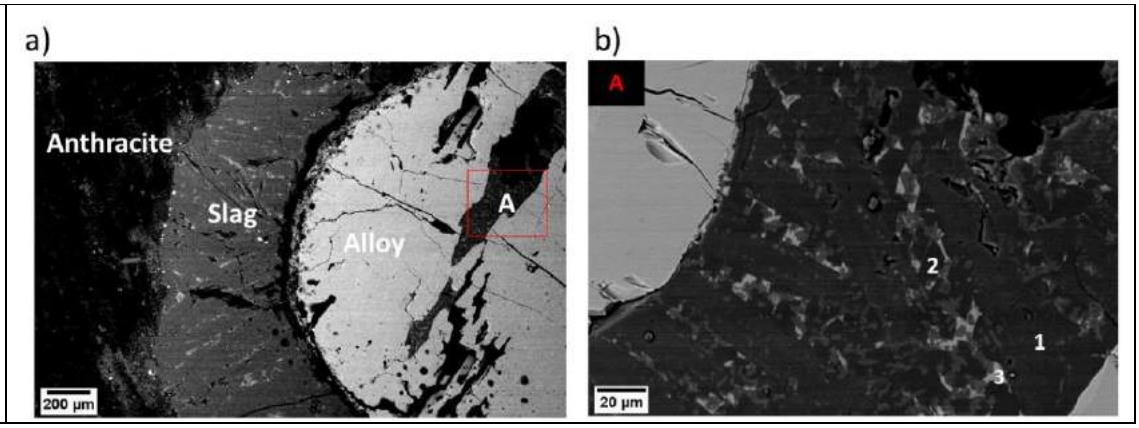

Figure 43: SEM backscattered electron image of the present slag phases at reaction time 360 minutes Anthracite conducted at 20.0kV. (a) Slag anthracite interface. Scale bar indicates 200 µm. (b) Zoomed out Area A of the slag with identified slag phases. Scale bar for area A indicates 20 µm.

The alloy for Coal 1, Coal 2 and Anthracite consisted of a single phase of Si-Mn phase. Coal 1 alloy composition in displays a Mn proportion of 74.2 mass%. Coal 2 in Table 32 is associated with SiC with Mn proportion reported at 87.4 mass% whilst Anthracite in Table 33 reported Mn proportion of the alloy at approximately 77 mass%.

Table 31: Elemental composition of the Si-Mn alloy at 360 minutes reaction time Coal 1 (mass%)

Area	Si	Mn	Total
Alloy	25.8	74.2	100

Table 32: Elemental compositions of the Si-Mn alloy and SiC at 360 minutes reaction time Coal 2 (mass%)

Area	Si	Mn	C	Total
2	44.6	-	55.5	100
Alloy	12.6	87.4	-	100

Table 33: Alloy composition at 360 minutes reaction time Anthracite (mass%)

Area	Si	Mn	Total
Alloy	23.0	77.0	100

In Table *33*, a summary table of the oxide compositions of the primary slag phase as determined by SEM-EDS are presented. In summary, the slag in comparison to the as-received was found to be high in CaO-SiO_2 and in Al_2O_3 in the case that is present. However, CaO, MgO and Al_2O_3 are stable and do not form part of the main reaction so will not be discussed any further. Typically, the MgO was found to dissolve in the secondary phase and CaO in the primary liquid phase before the MgO. Hence, the secondary phase was associated with MgO. SiO_2 content in slag slightly increased as reduction of MnO from the slag had a stronger effect on the slag chemistry than reduction of silica. But the increase was not observed at all the reduction times. It can be concluded that the slag chemical composition irrespective of the microstructure differences is similar in its composition compared to the as-received slag.

Table 34: Oxide composition of the slag at different reaction times for the different carbonaceous reductants

	Reduction time (min)	Al_2O_3	MnO	SiO_2	MgO	CaO	BaO
As-received slag	**0**	**3.5**	**26.3**	**36.8**	**5.9**	**32.5**	**-**
Coal 1	72	9.4	1.1	38.3	8.5	40.1	-
	144	-	-	-	-	-	-
	216	32.4	-	20.3	-	40.2	-
	288	32.5	-	21.8	-	42.5	-
	360	33.8	-	39.5	-	21.2	-
Coal 2	72	3.4	-	44.9	10.5	37.5	-
	144	24.0	-	37.2	5.6	28.5	-
	216	15.3	-	40.7	8.3	31.2	-
	288	25.4	-	30.2	-	42.53	-
	360	2.9	-	51.8	1.2	44.1	-
Anthracite	72	5.3	-	52.3	12.2	38.4	-
	144	-	-	44.5	12.8	47.4	-
	216	-	-	50.3	12.0	42.7	-
	288	4.6	-	51.4	12.9	45.9	-
	360	4.3	1.8	45.5	3.2	51.3	2.8

Determining MnO concentrations with SEM-EDS from the slag as seen in Table 34 proved to be a challenge especially for Coal 1 and Coal 2. The reason could be that the slag was most likely reduced from a two-phase area. Safarian and Tangstad (2010) conducted a study that found that if a slag is reduced in a single phase, the chemical composition measurements can be used to evaluate slag-carbon reactivity. However, the same is not possible in a two-phase area. Another possible explanation could be that in Anthracite where it was possible to determine the MnO content from slag, there was slag present at all the reduction times with clearly defined slag/carbon interface. This was not always observed in Coal 1 and Coal 2 where at higher reduction times, the slag/carbon interface was not always defined with sometimes little or no slag present either due to devolatilization or as a result of reduction.

The MnO concentrations from the slag as displayed in Table 35 were mostly determined from the secondary slag phase as it was difficult to determine MnO content from the primary phase using SEM-EDS. As such, it was inconclusive to compare the reduction rates of MnO from the slag from the carbonaceous reductants. It was also not possible to report with confidence if the reduction rate increased with increasing MnO content in the slag. Thus, a highly reactive reductant did not equate to a higher MnO reduction rate. However, in Anthracite, the trend was more obvious where MnO content decreased with an increase in reduction time.

Table 35: Summary table of MnO in slag at the different reduction times (mass%)

Reaction time (min)	**MnO mass % in slag**		
	Anthracite	**Coal 1**	**Coal 2**
0	21.5	21.5	21.5
72	18.3	2.0	17.9
144	18.8	-	3.5
216	9.0	6.9	1.9
288	3.4	1.6	-
360	1.8	-	-

The yield of Mn in the alloy varied with no trend observed with exception of Anthracite. However, despite tentative, the results were able to show an increase in Mn in the alloy indicative of reduction. The alloy measurements were mostly determined at the slag/carbon interface than in the slag matrix.

Table 36:Summary table, elemental composition of Mn in metal as a function of reaction time (mass%)

Reaction time (min)	Mn wt. % in alloy phase		
	Anthracite	Coal 1	Coal 2
0	0	0	0
72	60.7	75.9	79.1
144	75.1	-	76.2
216	76.2	79.1	47.7
288	81.4	79.1	71.3
360	77.0	74.2	87.4

Based on the above observations as well as previously conducted work, possible mechanisms of MnO reduction from the slag could be deduced and possibly provide better understanding of the factors that influence reductant reactivity to slag.

- Most of the Mn in alloy measurements were mostly determined at the slag-carbon interface which was found to be much higher than Mn determined from alloy surrounding slag. The alloy composition determined as seen in

- Table *35* displayed some sort of trend where the yield of Mn increased with reduction time except at 360 minutes reaction time. In Coal 1 and Coal 2, the alloy composition was sometimes determined within the slag matrix due to a non-existent interface of carbon and slag.
- The presence of Fe in the alloy in the system allows for MnO reduction by the dissolved carbon in the alloy.
- The solid carbon was mainly dissolved into the alloy in order for the alloy to become carbon saturated. The likelihood of the carbon dissolved in the slag is unlikely. "There is a small potential for solubility of C in slag in the form of a carbide i.e. ions of for example Si^{2+} and C^{2-} as this is a very reducing system. It is a good question if this dissolved C will react with the MnO in the slag. I [do not] think so, as the C^{2-} is already in a reduced state there [should not] be a driving force for it to react with the O_2. I don't think this has been tested experimentally before, though."(P.C. Pistorius, personal communication, November 15, 2022).
- The presence of metal prills in the slag indicates that they are transferred from reaction interface to the slag through gas bubbles (Tangstad and Safarian,2010).
- The as-received slag consisted of Fe metal prills, which were sometimes found in the reduced alloy. It has been suggested that the presence of Fe metal prills increases the rate of reduction (Tranell *et al.,* 2007; Skjervheim, 1995). Even though this observation could not be proven in this study, where a direct correlation of increased reduction rate was observed due to the presence of metallic Fe.

4.3.3 Petrographic observations

The following series of microscopic images depict the evolution of the identified macerals when heated. In Figure 44, the vitrinite macerals which form part of the reactive macerals exhibited pores as a result of devolatilization. Reactive macerals such as the identified vitrinite macerals when subjected to high temperatures, release the volatile matter derived from the breakdown of the aliphatic chains and the remaining aromatic carbon-rich molecular structure softens, swells, and becomes porous. The rest of the microscopic images are contained in **APPENDIX C** where the evolution of vitrinite from parent coal progressively becoming porous as a function of time are observed. On the other hand, unreacted inert macerals possess no pores as identified

in Figure 44 when subjected to heat as they are slow to change and devolatilise at higher temperatures.

Coal 1 reacted samples

Scale bar indicates 100 μm

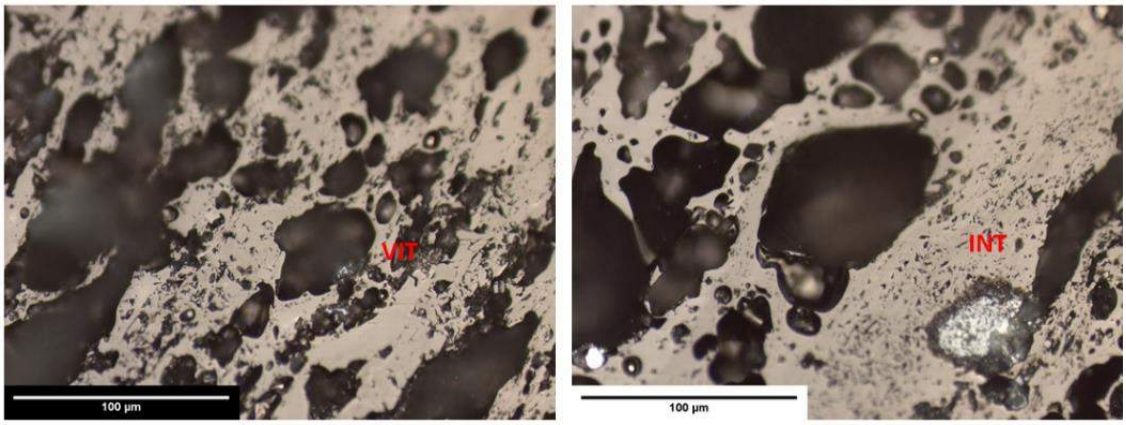

A **B**

Figure 44: Plate A and B showing the evolution of the vitrinite and inertinite when heated at 72 minutes reaction time

A- Porous reactive vitrinite bands showing signs of devolatilization at 72 minutes reaction time.

B – An unreacted inert fusinite at 72 minutes reaction time with associated mineral matter.

Coal 2 reacted samples

At same reaction time for Coal 2, larger pores were noted from the vitrinite macerals as seen in Figure 45. This could indicate that Coal 2 potentially releases volatile matter at a greater rate than Coal 1. Plates C and D show mineral matter and a partially porous semifusinite which is an inertinite maceral.

Scale bar indicates 100 μm

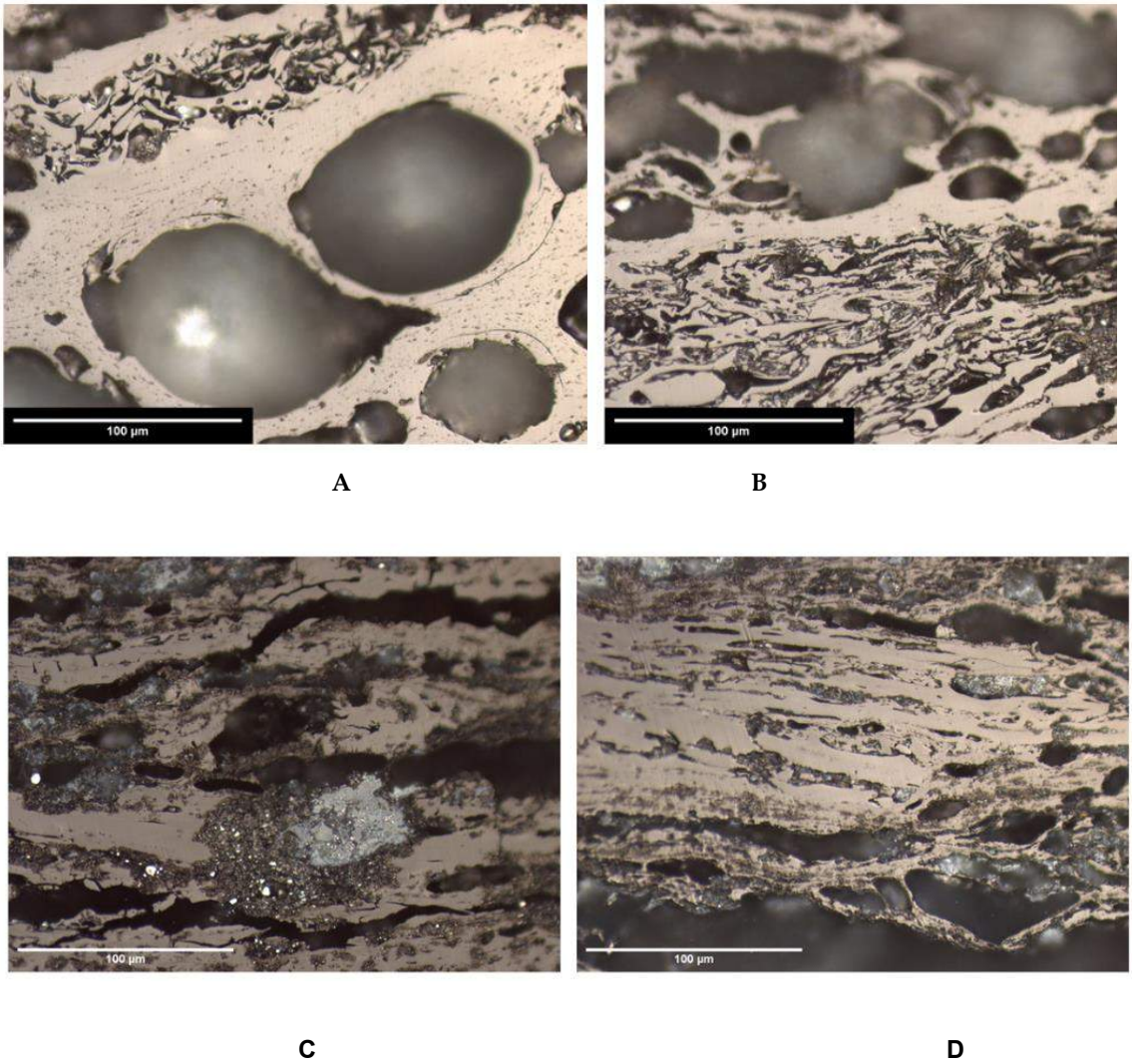

Figure 45: Plates A- D for Coal 2 showing the progression as a function of reaction time.

A, B- Unreacted fusinite and highly porous particle likely derived from vitrinite rich band at 72 minutes reaction time.

C, D- Partially consumed fusinite with visible mineral matter at 144 minutes reaction time.

Anthracite reacted samples

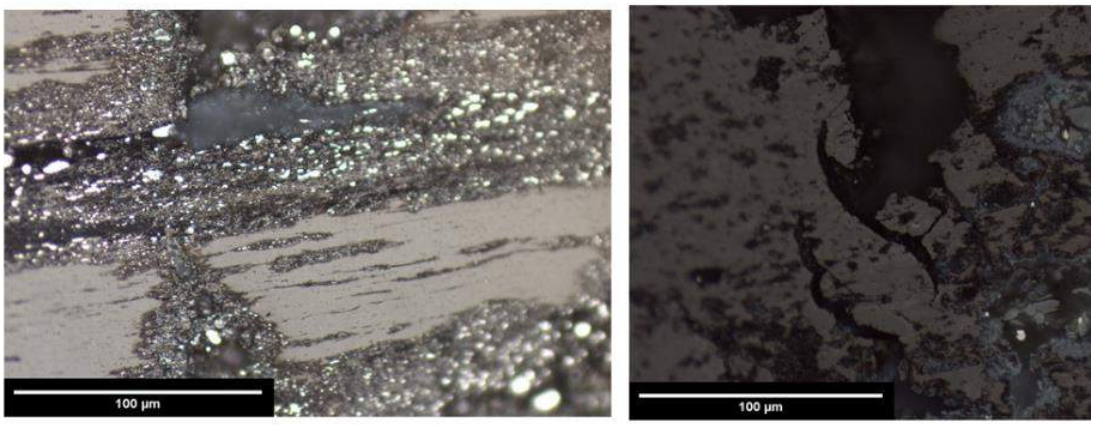

A **B**

Figure 46: Plates A-B for Anthracite showing evolution of macerals at 216 minutes reaction time

A,B- Porous vitrinite rich bands and unreacted likely from inertinite rich bands from 216 minutes reaction time with finely disseminated mineral matter and metal prills.

5 DISCUSSION

5.1 Effect of coal rank

Coal 1 and Coal 2 were established to belong to the same coal rank classified as medium-rank C bituminous coal as determined by vitrinite reflectance with comparable rank indicator parameters of volatile matter and fixed carbon. On the other hand, Anthracite was found to belong to a higher ranked coal rank. Coal rank is found associated with changes in geochemical properties such as volatile matter and fixed carbon (O'Keefe and Mastalerz, 2011) in Figure 47.

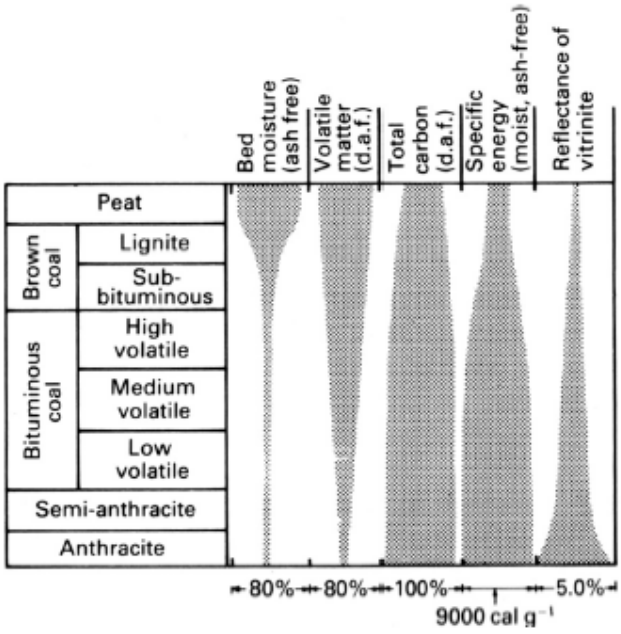

Figure 47: Variation of key coal properties with coal rank (Ward, 2008(ed.))

The differences in terms of volatile matter and fixed carbon cited between Coal 1 and Coal 2 with Anthracite are linked to coal rank and possess an opposite trend. Generally, as rank increases, volatile matter content decreases and leads to a reciprocal carbon content enrichment due to the geochemical changes the coal undergoes with progression of rank or maturity. This was observed in Coal 1 and Coal 2 belonging to the same coal rank possessing a higher volatile matter and less carbon content compared to a higher ranked carbon rich and low volatile matter Anthracite in Figure 48. In bituminous coals, the amount of volatile matter mainly consists of aliphatic components. Whilst during the anthracitic stage, a decrease of hydrogen/carbon ratio

in anthracites corresponds to a sudden orientation of aromatic units with high degree of ordering with a change in molecular structure noted with change in rank (Teichmüller and Teichmüller 1968).

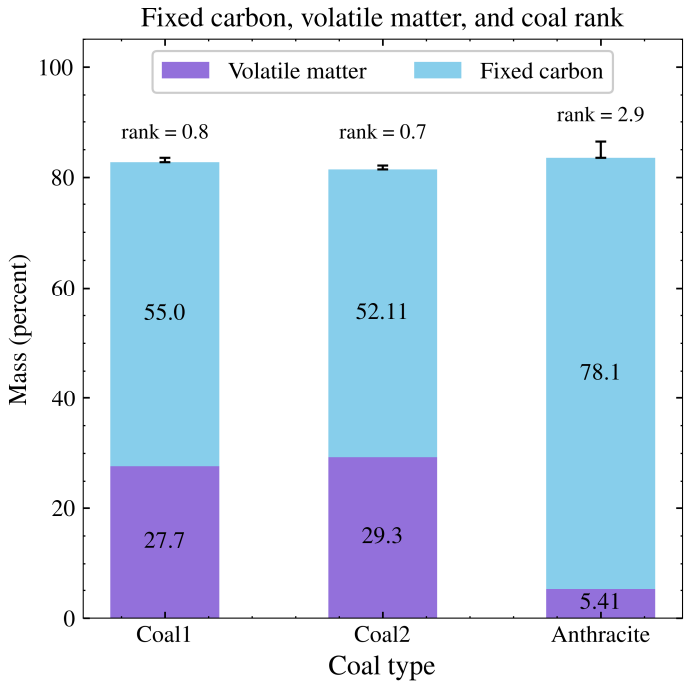

Figure 48: Coal rank relationship with volatile matter and fixed carbon for Coal 1, Coal 2 and Anthracite

The mass loss from the reactivity tests indicated a rapid initial mass loss specifically for Coal 1 and Coal 2, which were attributed to devolatilization. For instance, Coal 2 with a highest volatile matter content as determined by proximate analysis exhibited a higher initial mass loss compared to Coal 1 and Anthracite. On the other hand, Anthracite exhibiting the least initial mass loss had the least volatile matter. The influence of coal rank was evidently relevant with Anthracite where the reactivity is largely influenced by coal rank and to a lesser extent by the maceral composition. The higher rate of devolatilization for Coal 1 and Coal 2 reinforces the relationship between coal rank and properties such as volatile matter and fixed carbon. The boundaries that separate the different categories of coal rank are justified by important changes in coal properties or behaviour (Pinheiro, 2006).

The second stage of mass loss was attributed to reduction. The mass loss as a result of reduction is quantified by calculating the difference between the determined volatile matter and total mass loss. This is supported by evidence of MnO reduction in slag to Mn in alloy as determined by SEM-EDS. The SEM-EDS results revealed Mn in the alloy as a result of MnO reduction from the slag indicate that a reactive reductant does not translate to a higher yield of Mn in the alloy phase as function of reduction time but rather indicates the presence of metallic Mn in the alloy. The reductant reactivity test results revealed that reactivity translated as mass loss decreased with an increase in coal rank. A higher ranked Anthracite was found to have the least mass loss. In overall, Coal 2 was found to have more mass loss than Coal 1.

It is also worth noting that the coal properties are not only determined by the rank but by its composition as well. Therefore, the inherent organic composition such as maceral content might provide some distinctive chemical and physical differences when heated between the two similar reductants (Coal 1 and Coal 2). As the behaviour of the reductant type is influenced by rank and maceral composition which are two independent and separate factors (Ward, 2008).

5.2 Effect of maceral analysis

The maceral analysis performed indicated that the principal reactive maceral such as vitrinite exhibited structural changes upon heating. As such, on being heated, reactive macerals are known to devolatilise easily with increasing temperature and rank (Falcon and Ham,1988) consequently swell and become porous. The initial stage of mass loss observed was due to the thermal decomposition which entails a release of volatiles leading to changes in morphology and molecular structure of the macerals (Falcon *et al.*,2018). This is related to its chemical properties where vitrinite is found to be volatile matter and hydrogen rich in low rank bituminous coals.

Once devolatized, the remaining molecules re-align becoming graphitic and crystalline. Such a structure breaks down in a liquid slag resulting in the dissolution of the carbon into the molten alloy. On the other hand, the principal unreactive maceral such as inertinite as determined by maceral analysis was observed not to change in its structure upon heating. Falcon *et al.*, (2018) also suggested that anthracite irrespective

of maceral type does not swell or form porous chars. Inertinites are generally poor in volatiles, and will not swell and become porous at any temperature due to the dense structure. In terms of its chemical reactivity, inertinite is found to be more aromatic and richer in carbon structured molecules (Falcon *et al.*,2018). The reactive and inertinite macerals are not only found petrographically distinct but also possess differences in their chemical and physical properties (Nag *et al.*, 2018)

The mass loss observed from the coal with slag which translates to reactivity was mainly due to contribution of devolatilization of the coals and reduction reaction between coal and slag. Studies using thermogravimetry to generate mass loss curves revealed that the mass loss is largely due to the release of volatile matter and reduction of the manganese (Patricia, 2018). To what extent the reactive and inertinite macerals play a role in devolatilization and reduction is still a matter that needs to be further investigated. However, based on the studies on the behaviour of the macerals when heated, Coal 1 and Coal 2 which consist of reactive macerals and are of low rank have shown to devolatilise at a higher rate than Anthracite. Once devolatilised, the vitrinitic char could have played a role in reduction by dissolving in the liquid phase resulting in reduction. This would be more evident at higher reduction times. On the other hand, semi-reactive forms of inertinite may release some volatiles thereby contributing to the mass loss at higher reaction times such as between 216-288 minutes reaction time.

Coal 2 with a higher proportion of volatile matter from proximate analysis and a higher proportion of reactive macerals, which both relate to the release of volatile matter was found to have the highest mass loss. In contrast, Anthracite consisting of the highest proportion of inertinite, the reactivity tests confirmed Anthracite to have the least mass loss. However, the reactivity of Anthracite was primarily influenced by coal rank more than the maceral content of inertinite.

The relationship is thus explored through the response of the carbonaceous reductants to slag during the reactivity tests relative to their reactive and unreactive maceral compositions. The carbonaceous reductant with the highest reactive maceral such as Coal 2 as determined petrographically was the most reactive from the reactivity tests. Moreover, the reductant with the highest inertinite macerals was the least reactive.

However, it is apparent that no single parameter can determine the reductant reactivity to slag.

What was achievable from the determined maceral analysis is the individual chemical reactivities of the macerals and their contribution to devolatilization. Due to the nature of the reductant reactivity tests conducted in a chamber furnace, the extent of devolatilization can only be inferred through literature where volatile matter is typically released at temperatures above 400°C (Speight, 2015).

6 CONCLUSIONS AND RECOMMENDATIONS

The conclusions from the study are as follows:

- The studied Coal 1 and Coal 2 exhibited similar chemical properties such as volatile matter and fixed carbon derived from proximate analyses. Anthracite consisted of less volatile matter and higher fixed carbon. These chemical properties are linked to coal rank: Coal 1 and Coal 2 were classed in same rank whilst Anthracite belongs to a higher coal rank hence the different chemical properties observed.
- In terms of coal rank, from the reactivity tests conducted it was determined that the carbonaceous reductant reactivity to slag was higher in lower ranked coals such as Coal 1 and Coal 2 and lower reactivity was observed in higher ranked Anthracite.
- Coal 1 and Coal 2 examined were characterised by a high proportion of total reactive macerals compared to Anthracite. On the other hand, Anthracite was characterised by a high inertinite proportion. The carbonaceous reductant reactivity to slag showed systematic trend and increased with increasing proportion of reactive macerals.
- The maceral analysis results showed that Coal 2 with the highest proportion of reactive macerals relative to the inert macerals exhibited the highest mass loss. Reactive macerals upon heating devolatilize, change in structure, texture and form. However, no information was gathered on how the reactive and inert macerals react with the slag as a result of reduction but a relationship of the relative chemical reactivities of macerals and structural changes upon heating was established.

Recommendations for further study:

- Further study to separate macerals from parent coal through density differences of the macerals to obtain pure macerals in order to understand the chemical properties of individual macerals when heated. Concentration of the macerals by methods such as heavy liquid separation could be employed to separate the macerals at different specific gravities. The individual macerals possess different specific gravities and behave differently when heated. This could ultimately

establish basis of comparison for the individual macerals in relation to the slag when heated.

- Determination of the micropore surface area and microporosity to study the evolution effect of devolatilization on the carbonaceous reductants.
- Complement fundamental coal characterisation methods by conducting further coal characterisation techniques on the carbonaceous reductants. Determination of the physical structural characteristics of the coal will consequently provide the role the parameters play on the reactivity of carbonaceous reductants to slag.
- Raman spectroscopy in order to infer chemical structure and physical changes of coal in relation to the petrography results. Raman spectroscopy will provide information on the atomic ordering of coal.
- A series of thermogravimetric tests at different testing coupled with off-gas analysis at different temperature targets would also be useful for comparison reasons as well as to analyse the thermal changes of the coal relative to the slag. Different gas analysis techniques that can be used such as gas chromatography.

7 REFERENCES

1. Akdogen, G. and Eric, H.R., (1995),' Kinetics of the solid-state carbothermic reduction of Wessel manganese ores', *Metallurgical and Materials Transactions B,* vol.26, pp.13-24.
2. Arnold, B J., (2013), 'Coal formation', Osborne, D., (ed.), *The coal handbook: Towards cleaner production,* Woodhead Publishing, pp. 31-52.
3. ASTM International, (2017), 'Standard test method for measuring coke reactivity index (CRI) and coke strength after reaction (CSR)', *ASTMD -5341-17.*
4. ASTM International, (2015), 'Standard methods for proximate analysis of coal and coke by macro thermogravimetric analysis', *ASTDM D7582-15.*
5. ASTM International, (2009), 'Standard specification for ferromanganese', *ASTDM A99-03.*
6. Bagirathi, N., (2012), 'Evaluation of the reactivity of anthracites in respect to its chemical and petrographic characteristics in an ilmenite smelting operation', *MSc Dissertation*, University of Witwatersrand.
7. Boss, C.B., and Freeden, K. J., (2004), '*Concepts and Techniques in inductively coupled plasma optical emission spectrometry*', Perkin Elmer, 3rd ed., pp. 2-12.
8. Cairncross, B., (2001), 'An overview of the Permian (Karoo) coal deposits of Southern Africa', *African Earth Sciences,* vol. 33, pp. 529- 562.
9. Chakravarty, S., Mohanty, A., Banerjee, A., Tripathy, R., Mandal, G.K., Basariya, R., and Sharma, M., (2015), 'Composition, mineral matter characteristics and fusion behaviour of some Indian coals', *FUEL,* vol. 150, pp 96-101.
10. Chen, P., and Ma, J., (2002),' Petrographic characteristics of Chinese coals and their application in coal utilization processes', *FUEL,* vol. 81, pp. 1389-1396.
11. Choudhury, N., Mohanty, D., Boral, P., Kumar, S., and Hazra, S.K., (2008), 'Microscopic evaluation of coal and coke for metallurgical usage', *Current Science,* vol.94, pp. 74-81.
12. Coetsee, T., (2018),' Ore smelting in high carbon ferromanganese production: "It works in practice, but does it work in theory?" *INFACON XV: International Ferro-Alloys Congress,* Cape Town, 25-28 February, pp.1-13.
13. Diessel, C.F.K., (1992), *Coal-bearing depositional systems*. Springer, Berlin.
14. Eidem, P.A., Tangstad, M., Bakken, J.A., and Ishak, R., (2010), 'Influence of coke particle size on the electrical resistivity of coke beds', *The Twelfth International Ferroalloys Congress: Sustainable Future,* Helsinki, Finland, June 6-9. pp.349-358.
15. Falcon, R.M.S., and Snyman, C.P., (1986), 'An introduction to coal petrography: Atlas of petrographic constituent in the bituminous coals of Southern Africa', *The Geological Society of South Africa*, Johannesburg.
16. Falcon, R., (2013), *Coal Petrography. The coal handbook: Towards cleaner production*, Woodhead Publishing limited, pp. 53-79.
17. Falcon, R., and Ham, A.J., (1988), 'The characteristics of Southern African coals', *Journal of the South African Institute of Mining and Metallurgy,* vol.88, no.5, pp.145-161.
18. Falcon, R., and Falcon, R.M.S., (1987), 'The petrographic composition of Southern African coals in relation to friability, hardness, and abrasive indices', *Journal of the South African Institute of Mining and Metallurgy,* vol.87, no.10, pp.323-336.

19. Falcon, R., Wagner, N., and Malumbazo, N., (2018), *Southern African coals and carbons: definitions and applications of organic petrology,*1st ed, Struik Nature, Cape Town.
20. Finkelman, R.B., Dai, S., and French, D., (2019), 'The importance of minerals in coals as the hosts of chemical elements: a review', *International Journal of Coal Geology,* vol. 212, pp. 10325.
21. Gaal,S., Berg, K., Tranell, G., Olsen, S.E., and Tangstad,M.,(2004), 'An investigation into aspects of liquid phase reduction of manganese and silica containing slag', The South African Institute of Mining and Metallurgy, pp. 651-658.
22. Gray, R.J., and Devanney, K.F., (1986), 'Coke carbon forms: microscopic classification and industrial applications', *International Journal of Coal Geology*, vol. 6, pp.277 – 297.
23. Gray, R.J., Buo, T.V., and Patalsky, R.M., (1999), 'Reactivity and petrography of cokes for ferrosilicon and silicon production', *International Journal of Coal Geology,* vol. 43, pp. 243-253.
24. Jeffrey, L.S., (2015), 'Characterization of the coal resources of South Africa', *The Journal of the South African Institute of Mining and Metallurgy,* pp. 95-102.
25. Jordan, P. 2006. Characterising coals for coke production and assessing coke- predicting coke quality based on coal petrography, rheology and coke petrography. *MSc Dissertation*, University of Witwatersrand, pp. 1-111.
26. Kim, P.P., (2018), 'Reduction rates of SiMn slags from various raw materials', *PhD Thesis*, Norwegian University of Science and Technology.
27. Kolbeinsen, L., Safarian, J., Grong, O., and Olsen, S.E., (2006), 'A process Model for the carbothermic Reduction of MnO from High Carbon Ferromanganese Slag- The Model', *ISIJ International,* vol. 46, no. 8, pp. 1120-1129.
28. Kononov, R., Ostrovski, O., and Ganguly, S., (2007), 'Carbothermal solid state reduction of manganese ores', *INFACON XI,* pp. 259-267.
29. Krishnamoorthy, V., and Pisupati, S.V., (2015), 'A critical review of mineral matter related issues during gasification of coal in fixed, fluidized, and entrained flow gasifiers', *Energies*, vol 8, pp 10430-10463.
30. Lindstad, T., Tangstad, M., and Olsen, S.E., (2007), *Production of Manganese Ferroalloys*. Tapir academic press, Trondheim.
31. Lundgren, M., Okvist, L.S., and Bjorkman, B., (2009), 'Coke reactivity under blast furnace conditions and in the CSR/CRI test', *Steel Research International,* vol.80, no.6, pp.396-401.
32. Madias, J., (2011), 'A review of the production of ferromanganese in blast furnace', *AISTech Proceedings,* vol.1, pp.401-412.
33. Magnus, E., (2017), 'Alternative methods for coal resource classification of the geologically complex Witbank coalfield', *MSc dissertation,* University of Witwatersrand.
34. Maledi, N.B., (2017), 'Characterisation of Mineral Matter in South African Coals using Micro-Raman spectroscopy and other techniques', *PhD Thesis,* University of Witwatersrand.
35. Malumbazo, N., Wagner, N. and Bunt, J.R., (2012), 'The petrographic determination of reactivity differences of two South African inertinite-rich lump coals', *Journal of Analytical and Applied Pyrolysis,* vol.93, pp. 139-146.
36. Mastalerz, M and O'Keefe, J.M.K., (2011), 'Spontaneous combustion and coal petrology, Stracher, G.B., Prakash, A., and Sokol, V., (eds.), *Coal and peat fires: A global perspective* ,vol. 1, https://doi.org/10.1016/C2009-0-16444-9.

37. Miller, K., (2013), *Coal Analysis*, *The coal handbook towards cleaner production*, vol.1, Woodhead Publishing Limited, pp. 151- 180.
38. Monsen, B., Tangstad, M., Solheim, I., Syvertsen, M., Ishak, R., and Midtgaard, H., (2007), 'Charcoal for manganese alloy production', *INFACON XI*, pp.298-310.
39. Monsen, B., Tangstad, M., and Midtgaard, H., (2004), 'Use of charcoal in silicomanganese production', *INFACON X,* Cape Town, South Africa, pp. 392-404.
40. Moroeng, O.M., Mhuka, V., Nindi, M.M., Roberts, R.J., and Wagner, N.J., (2019), 'Comparative study of a vitrinite rich and an inertinite rich Witbank coal (South Africa) using pyrolysis-gas chromatography', *International Journal Coal Science and Technology,* vol.6, no.4, pp. 621-632.
41. Mukhopadhyay, P.K., (1994), 'Vitrinite Reflectance as Maturity Parameter', *ACS Symposium: American Chemical Society*.
42. Myrvagnes, V., (2008), 'Analyses and characterization of fossil carbonaceous materials for silicon production', *PhD Thesis, Norwegian* University of Science and Technology.
43. Nag, D., Kopparthi, P, P., Dash, P.S., and Saxena, V.K., (2018), 'Enrichment of reactive macerals in coal: its characterization and utilization in coke making'. *Metallurgical Research and Research and Technology,* vol. 115, https://doi.org/10.1051/metal/2017094.
44. O'Brien, G., Jenkins, B., and Beath, J.E., (2002), 'Coal characterisation by automated petrography', *FUEL,* vol. 28, no.9, pp. 1067-1073.
45. O' Keefe, J.M.K., Betchel, A., Christanis, K., Dai, S., DiMichele, W.A., Eble, C.F., Esterle, J.S., Mastalerz, M., Raymond, A.L., Valentim, B.V., Wagner, N.J., Ward, C.R., and Hower, J., (2013), 'On the fundamental differences between coal rank and coal type', *International Journal of Coal Geology,* vol. 118, pp. 58-87.
46. Olso, V., Tangstad, M. and Olsen, S.E., (1998),'Reduction kinetics of MnO saturated slags', *INFACON 8*. pp.279-283.
47. Ostrovski, O., and Swinbourne, D., (2013), 'Slags in production of manganese alloys', *Steel Research International*, vol. 84, Issue 7, pp. 680-686.
48. Pickel, W., Kus, J., Flores, D., Kalaitzidis, S., Christanis, K., Cardott, B.J., Misz-Kennan, M., Rodrigues, S., Hentschel, A., Hamor-Vido, M., Crosdale, P., Wagner, N., and ICCP., (2017), 'Classification of liptinite-ICCP System 1994', *International Journal of Coal Geology,* vol. 169, pp. 40-61.
49. Pinheiro, H., (2006), 'Springlake Anthracite- Characterisation and potential Industrial Utilisation', *PhD Thesis*, Universidade do Porto, pp. 1-136.
50. Pistorius, P.C., (2002), 'Reductant selection in ferro-alloy production: The case for the importance of dissolution in the metal', *Journal of the South African Institute of Mining and Metallurgy,* pp. 33–36.
51. Pochart, G., Joncourt, L., Touchard, N., and Perdon, C., (2007), 'Metallurgical benefit of reactive high-grade ore in manganese alloys manufacturing', *Proceedings of INFACON XI,* New Delhi, India, 18-27 February, pp. 217-230.
52. Raanes, O., and Gray, R.J., (1995), 'Coal production of silicon rich ferroalloys', *INFACON 7,* Trondheim, Norway, pp. 201-220.
53. Rankin, W.J., and Van Deventer, J.SJ., (1980), 'The kinetics of reduction of manganese oxide by graphite', *Journal of the South African Institute of Mining and Metallurgy,* vol.80, pp.239-247.
54. Richards, J.M., Naude, G., Theron, S., and McCullum, M., (2013), 'Petrological characterisation of coal: an evolving science', *Journal of South African Institute of Mining and Metallurgy,* vol. 113, no. 11, pp. 865-875.

55. Ringdalen, E., Tangstad, M., and Gaal, S., (2009),'Initial melting and reduction of ore and fluxes at the top of the coke bed during SiMn-production', *Molten,* Santiago, Chile, pp.1164-1172.
56. Ringdalen, E., Tangstad, M., and Brynjulfsen, T., (2015), 'Melting behaviour of Mn sources-effect on furnace performance', *The fourteenth International Ferroalloys Congress: Energy efficiency and environmental friendliness are the future of the global Ferroalloy industry*, Kiev, Ukraine, May 31-June 4. pp.436-445.
57. Safarian, J., and Kolbeinsen, L., (2008), 'Kinetic of carbothermic reduction of MnO from High- carbon Ferromanganese Slag by graphite materials', ISIJ *International,* vol. 48, no.4, pp. 395-404.
58. Safarian, J., Kolbeinsen, L., Tangstad, M., and Tranell, G., (2009), 'Kinetics and mechanism of the simultaneous carbothermic reduction of FeO and MnO from High-carbon ferromanganese slag', *Metallurgical and Materials Transactions B,* vol.40b, pp.929-939.
59. Safarian, J., Tranell, G., Kolbeinsen, M., Tangstad, M., Gaal, S., and Kaczorowski, J., (2008),'Reduction kinetics from High-Carbon ferromanganese slags by carbonaceous materials in Ar and CO atmospheres', *Metallurgical and Materials Transaction B,* vol.39b, pp.702-712.
60. Safarian, J., Grong, O., Kolbeinsen, L., and Olsen, S.E., (2006), 'A process model for the carbothermic reduction of MnO from High Carbon Ferromanganese- The model', ISIJ *International,* vol.46, No.8, pp.1120-1129.
61. Sahajwalla, V., Dubikova, M., and Khanna, R., (2004), 'Reductant characterisation and selection: Implications for ferroalloys processing', *Proceedings INFACON X: Transformation through Technology,*1-4 February, Cape Town, South Africa, pp. 351-362.
62. SANS 7404-3:1994/ISO 7404-2. Method for the petrographic analysis of bituminous coal and anthracite-Part 2: Preparation of coal samples.
63. SANS 7404-3:1994/ISO 7404-3. Method for the petrographic analysis of bituminous coal and anthracite-Part 3: Method for determining maceral group composition.
64. SANS 7404-3:1994/ISO 7404-4. Method for the petrographic analysis of bituminous coal and anthracite-Part 4: Method for determining microlithotype, carbominerate and minerite composition.
65. SANS 7404-3:1994/ISO 7404-5. Method for the petrographic analysis of bituminous coal and anthracite-Part 5: Method for determining microscopically the reflectance of vitrinite.
66. Scott, A.C., and Glasspool, I.J., (2007), 'Observations and experiments on the origin and formation of inertinite group macerals', *International Journal Coal Geology,* vol. 70, pp. 53-66.
67. Skjervheim, T., and Olsen, S.E., (1995), 'The rate and mechanism for reduction of manganese oxide from silicate slags', *INFACON 7,* Trondheim, Norway, pp. 631- 639.
68. Smith, G.C., and Cook, A.C., (1980), 'Coalification paths of exinite, vitrinite and inertite', *FUEL,* vol. 59, pp. 641-646. Doi: 10.1016/0016-2361 (80) 90127-1.
69. Snyman, C.P., and Botha, W.J., (1993), 'Coal in South Africa', *Journal of African Earth Sciences,* vol.16, pp. 171-180.
70. Stach, E., Mackowsky, M-Th., Teichmuller, M., Taylor, G.H., Chandra, D., and Teichmuller, R., (1982), *Stach's textbook of coal petrology.* 3rd edition, Berlin, Gebruder Borntraeger.
71. Speight, J.G., (2015), '*Handbook of coal analysis'*, John Wiley and Sons.
72. Suarez-Ruiz, I., Diez, M.A. and Rubiera, F., (2019), '*Coal. New Trends in coal conversion: combustion, gasification, emissions and coking*', Woodhead Publishing, pp. 1-30.

73. Suarez- Ruiz, I., and Ward, C.R., (2008), 'Introduction to Applied Coal Petrology', *Applied Coal petrology. The role of petrology in coal utilization,* pp. 2-18.
74. Suharno, B., Nurjaman, F., Rifki, A., Elvin, R.K., Putra, A.A., and Ferdian, D., (2018), 'Coke and coals as reductants in manganese ore smelting: An experiment', *Mineralogia,* vol. 49, no. 1-4, pp. 35-45.
75. Sun, H., Lone, M., Ganguly, S., and Ostrovski, O., (2010),'Reaction of manganese containing slag with carbon substrate', The *Twelfth International Ferroalloys Congress: Sustainable Future,* Helsinki, Finland, June 6-9, pp. 557-568.
76. Swamy, K.N., and Robertson, D.G.C., (2001), 'Factors affecting carbon consumption in the production of High Carbon Ferromanganese', *INFACON 9: The ferroalloys association,* pp. 293-301.
77. Tang, K and Olsen, S.E (2006), 'Computer simulation of equilibrium relations in manganese ferroalloy production', *Metallurgical and Materials Transactions B,* vol.37, no.4, pp. 599-606.
78. Tangstad, M., Steenkamp, J.D., Ringdalen, E., and Beukes, J.P., (2019), '*Coal based reducing agents in ferroalloys and silicon production', New Trends in coal conversion: combustion, gasification, emissions and coking,* Woodhead Publishing.
79. Tangstad, M., and Ishak, R., (2007), 'Degree of pre reduction without coke consumption in industrial furnaces' *INFACON XI,* pp.269-280.
80. Tangstad, M., Ichihara, K., and Ringdalen, E., (2015),'Pre-treatment unit in ferromanganese production', *The Fourteenth International Ferroalloys Congress: Energy efficiency and environmental friendliness are the future of the global Ferroalloy Industry,* Kiev, Ukraine, May 31-June 4. Pp.99-106.
81. Tangstad, M., and Olsen, S.E., (1995),'The ferromanganese process-material and energy balance', *INFACON 7,* Trondheim, Norway, June 1995. pp.621-630.
82. Tangstad, M., and Olsen, S.E., (1997), 'Phase relations in ferromanganese slags during melting and reduction', Molten *Slags, Fluxes and Salts* pp. 549-555.
83. Tangstad, M., and Olsen, S.E., (2004), 'Silicomanganese production-process understanding', *INFACON X: Transformation through technology. Proceedings: Tenth International Ferroalloys Congress,* Cape Town, 2-4 February pp. 231-238.
84. Tangstad, M., and Safarian, J., (2010), 'Slag-carbon reactivity', *The Twelfth International Ferroalloys Congress: Sustainable Future,* Helsinki, Finland, 6-9 June, pp. 327- 337.
85. Tang, Y., Li, R., and Wang, S., (2020), 'Research progress and prospects of coal petrography and coal quality in China. *International Journal Coal Science Technology,* vol. 7, no. 2, pp. 273-287.
86. Tangstad, M., and Jayakumari, S., (2015), 'Carbon materials for silicomanganese reduction', *The Fourteenth International Ferroalloys Congress,* 31 May- 4 June, Kiev, Ukraine, pp. 374- 381.
87. Teichmüller, M., and Teichmüller, R., (1968). 'Geological aspects of coal metamorphism'. In Murchison, D. G. and Westoll, T. S. (Eds), "*Coal- and coal bearing strata*', Oliver & Boyd, Edinburgh, Scotland.
88. Thompson, M., and Walsh, N.J., (1989), '*Handbook of Inductively Coupled Plasma Spectrometry*', 2nd ed. New York, Chapman and Hall.
89. Teasdale, S.L., and Hayes, P.C., (2005), 'Kinetics of reduction of FeO from slag by graphite and coal chars', *ISIJ International,* vol.45, No.5, pp. 642-650.
90. Teasdale, S.L, and Hayes, P.C., (2005), 'Observations of the reduction of FeO from slag by graphite, coke and coal char', *ISIJ International,* vol. 45, No.5, pp.634-641.

91. Tranell, G., Gaal, S., Lu, D., Tangstad, M., and Safarian, J., (2007), 'Reduction kinetics of manganese oxide from HC FeMn slags', *INFACON XI*, pp.232-240.
92. United Nations Economic Commission for Europe, (1998), 'International classification of in-seam coals, Geneva.
93. Wilberforce, O., and Olivia, E., (2017), 'Proximate analysis and rankings of a suspected sample of coal from Afikpo and Enugu', *International Journal of Biology, Pharmacy and Allied Sciences,* vol. 6, pp. 362-332.
94. Xie, K., (2015), '*Structure and Reactivity of coal: A survey of selected Chinese Coal'*, Springer, DOI: 10.1007/978-3-662-47337-5.
95. Yastreboff, M., Ostrovski, O., and Ganguly, S., (1998), 'Carbothermic reduction of manganese from manganese ore and ferromanganese slags'*, INFACON 8,* Beijing, China, pp. 263-270.
96. Zhu, Q., (2014), 'Coal sampling and analysis standards', *IEA Clean Coal Centre.*

APPENDIX A

Appendix A consists of temperature profile that was recorded during the slag reactivity tests conducted in a muffle furnace.

Reactivity test data

Table 36: Temperature profile for reactivity tests in muffle furnace

Time (min)	Actual	Set-point	
0	128	133	
15	278	278	
24	365	366	
34	459	459	
44	558	559	
55	661	661	
64	753	754	
73	838	839	Warm up
83	935	935	
93	1033	1034	
103	1132	1132	
114	1233	1234	
123	1324	1324	
133	1424	1425	
143	1501	1500	
158	1500	1500	
188	1500	1500	
218	1500	1500	At temperature
248	1500	1500	
278	1500	1500	
294	1499	1500	

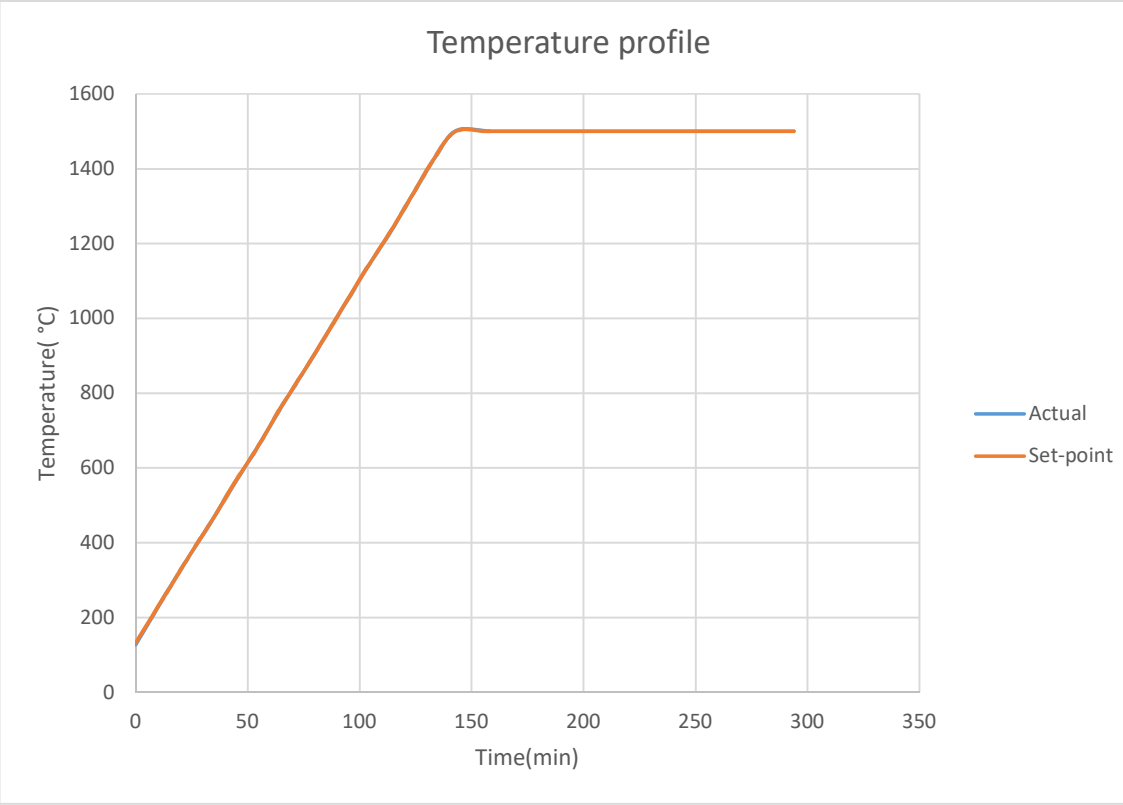

Figure 49:Graph representing temperature profile of actual vs set-point

Table 37: Coal 1 reactivity tests data

Sample	Time at temperature	BEFORE			AFTER	Mass loss
		Reductant crucible	Slag	Reductant crucible + slag	Reductant crucible +slag	
	min	g	g	G	g	%
All	0					0
#1	72	57.7	22.7	80.3	53.9	33
#2	144	51.6	18.7	70.3	44.3	37
#3	216	55.0	16.7	71.7	43.2	40
#4	288	39.6	13.1	52.7	34.3	35
#5	360	27.1	15.7	42.8	26.1	39

Table 38: Coal 2 reactivity tests data

Sample	Time at temperature	BEFORE	AFTER			Mass loss
		Reductant crucible	Slag	Reductant crucible + slag	Reductant crucible +slag	
	min	g	g	g	g	%
All	0					0
#1	72	44.1	12.4	56.5	34.7	39
#2	144	40.8	17.2	58.0	39.0	33
#3	216	32.5	15.7	48.2	29.9	38

#4	288	50.5	17.5	68.0	40.0	41
#5	360	58.8	17.2	76.0	45.9	40

Table 39: Anthracite reactivity data test 1

Sample	Time at temperature	BEFORE			AFTER	Mass loss
		Reductant crucible	Slag	Reductant crucible + slag	Reductant crucible +slag	
	min	g	g	G	g	%
All	0					0
#1	72	51.3	14.1	65.4	57.1	13
#2	144	44.1	8.3	52.4	41.8	20
#3	216	49.8	17.2	67.0	54.4	19
#4	288	43.8	9.4	53.2	40.6	24
#5	360	41.5	13.5	55.0	41.2	25

Table 40: Anthracite reactivity tests 2 data

Sample	Time at temperature	BEFORE			AFTER	Mass loss
		Reductant crucible	Slag	Reductant crucible + slag	Reductant crucible +slag	
	min	g	g	g	g	%
All	0					0
#1	72	54.2	14.6	68.8	62.3	9
#2	144	54.6	12.2	66.8	54.6	18
#3	216	49.1	12.9	62.0	51.0	18
#4	288	52.7	10.3	63.0	49.0	22
#5	360	61.7	13.4	75.1	59.6	21

Table 41: Anthracite reactivity tests 2 data

Sample	Time at temperature	BEFORE			AFTER	Mass loss
		Reductant crucible	Slag	Reductant crucible + slag	Reductant crucible +slag	
	min	G	g	G	g	%
All	0					0
#1	72	35.8	8.1	43.9	37.1	15
#2	144	43.4	6.9	50.3	40.2	20
#3	216	38.7	18.5	57.2	46.4	19
#4	288	42.8	17.0	59.8	47.8	20
#5	360	47.1	14.5	61.6	48.4	21

APPENDIX B

Method development

Appendix B contains the operating procedure developed for the muffle type tests conducted to determine reductant reactivity on slag.

For the muffle furnace type tests a procedure was developed,

Step 1

The prepared reductant 'crucibles' are weighed before heat treatment and mass recorded.





Step 2

The reductant crucibles are then filled with the slag and then weighed and mass recorded. The mass of the slag is determined by difference.





Step 3

Weigh mass of empty alumina crucible and insert reductant crucible and slag sample to contain the contents.




Step 4

To ensure that atmosphere remains controlled, place refractory board on top of the alumina crucible and place reactive carbon on top to serve as sacrificial carbon.



Step 5

Inspect chamber furnace and working parts according to **PDD-SOP- 732**. Ensure that the gas seal is tight, that there is adequate ventilation.

Step 6

Open flowmeter to allow purging of the chamber with Argon gas for approximately 30 minutes. Ensure that the chamber furnace seal door is properly closed.





Step 7

Open cooling water and allow to run.





Step 8

Open chamber and load sample inside chamber. Assure that the sample is firmly place on the floor of the chamber. Close the door seal properly.



Step 9

Proceed to switch on the furnace whilst the cooling water is still running and argon gas open.

Step 10

Set test program on controller according to **PDD-SOP-784.** Ensure that the seal door is properly closed.

Step 11

Once test is complete, remove sample from furnace chamber and ensure all safety and environmental precautions are followed. Measure the slag and carbonaceous reductant mass after reaction in order to calculate the mass loss %.

Standard operating procedures used for the muffle furnace type tests

MINTEK

Chamber Furnace

Technique / Method / SOP
SOP

Document No. PDD-SOP-732
Effective From Date: 2019-12-13
Last Review Date: 2019-11-18
Document Owner: Lee-Ann Terry
Approver: Isabel Geldenhuys

Potential hazards to environment and/or safety of persons:
Burns, gas and sample material

1. PURPOSE

To provide a procedure for the operation, calibration and maintenance of chamber furnaces in the Pyrometallurgy Division.

2. SCOPE

Procedure for operation, calibration and maintenance of chamber furnaces

3. DEFINITIONS

- Chamber furnace: A chamber furnace operated at different temperatures.
- Controller: An electronic device for setting the operating temperature of the furnace.
- Set point temperature: The temperature setting on the controller
- Furnace temperature: The temperature in the centre of the furnace chamber

Refer to Glossary of Terminology (SHEQ STD-000) for general SHEQ definitions

4. RESPONSIBILITIES AND AUTHORITIES

Responsibilities and authorities as defined in the Areas of Responsibility procedure PDD-SOP-0103.

5. PROCEDURE

Although this procedure provides the basic user instructions for the Chamber furnaces, a person familiar with Chamber furnaces might follow a slightly different procedure still achieving the same results.

5.1 Safety

The operator of a Chamber furnace is exposed to heat when the door of the furnace is opened. When a sample is inserted or removed from a hot furnace, the operator should assess the situation and make **use of the following personal protective equipment (PPE):**

Xolisa Gqoso 2020-05-22

5.3.5. On completion of the experiment remove sample from furnace and ensure all the safety and environmental precautions are followed.

5.4 Temperature verification

Chamber furnaces are not calibrated at predetermined intervals. All members of staff are advised to obtain a temperature profile for a specific Chamber furnace should the tests carried out in that furnace require very accurate temperature measurements and record the information.

Relevant Quality risks are identified in the PIC for a particular project. If the Chief Investigator for a particular project requires that the temperature in the Chamber furnace be accurately controlled, this is done prior to use and should be captured in the Project report

In order to protect the Chamber furnace, the CI should verify the maximum continuous operating temperature (for the gas atmosphere in use) of the Chamber furnace and ensure that this temperature is not exceeded

5.5 Maintenance

5.5.1. It is advised that an inspection of the electrical connections and elements be carried out once every six months.

5.5.2. It is advised that an inspection of the refractories be carried out once every six months or if it is suspected that material had spilt out in the furnace during an experiment.

5.5.3. Maintenance will be carried out when required by qualified persons.

5.5.4. Information about the maintenance of the furnace will be recorded by the responsible person.

Faults and maintenance:

If you encounter something not working no matter how small an issue you think it may be (e.g. faulty power on globe or voltage gauge, door panel does not close/lock properly) please report it to PyroMaintenance. Often these seemingly little things are very important from a safety aspect and may result in an incident or injury.

If electrically operated equipment is known to be faulty or requires maintenance it is critical that it is switched off and locked out (electrical isolator turned off and padlocked, DB isolated). In such a case it is important that Senior Superintendent: Control and Electrical is contacted to ensure that the equipment is indeed safe to work on before commencing any maintenance (eg. element changes). Should the Senior Superintendent: Control and Electrical not be available an EMS electrician can also be contacted.

If the equipment has a plug, the wall socket should also be switched off and the plug removed. Ideally the plug itself should be locked out with a suitable clamping device but failing this it should be removed (by an electrician) to prevent someone plugging it in again. Putting signage on the equipment to communicate that it is faulty and may not be used, is also advisable.

6. RECORDS

None

Xolisa Gaga 2020-05-22

MINTEK

User instruction for the Caho P961 Controller

Technique / Method / SOP
SOP

Document No. PDD-SOP-784
Effective From Date: 2019-09-16
Last Review Date: 2019-09-05
Document Owner: Lee-Ann Terry
Approver: Isabel Geldenhuys

This document is controlled when viewed on the SharePoint document system or in the locations or with the people specified in the controlled copies section

Potential hazards to environment and/or safety of persons:
None

1 PURPOSE

To provide the user instructions needed to program the Caho P961 controller

2 SCOPE

Instructions for programming the Caho P961 controller

3 DEFINITIONS

- *Muffle furnace:* A chamber furnace operated at high temperatures
- *Tube furnace:* A furnace that uses a ceramic tube as the reaction chamber
- *Controller:* An electronic device for setting the operating temperature of the furnace. A number of different controllers are used and for each of these the operating instructions are attached to the instrument.

Refer to Glossary of Terminology (SHEQ-STD-000) for general SHEQ definitions

4 RESPONSIBILITIES AND AUTHORITIES

All staff members of Pyrometallurgy Division using a furnace with the Caho P961 controller have the responsibility to familiarize themselves with the user instructions for programming the Caho P961 controller before attempting to operate the furnace.

Xolisa Gaso 2020-05-22



	DOWN: Decrease a value
	ENTER : shift



Entering a program

THEORY : The programmer works on the principle of heating to a target temperature at a specific rate and remaining at that target for a specific amount of time then execute the next STEP (up to 8 STEPS can be programmed). When starting (RUN) program the 1st ramp will begin from the current furnace temperature.

Programming

1. Press PROG/END and **Ptn1** will display
2. Press ENTER to select the pattern. Ptn1 is a program to heat to 1600°C and stay at temperature for a period of 1 hour. Ptn2 is a flexible pattern that can be used for any temperature to be investigated. LInY can link both Ptn1 and Ptn1 to create a program which consists of 16 steps.
3. Press SET and **P.end/Hold**, segment off will display
4. Press SET and **P.ALn off** will display
5. Press SET and **P.tne/P-Hn** will display
6. Press SET and **Band 1** will display
7. Press SET and **SP-1** will display. Press ENTER and select the temperature using the UP and DOWN buttons.
8. Press SET and **rpt.1** will display. Press ENTER and select the ~~rate~~ time required to reach the temperature at **SP-1** using the UP and DOWN buttons. The rate is measured by hours and minutes and will display as 00:00 (hours:minutes).
9. Press SET and **syt.1** will display. Press ENTER to select dwelling time by using UP and DOWN buttons. Dwelling time is also displayed as 00:00 (hours:minutes)
10. Press SET and SP-2 will display
11. Continue from step 7 and set
    - SP-n TEMPERATURE for n = 1 to 8
    - rpt.n RAMP RATE for n = 1 to 8
    - syt.n DWELL TIME for n = 1 to 8
12. ~~To end or add more steps on~~ After the last stage, press PROG/END
13. To start the program, press RUN
14. To exit the program press STOP for approximately 5 seconds and monitor the temperature decrease before leaving the furnace to cool down on its own. Pressing STOP gets you out of the program.

Record the information according to the instructions given in the logbook provided next to the furnace.

Kolisa Gosa Gosa 2020-05-22

APPENDIX C

Petrography data

Sample : 2107_r

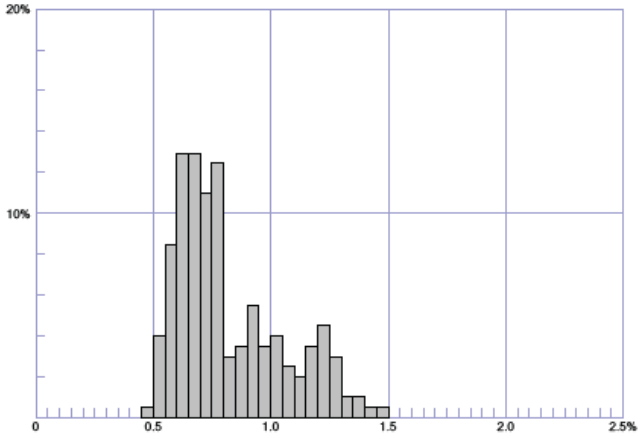

Measure count =	201	Date	3/17/2021 5:12 PM
Reflectance Rr =	0.815 %	Operator	
s =	0.229 %	Printed	3/29/2021

0.45 - 0.50 % R	0.5 %		1.00 - 1.05 % R	4.0 %	
0.50 - 0.55 % R	4.0 %		1.05 - 1.10 % R	2.5 %	
0.55 - 0.60 % R	8.5 %		1.10 - 1.15 % R	2.0 %	
0.60 - 0.65 % R	12.9 %		1.15 - 1.20 % R	3.5 %	
0.65 - 0.70 % R	12.9 %		1.20 - 1.25 % R	4.5 %	
0.70 - 0.75 % R	10.9 %		1.25 - 1.30 % R	3.0 %	
0.75 - 0.80 % R	12.4 %		1.30 - 1.35 % R	1.0 %	
0.80 - 0.85 % R	3.0 %		1.35 - 1.40 % R	1.0 %	
0.85 - 0.90 % R	3.5 %		1.40 - 1.45 % R	0.5 %	
0.90 - 0.95 % R	5.5 %		1.45 - 1.50 % R	0.5 %	
0.95 - 1.00 % R	3.5 %				

Figure 50: Coal 1 histogram with V-steps

Sample : 2108_r

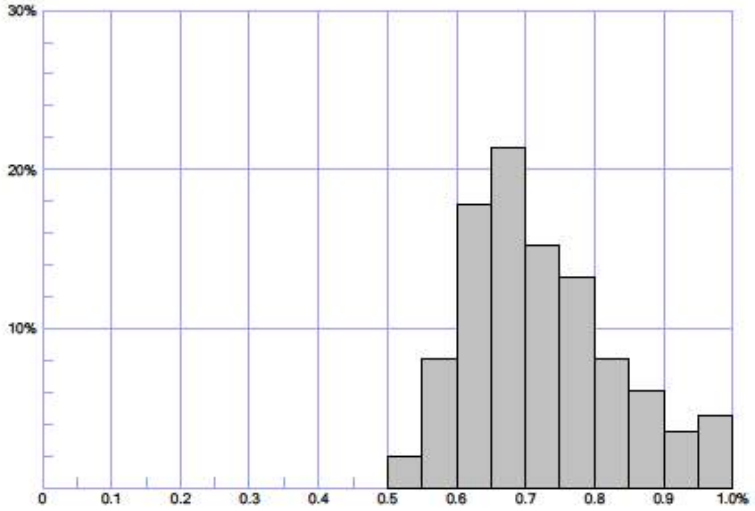

Measure count =	197	Date	3/17/2021 4:56 PM
Reflectance Rr =	0.717 %	Operator	
s =	0.107 %	Printed	3/29/2021

0.50 - 0.55 % R	2.0 %		0.75 - 0.80 % R	13.2 %
0.55 - 0.60 % R	8.1 %		0.80 - 0.85 % R	8.1 %
0.60 - 0.65 % R	17.8 %		0.85 - 0.90 % R	6.1 %
0.65 - 0.70 % R	21.3 %		0.90 - 0.95 % R	3.6 %
0.70 - 0.75 % R	15.2 %		0.95 - 1.00 % R	4.6 %

Figure 51: Coal 2 V-steps and histogram distribution

Sample : 2109_r

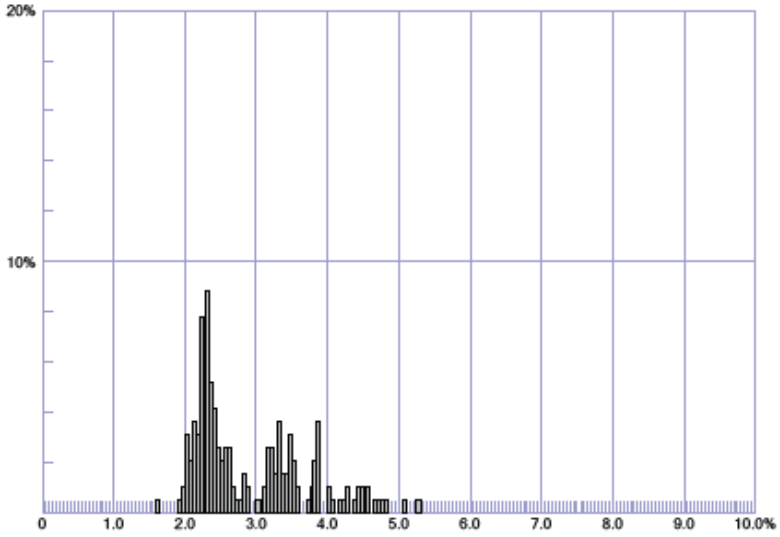

Measure count =	193	Date	3/19/2021 12:57 PM
Reflectance Rr =	2.895 %	Operator	
s =	0.793 %	Printed	3/29/2021

1.60 - 1.65 % R	0.5 %		3.15 - 3.20 % R	2.6 %	
1.90 - 1.95 % R	0.5 %		3.20 - 3.25 % R	2.6 %	
1.95 - 2.00 % R	1.0 %		3.25 - 3.30 % R	1.6 %	
2.00 - 2.05 % R	3.1 %		3.30 - 3.35 % R	3.6 %	
2.05 - 2.10 % R	2.1 %		3.35 - 3.40 % R	1.6 %	
2.10 - 2.15 % R	3.6 %		3.40 - 3.45 % R	1.6 %	
2.15 - 2.20 % R	3.1 %		3.45 - 3.50 % R	3.1 %	
2.20 - 2.25 % R	7.8 %		3.50 - 3.55 % R	2.1 %	
2.25 - 2.30 % R	5.7 %		3.55 - 3.60 % R	1.0 %	
2.30 - 2.35 % R	8.8 %		3.70 - 3.75 % R	0.5 %	
2.35 - 2.40 % R	5.2 %		3.75 - 3.80 % R	1.0 %	
2.40 - 2.45 % R	4.1 %		3.80 - 3.85 % R	2.1 %	
2.45 - 2.50 % R	2.6 %		3.85 - 3.90 % R	3.6 %	
2.50 - 2.55 % R	2.1 %		4.00 - 4.05 % R	1.0 %	
2.55 - 2.60 % R	2.6 %		4.05 - 4.10 % R	0.5 %	
2.60 - 2.65 % R	2.6 %		4.15 - 4.20 % R	0.5 %	
2.65 - 2.70 % R	1.0 %		4.20 - 4.25 % R	0.5 %	
2.70 - 2.75 % R	0.5 %		4.25 - 4.30 % R	1.0 %	
2.75 - 2.80 % R	0.5 %		4.35 - 4.40 % R	0.5 %	
2.80 - 2.85 % R	1.6 %		4.40 - 4.45 % R	1.0 %	
2.85 - 2.90 % R	1.0 %		4.45 - 4.50 % R	1.0 %	
3.00 - 3.05 % R	0.5 %		4.50 - 4.55 % R	1.0 %	
3.10 - 3.15 % R	1.0 %		4.55 - 4.60 % R	1.0 %	

Figure 52: Anthracite histogram distribution and V-steps

Table 42: Maceral group analysis of the three studied parent coals

Table 1: MACERAL GROUP ANALYSIS (% BY VOLUME)							
THESE RESULTS RELATE ONLY TO THE SAMPLES ANALYSED							
Sample no:		2107		2108		2109	
Sample identification:		Coal 1		Coal 2		Coal 3 (anth)	
		inc. mm	Mmf	inc. mm	Mmf	inc. mm	mmf
MACERAL GROUP	MACERAL (vol%)	vol%	vol%	vol%	vol%	vol%	vol%
Vitrinite	telinite	0.4	0.4	0.2	0.2	0.0	0.0
	collotelinite	22.0	24.1	31.0	33.6	13.0	13.9
	vitrodetrinite	0.0	0.0	0.0	0.0	0.0	0.0
	collodetrinite	17.5	19.2	22.0	23.9	7.9	8.4
	corpogelinite	0.4	0.4	1.3	1.5	0.2	0.2
	gelinite	0.0	0.0	0.0	0.0	0.0	0.0
	pseudovitrinite	0.2	0.2	0.2	0.2	0.2	0.2
Inertinite	fusinite	13.3	14.5	7.6	8.3	3.2	3.4
	reactive semifusinite	5.5	6.0	1.7	1.9	1.4	1.5
	inert semifusinite	19.9	21.7	18.7	20.3	54.8	58.6
	micrinite	0.0	0.0	0.0	0.0	0.0	0.0
	macrinite	0.0	0.0	0.0	0.0	0.0	0.0
	secretinite	0.6	0.6	0.2	0.2	3.7	4.0
	funginite	0.0	0.0	0.0	0.0	0.0	0.0
	inertodetrinite R	0.2	0.2	0.2	0.2	0.2	0.2
	inertodetrinite I	7.2	7.9	6.1	6.6	8.5	9.1
Liptinite	sporinite	3.9	4.3	2.5	2.7	0.4	0.4
	cutinite	0.4	0.4	0.4	0.4	0.0	0.0
	resinite	0.0	0.0	0.0	0.0	0.0	0.0

	alginite	0.0	0.0	0.0	0.0	0.0	0.0
	liptodetrinite	0.0	0.0	0.0	0.0	0.0	0.0
	suberinite	0.0	0.0	0.0	0.0	0.0	0.0
	exsudatinite	0.0	0.0	0.0	0.0	0.0	0.0
MACERAL GROUP	VITRINITE	40.5	44.3	54.7	59.3	21.3	22.8
TOTALS (vol%)	INERTINITE	46.6	51.0	34.6	37.6	71.8	76.8
	LIPTINITE	4.3	4.7	2.9	3.1	0.4	0.4
	MINERAL MATTER	8.6		7.8		6.5	
	TOTAL INERTINITE	46.6	51.0	34.6	37.6	71.8	76.8
	TOTAL REACTIVE MACERALS	50.5	55.2	59.5	64.5	23.3	24.9

Table 43: Vitrinite reflectance analysis data of the parent coals

TABLE 2: VITRINITE REFLECTANCE ANALYSIS (RoV%)							
Sample no:		2107		2108		2109	
Sample identification:		**Coal 1**		**Coal 2**		**Coal 3 (anth)**	
Vitrinite reflectance	Rmax	0.815		0.717		2.895	
(RoV%)	st. dev.	0.229		0.107		0.793	
	Rrandom						
	st. dev.						
	maximum reading						
	minimum reading						
	number of points	201		197		193	
	RANK CATEGORY	Med Rank C bit		Med rank C bit		Anth	

The following micrographs were generated from the petrography assessment:

Coal 1 reacted coal sample images showing evolution of macerals with reaction time progression

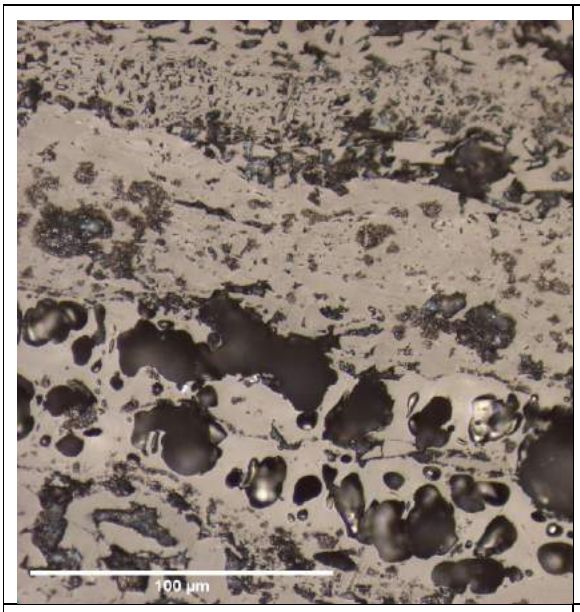

A

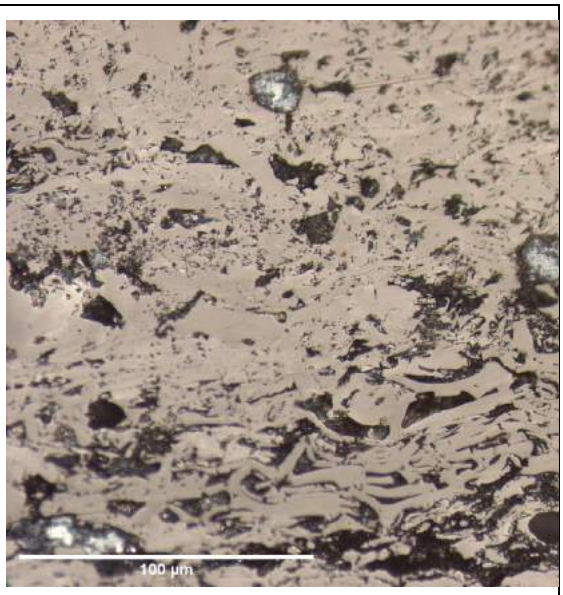

B



C

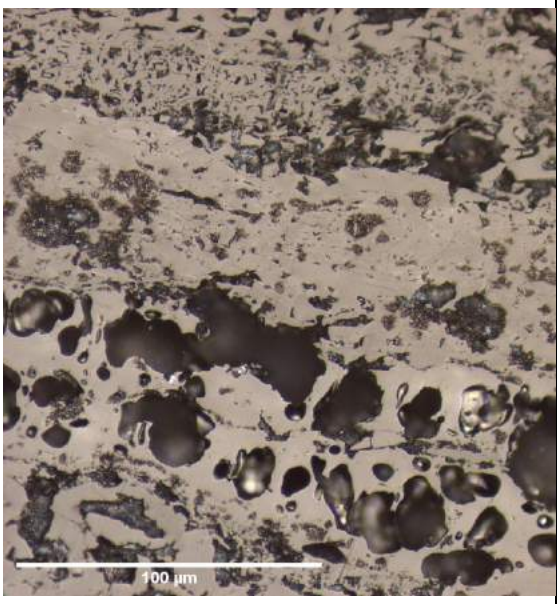

D

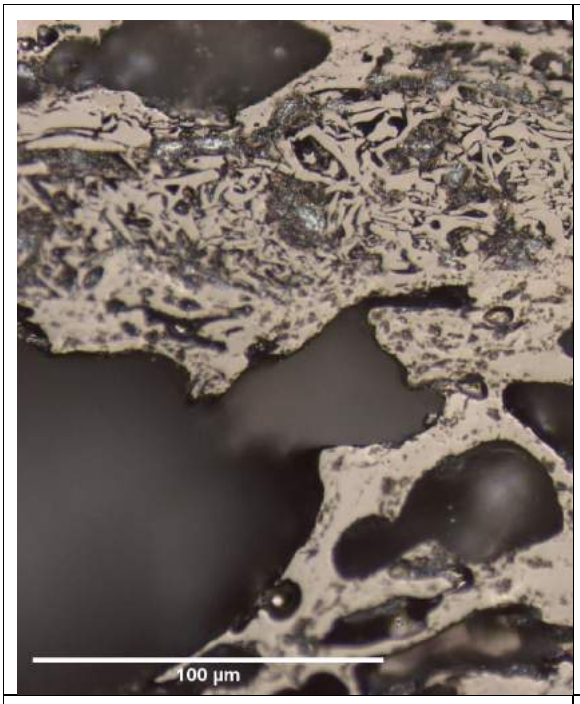	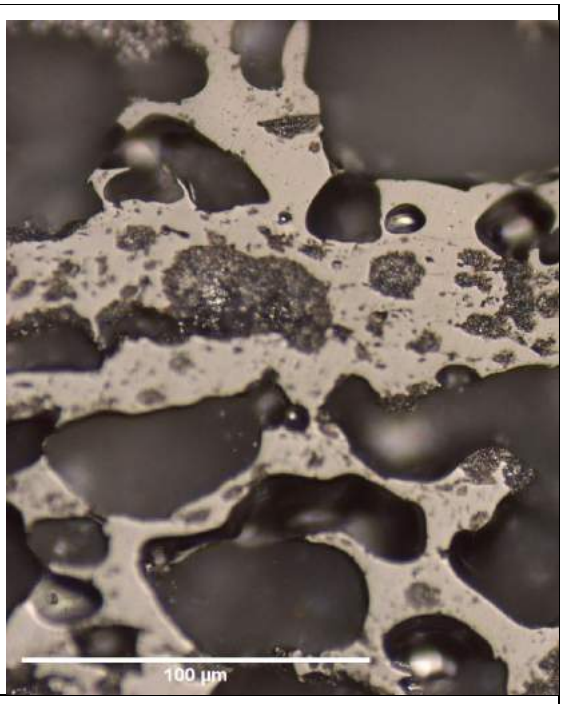
E	F
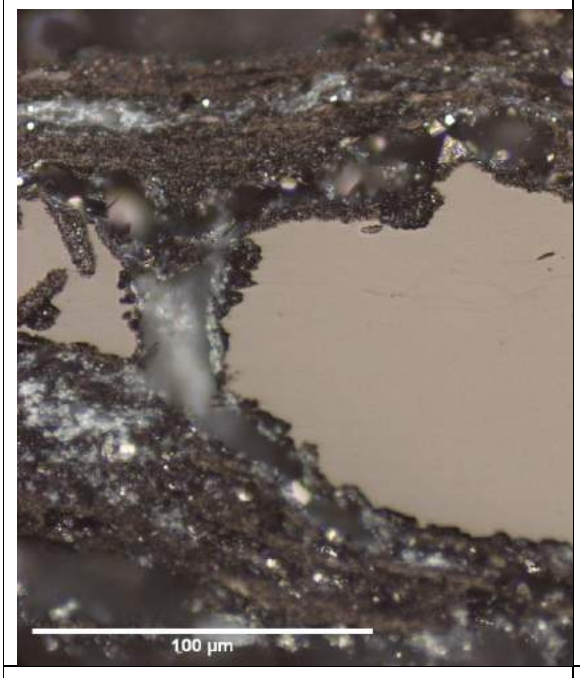	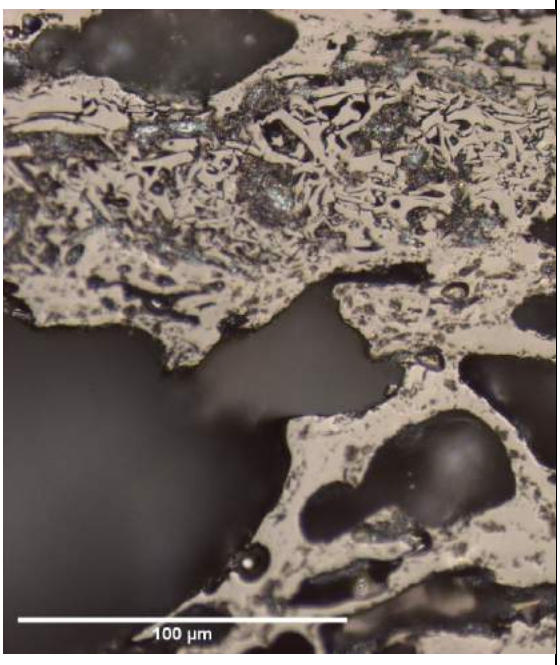
G	H

	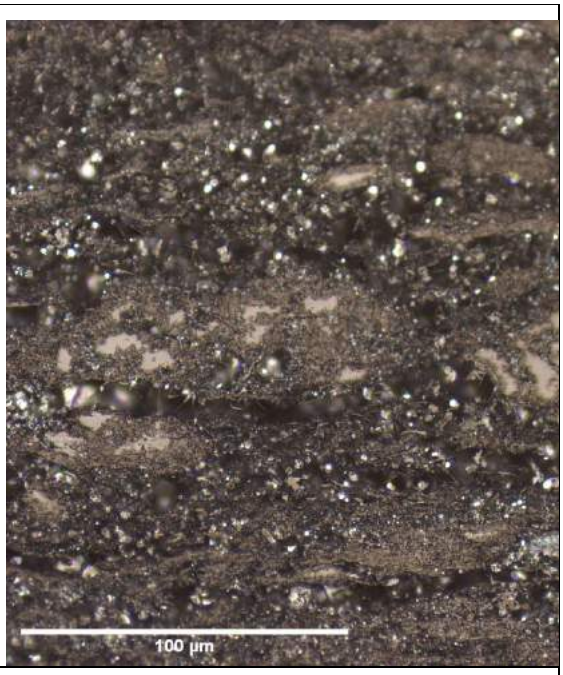
I	J

A, B- Visible porous vitrinite and inert unreacted fusinite at 144 minutes reaction time.

C, D- Inert fusinite partially consumed at 216 minutes reaction time. Bands of vitrinite and semifusinite still visible with vitrinite showing signs of devolatilization.

E, F- Highly porous vitrinite being impeded by the inert semifusinite from reacting at 216 minutes reaction time.

G, H- Highly porous vitrinite band at 288 minutes reaction time.

I, J- Indistinguishable inertinite and vitrinite macerals at 360 minutes reaction time and mineral matter with some metal prills are visible within the coal. The coal is altered and shows signs of coal being partially consumed.

Coal 2 reacted samples

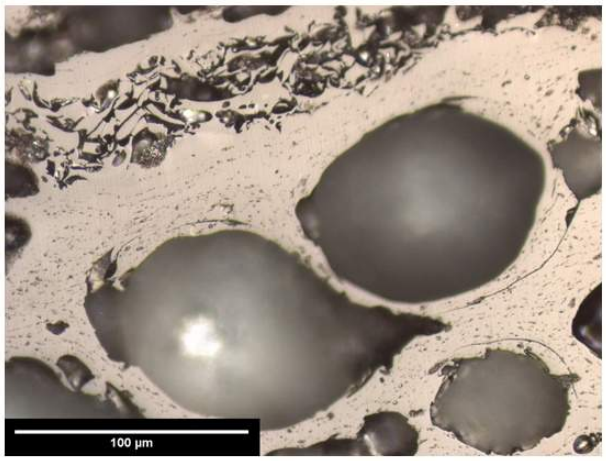

A

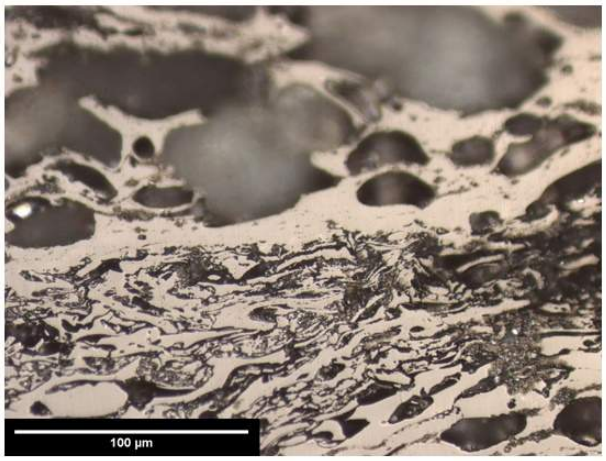

B

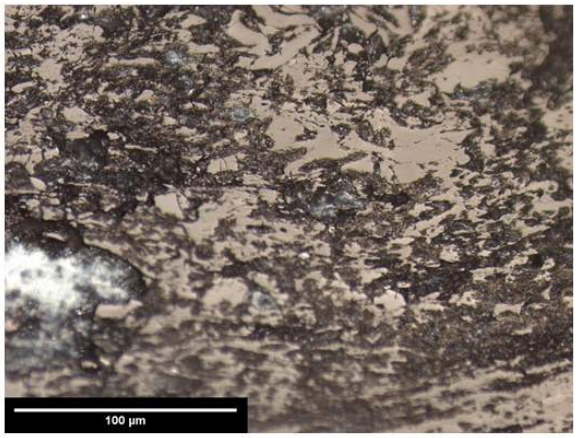

C

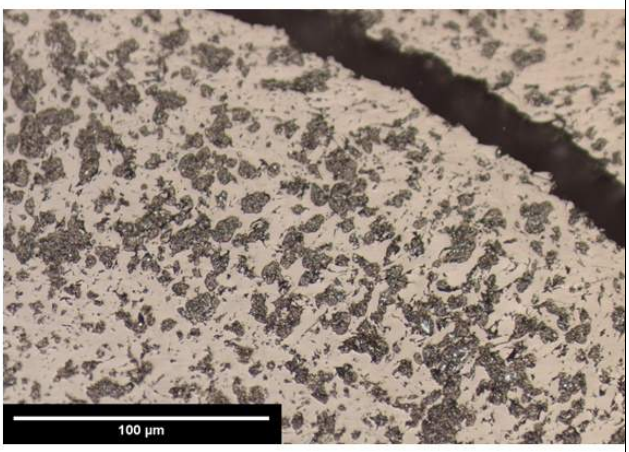

D

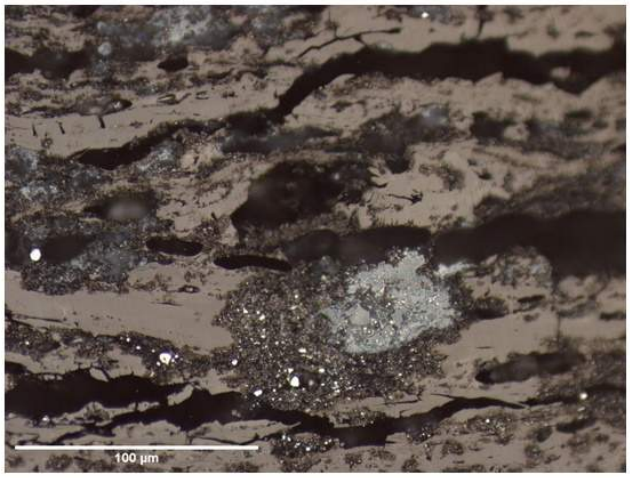

E

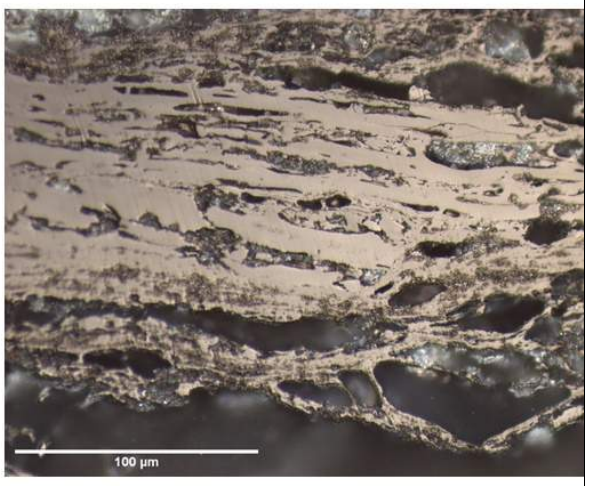

F

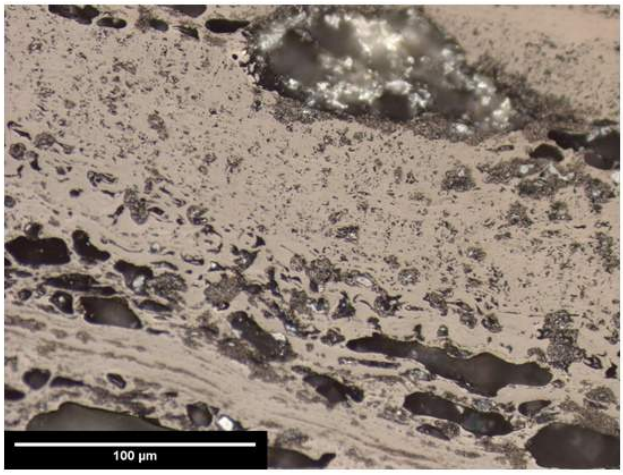

G

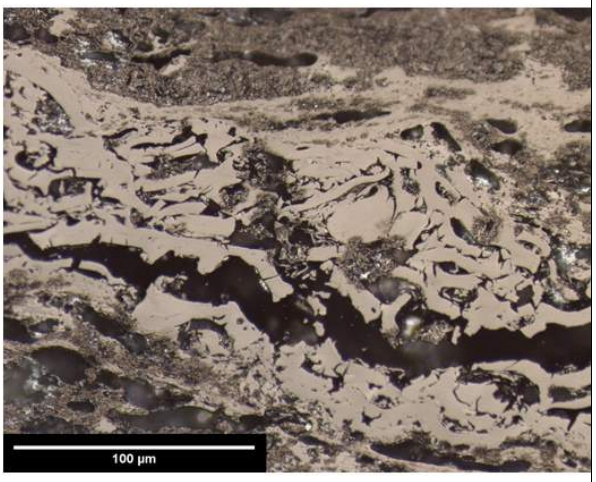

H

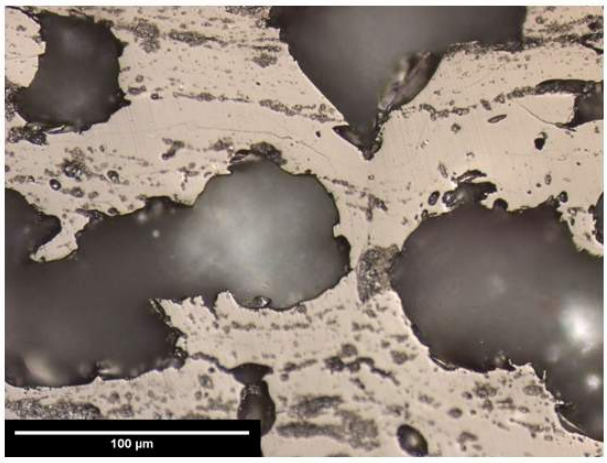

I

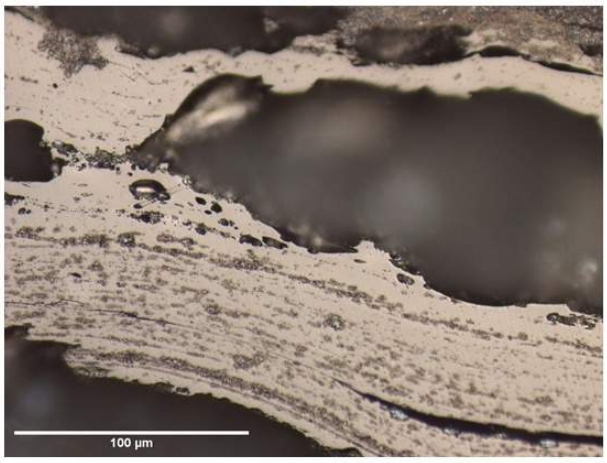

J

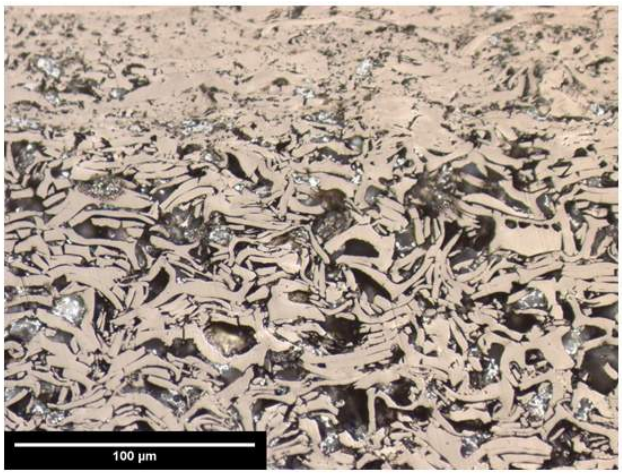

K

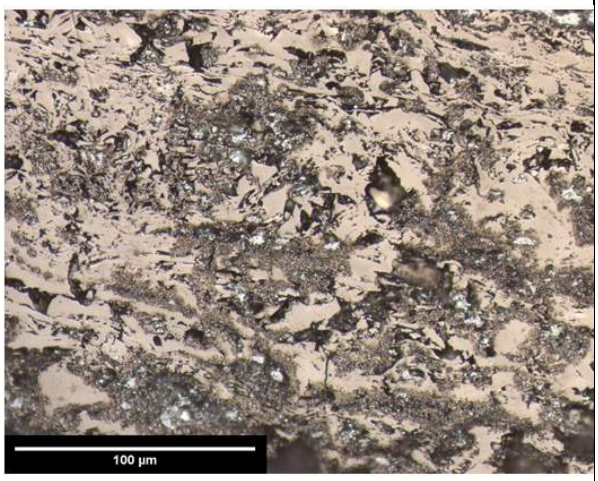

L

A, B- Unreacted fusinite and highly porous particle likely derived from vitrinite rich band at 72 minutes reaction time.

C, D- Partially consumed fusinite with visible mineral matter at 144 minutes reaction time.

E, F- Altered inert fusinite with slightly porous vitrinite band showing signs of devolatilization with associated minerals hindering the pores at 216 minutes reaction time.

G, H- Unreacted semifusinite and fusinite with visible mineral matter at 288 minutes reaction time.

I, J- Highly porous vitrinite with visible bands at 360 minutes reaction time

K, L- unreacted inert fusinite and semifusinite with visible mineral matter inclusions at 360 minutes reaction time.

SEM-EDS data

The following images are post mortem images generated from SEM-EDS depicting some of the special properties that were noted at the different reaction times.

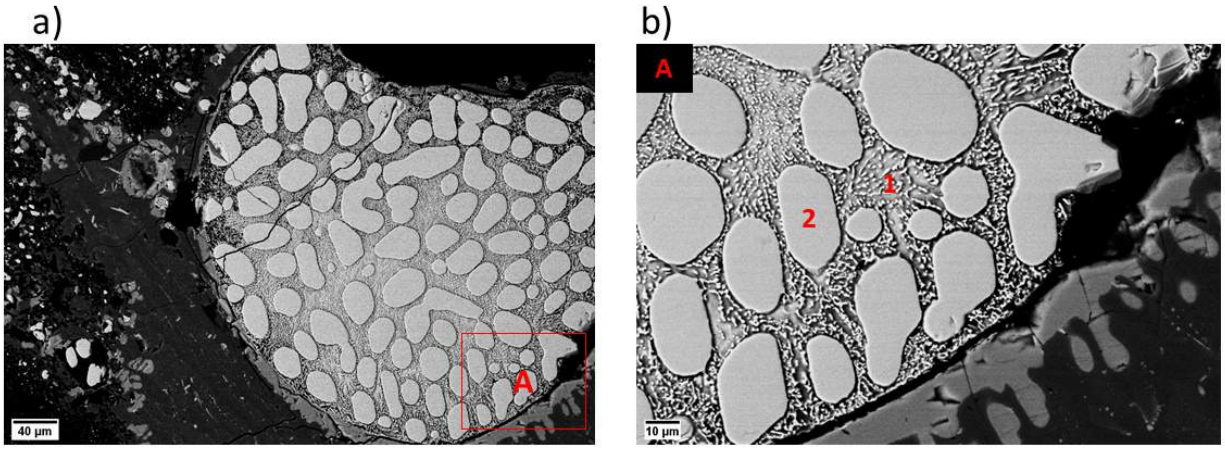

Figure 53: Zoomed out alloy phases of Coal 1 at 72 minutes reaction time

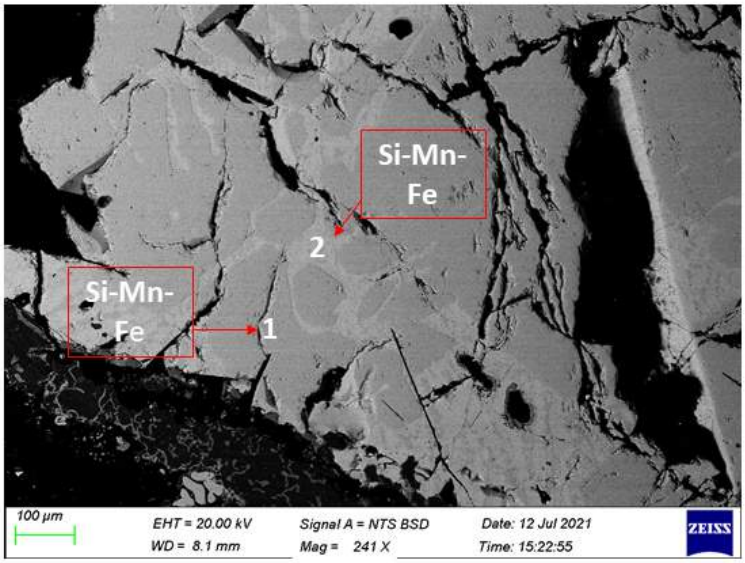

Figure 54: Alloy phases for Coal 1 at 72 minutes reaction time with a different microstructure

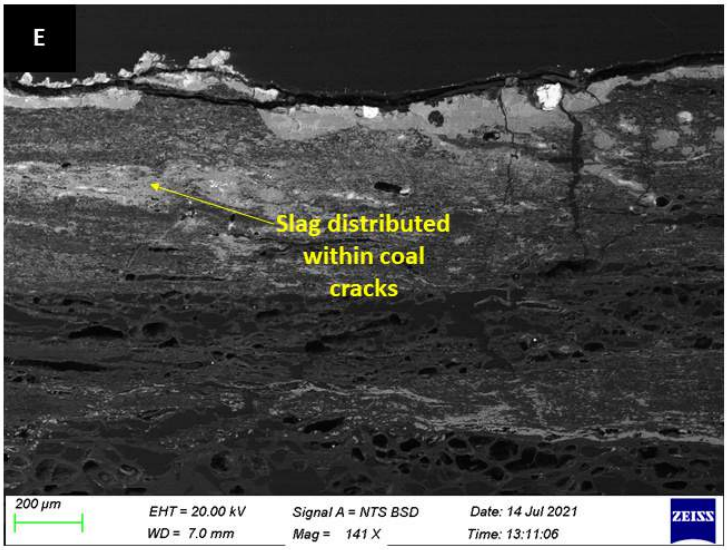

Figure 55: Coal 1 at 216 minutes reaction time, showing porous coal with slag depositing within the pores

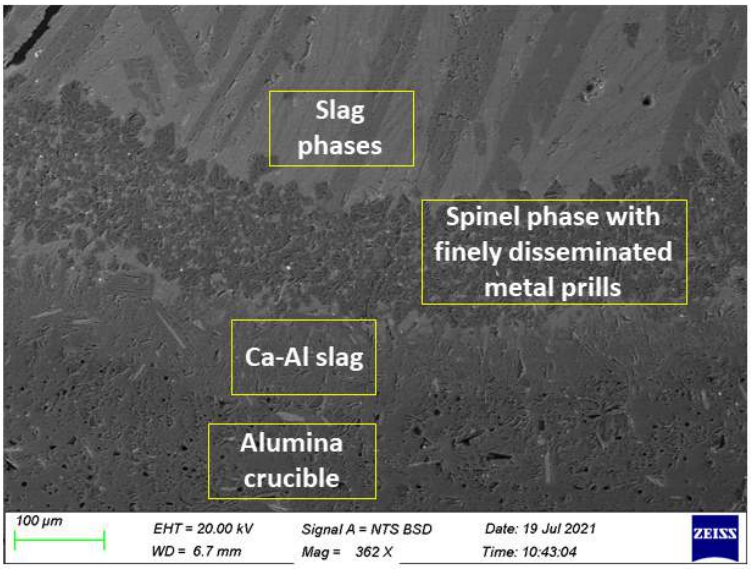

Figure 56: Settling phases found at the bottom of alumina crucible in Coal 1 at 288 minutes reaction time

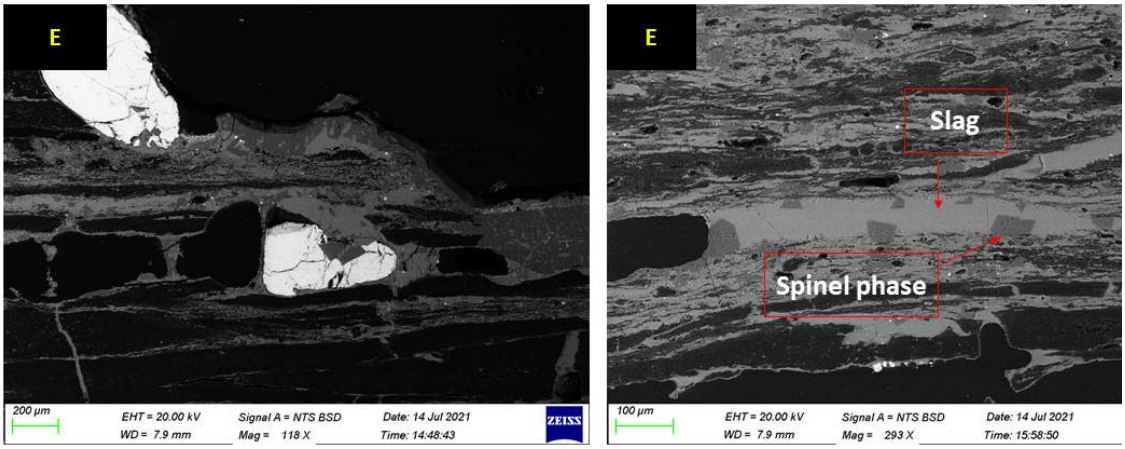

Figure 57: Coal 1 at 360 minutes reaction time showing alloy found in between large pores with slag

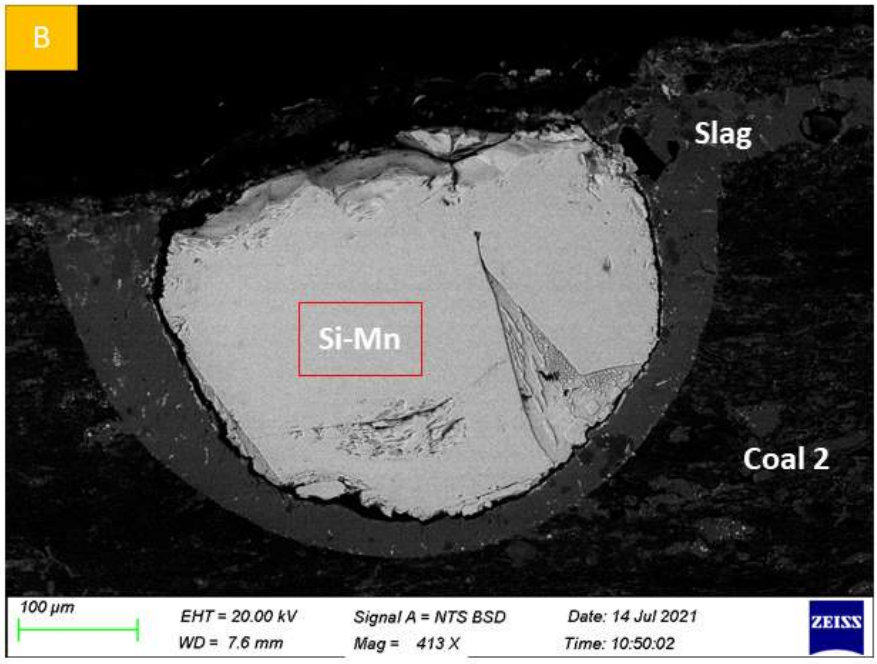

Figure 58:Coal 2 alloy at 144 minutes reaction time associated with the slag

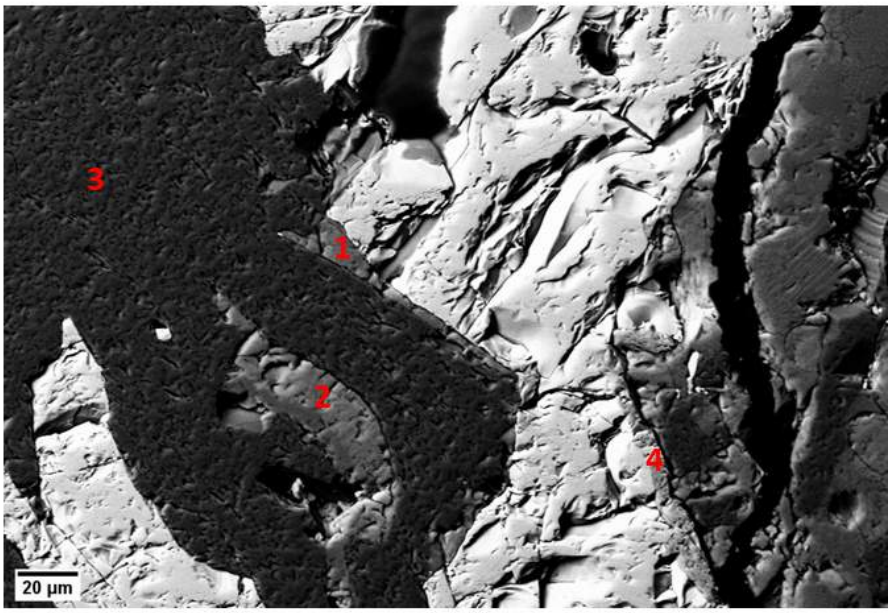

Figure 59: Zoomed out phases associated with alloy at 288 minutes reaction time Coal 2

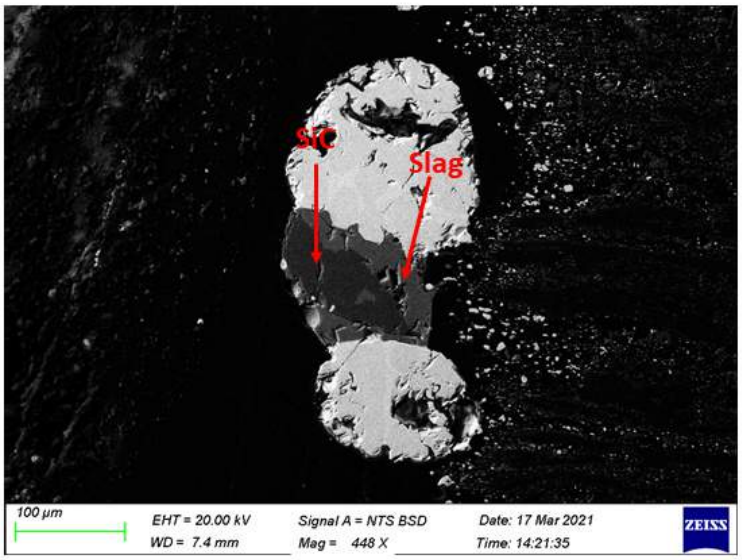

Figure 60: Alloy of Anthracite at 72 minutes reaction time with displaced slag

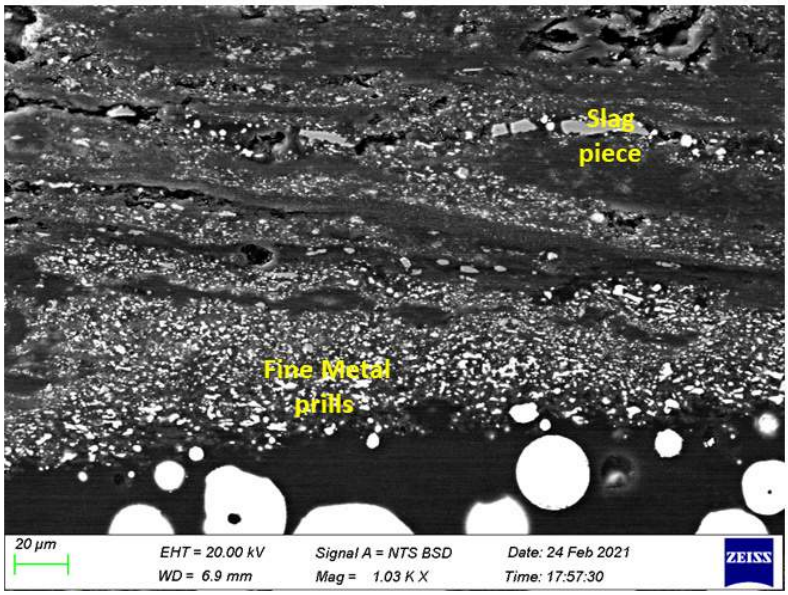

Figure 61: Metal prills found finely disseminated in Anthracite at 144 minutes reaction time

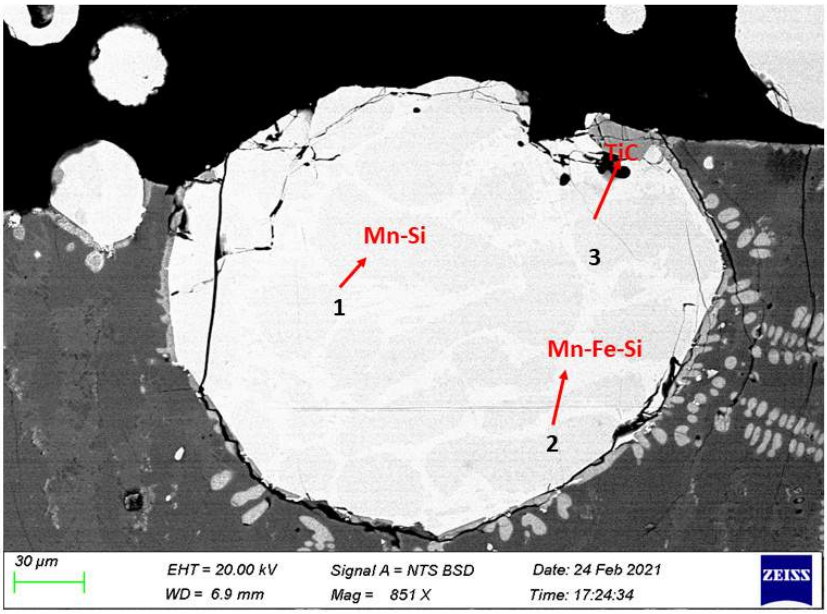

Figure 62: Alloy phases of Anthracite at 144 minutes reaction time